

## **The earthquake of 1980 November 23 in Campania–Basilicata (southern Italy)**

**Rob Westaway<sup>★</sup> and James Jackson** *Bullard Laboratories,  
Department of Earth Sciences, University of Cambridge, Madingley Road, Cambridge  
CB3 0EZ*

Accepted 1987 January 6. Received 1987 January 6; in original form 1986 May 26

**Summary.** Teleseismic waveforms, local ground acceleration, elevation changes, surface faulting and aftershocks are used to investigate the three-dimensional geometry of fault movement in the destructive earthquake ( $M_S = 6.9$ ) of 1980 November 23 in Campania–Basilicata (southern Italy).

Twelve kilometres of surface faulting has been identified following this earthquake. The re-determined epicentre and focal mechanism, and the focal depth of 10 km, determined by modelling long-period teleseismic body waves, show that the hypocentre was on a downward projection of the surface faulting, and that the seismogenic normal fault was approximately planar, with a dip of  $60^\circ$ , from the hypocentre to the surface. Further analysis of the long-period body-waves indicates that, within 10 s of the origin time of the earthquake, motion occurred on three discrete fault-segments extending for 30 km along strike. Fault rupture in the earthquake propagated predominantly towards the NW. An overall moment tensor for the earthquake is obtained from the inversion of long-period GDSN and WWSSN data, and shows that the total scalar moment of  $26 \times 10^{18}$  Nm is approximately double that accounted for by the fault motion in these first three subevents. We use teleseismic body-waves, locally recorded ground acceleration and aftershocks to investigate the position, timing and orientation of the additional seismic sources responsible for the remaining seismic moment. These data suggest that a fourth subevent occurred about 13 s after the first motion, approximately 20 km SE of the hypocentre of the first subevent. Two later fault ruptures also occurred, beneath the hanging wall of the earlier ruptures, about 20 and 40 s after the first motion. Long-period body waves and elevation changes are consistent with these occurring on normal faults, dipping at about  $20^\circ$  NE, at the base of the upper-crustal seismogenic zone. The total of six subevents that we identify for this earthquake account for almost all of the scalar moment in the overall moment tensor.

<sup>★</sup>Present address: Department of Earth Sciences, University of Liverpool, Brownlow Street, Liverpool L69 3BX.

The geometry of normal faulting in this earthquake is reflected in the geomorphology and structural geology of the epicentral region. The elevation changes accompanying the earthquake resulted in the south-westward tilting of a sedimentary basin situated in the hanging wall of the early ruptures, and increased the south-westward dip of the Pliocene and Pleistocene basin sediments. This suggests that the system of faults active in 1980 may have been active since Pliocene time and has been responsible for the evolution of the basin. The individual fault segments responsible for the different sub-events are separated along strike by transverse discontinuities in structure, which control the local geomorphology.

Other intra-Apennine post-lower Pliocene sedimentary basins are likely to be bounded by similar normal faults and should be regarded as areas of high seismic hazard relative to surrounding localities.

**Key words:** Italy, Campania-Basilicata, earthquake, normal-faulting

## 1 Introduction

The Campania–Basilicata earthquake of 1980 November 23 was the largest ( $M_S = 6.9$ ) to have occurred in the southern Apennines of Italy for many years, killing over 3000 people and devastating an area of several thousand square kilometres. Seismic deformation in the Apennines involves mainly normal faulting at crustal depths (e.g. Ritsema 1971; Gasparini *et al.* 1982; Gasparini, Iannaccone & Scarpa 1985; Ghisetti & Vezzani 1982; Anderson 1985; Anderson & Jackson 1987; Westaway 1987a). McKenzie (1972) first suggested that the Apennines are an extensional region between the relatively aseismic Tyrrhenian Sea to the west and the Adriatic Sea to the east. However, until recently little was known about the geometry of the normal faults that move during earthquakes in the Apennines.

In other continental regions, normal-faulting earthquakes nucleate on faults that dip typically in the range  $30^\circ$ – $60^\circ$  and are probably approximately planar from the depth of nucleation (typically in the range 8–15 km) to the surface (Smith & Bruhn 1984; Jackson 1987). These features have been observed in earthquakes in Greece (e.g. Soufleris & Stewart 1981; Jackson *et al.* 1982a), in western Turkey (e.g. Eyidogan & Jackson 1985) and in the western United States (e.g. Doser 1985; Stein & Barrientos 1985). In some larger normal-faulting earthquakes, seismic rupture on very low angle (dip  $< 30^\circ$ ) normal faults in the uppermost lower crust may follow the initial, relatively steep, faulting in the upper crust (Eyidogan & Jackson 1985).

Numerous models have been suggested to explain the occurrence of normal-faulting earthquakes in the Apennines, several of which involve fault geometries different from those known to occur in other regions of continental extension. For example, Mantovani & Boschi (1983) suggested, apparently on the basis of hypocentres at about 40–50 km depth, that normal faulting occurs in the outer margin of a plate that has been partially subducted under Italy from the NE. Ghisetti & Vezzani (1982) and Ghisetti, Scarpa & Vezzani (1982) have suggested that deformation of southern Italy is related to motion on a steep shear zone extending throughout the crust. In the lower crust, they argue, motion on this shear zone is in a reverse-faulting sense and is related to regional compression at depth. Deschamps & King (1984) have suggested that the 1980 Campania–Basilicata earthquake involved brittle deformation at mid-crustal depths between two subhorizontal ductile shear zones.

The problem is further complicated by the lack of agreement as to whether the Apennines are an area of true crustal extension or whether the observed normal faulting is related to regional compression in some complicated way. The Apennines were formed

mainly during Miocene time (e.g. Ippolito *et al.* 1975; Ogniben & Vezzani 1975) by the thrusting together of units of predominantly Mesozoic rocks. Extensive syntectonic 'flysch' deposits were formed at this time as the Apennines were eroded while being uplifted. Subsequently, during the middle Pliocene (Ippolito *et al.* 1975) or middle–upper Pliocene (Ogniben & Vezzani 1975) thrusting ceased and normal faulting started. Pliocene and Pleistocene sediments were then deposited on top of the Mesozoic and 'flysch' units in number of small (around 1–2000 km<sup>2</sup>) intra-Apennine sedimentary basins. Many mapped normal faults can be dated to this age from their relationships with these sediments (e.g. Ortolani 1975). However, some authors (e.g. Reutter, Giese & Closs 1980; Görler & Giese 1978) have dismissed this evidence and suggested that compressional tectonics have continued up to the present.

Many people have carried out specialized studies of the 1980 earthquake and its effects. Seismological studies included locations of the mainshock (del Pezzo *et al.* 1983) and aftershocks (Deschamps & King 1984), and determinations of the mainshock focal mechanism (Gasparini *et al.* 1982; Martini & Scarpa 1983; del Pezzo *et al.* 1983, Deschamps & King 1983) and moment tensor (Boschi *et al.* 1981; Kanamori & Given 1982; Brüstle & Müller 1983). Other studies have investigated elevation changes by levelling (Arca *et al.* 1983; Key & Crosson 1984; Crosson *et al.* 1986), and surface effects (e.g. Bollettinari & Panizza 1981; Cantalamessa *et al.* 1981; Carmignani *et al.* 1981; Cinque, Lambiasi & Sgrosso 1981; Ortolani 1981; Ortolani & Torre 1981; Alexander 1981, 1982; da Roit *et al.* 1983; Gars 1983; Westaway & Jackson 1984). Westaway & Jackson reported more than 10 km of earthquake related surface faulting, most of which had been missed and the rest misinterpreted in the earlier studies. Strong ground motion records have also been studied by Berardi, Berenzi & Capozza (1981) and Fels, Pugliese & Muzzi (1981). Suggestions for the geometry of normal faulting in the mainshock have already been put forward by Deschamps & King (1984), to explain their observations of aftershocks, and by Key & Crosson (1984) and Crosson *et al.* (1986), to explain the pattern of elevation changes. Here, we aim to present a description of the faulting in this earthquake that satisfies all the available types of data. In particular, we aim to address the question of whether a geometry of normal faulting similar to that observed in other regions of continental extension is consistent with the observations of the 1980 earthquake, or whether there is any need to suggest alternative styles of deformation that are unique to the Apennines.

We first describe the observed surface faulting for the mainshock (Section 2), and determine its epicentre (Section 3) and focal mechanism from first-motion polarities (Section 4). We then model the first cycle of long-period teleseismic *P*- and *SH*-waveforms (Section 5), which, we suggest, are caused by interference of the signals from three discrete fault ruptures or subevents. These results are all summarized in Section 6. In Section 7 we investigate the overall moment-tensor for the mainshock, and show that the total scalar moment is approximately double that accounted for by the waveform modelling in Section 5. In Sections 8 and 9 we attempt to constrain the location and timing of the additional subevents that are responsible for this extra seismic moment. In Section 8, we use locally recorded short-period ground acceleration signals to locate the hypocentres of additional subevents. In Section 9 we then use long-period teleseismic body-wave records of these subevents to estimate their orientation and moment. Section 10 discusses the relationship between the faulting in the mainshock and that in its aftershocks.

## 2 Surface faulting

Many people examined the epicentral area of the mainshock, looking for surface faulting produced by it. These initial studies revealed several kilometres of ground cracking in the limestone

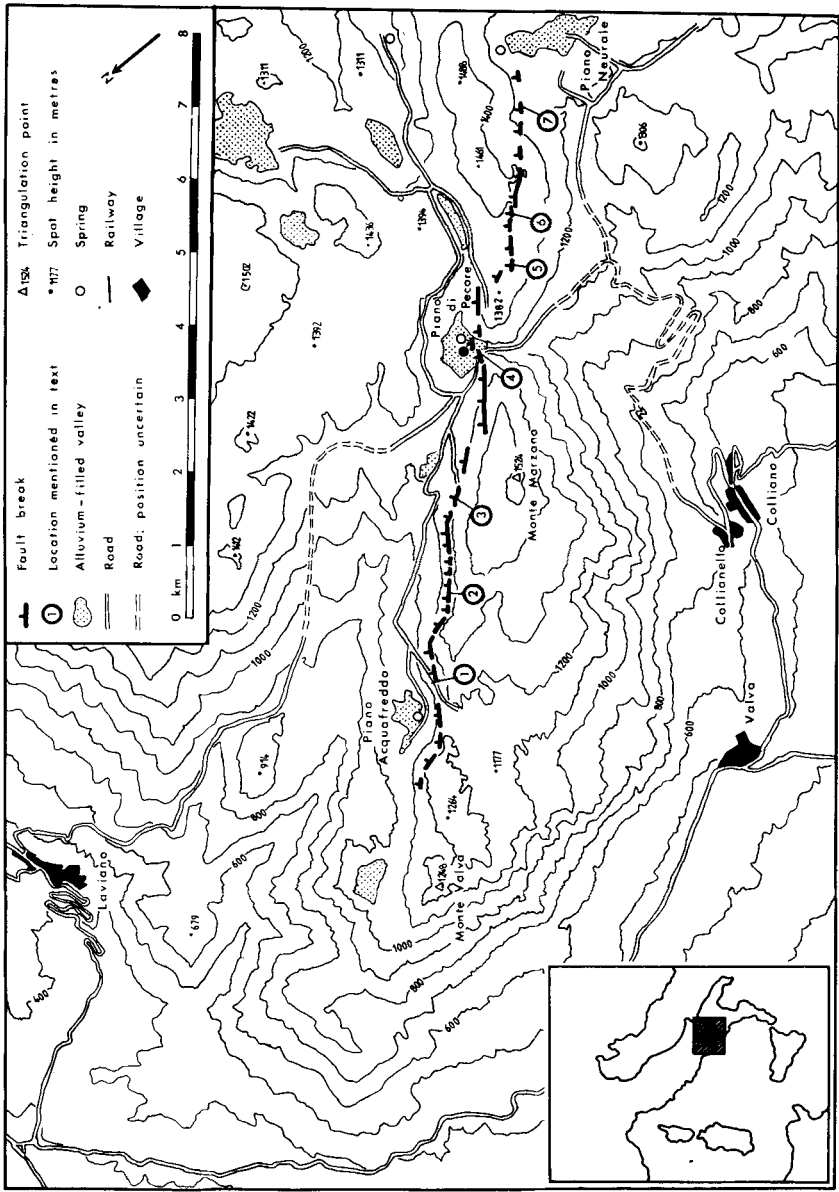
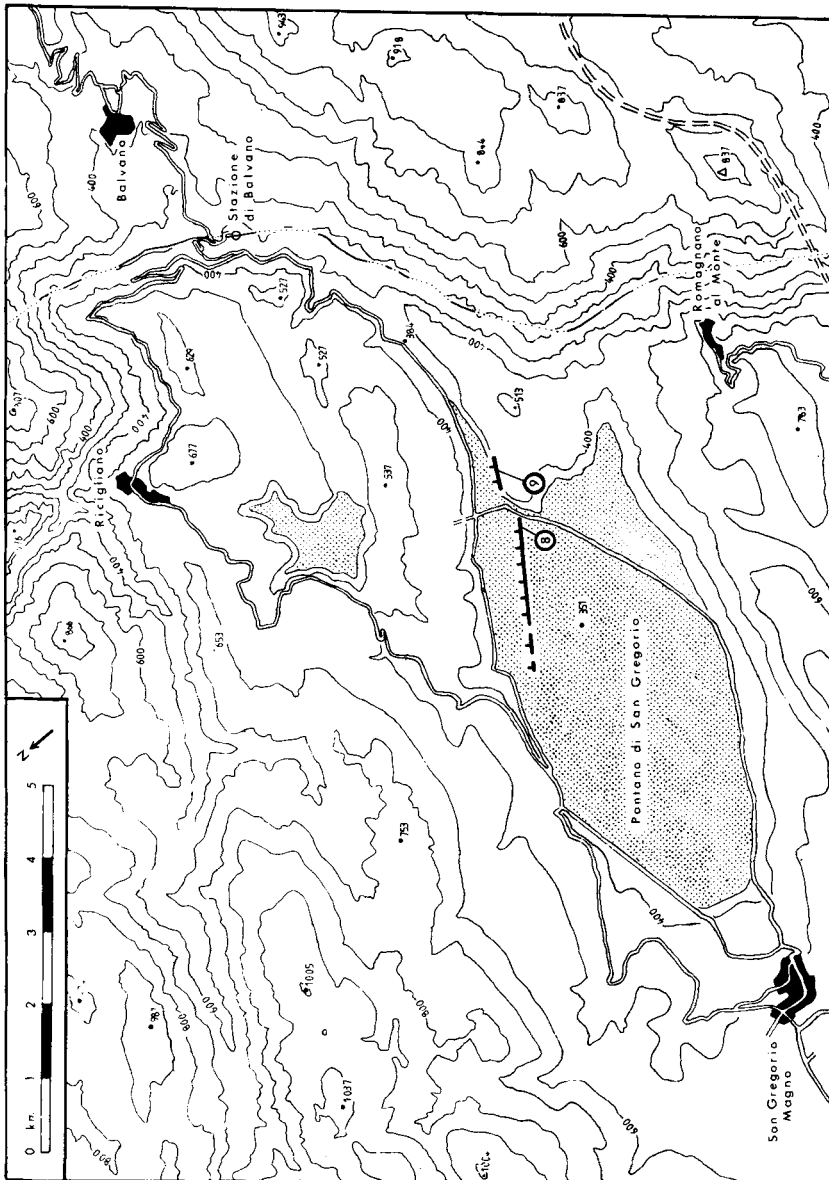


Figure 1. Detailed map of the Monte Marzano segment of surface faulting. Localities where significant exposures exist are numbered. At (1) and (6) features indicate that the same fault has moved in the past: at (1) alluvium in the hanging wall is faulted down against an exposed limestone surface; at (6) a 4 m deep gulley has been eroded along the hanging wall. Around (2) there is a 100 m long continuous exposure of limestone fault surface. The section (3)–(4) was reported by Cinque *et al.* (1981) and Carmignani *et al.* (1981); at (4) the surface faulting crosses a road and is most readily accessible. Between (5) and (7) the uphill side of the faulting is downthrown. The striations discussed in the text were found at locality (7).



**Figure 2.** Detailed map of the San Gregorio segment of surface faulting. Northwest of locality (8) the faulting crossed alluvial deposits in the Pantano di San Gregorio. East of the road, at locality (9), it occurred as an exposed limestone surface.

mountains of the Monte Marzano range (Cinque, Lambiase & Sgrosso 1981; Carmignani *et al.* 1981) (Fig. 1) and near the village of San Gregorio Magno, further SE (Bollettinari & Panizza 1981; Carmignani *et al.* 1981) (Fig. 2). However, none of these early reports concluded that any of the observed features represented surface faulting in the mainshock. The epicentral area was re-examined by Westaway & Jackson (1984), who identified about 10 km of surface faulting in the Monte Marzano range (Fig. 1), part of which included the short section found in the earlier studies. This range of mountains is part of the Campania–Lucania carbonate platform (Ippolito *et al.* 1975); a unit of Mesozoic limestone that forms much of the southern Apennines.

This surface faulting has an overall strike of about  $320^\circ$ , with a downthrow to the NE of up to 1 m. Individual strands of the faulting, up to 1 km in length, are arranged *en echelon*, stepping to the right (Fig. 1). For 6 km, at its NW end, around Monte Valva, the faulting lies along the face of a large north-east-facing topographic escarpment, that has presumably been created by the cumulative effect of faulting in many similar historical earthquakes. At the SE end, 2 km of the faulting are situated such that the downthrown block is on the uphill side. This is strong evidence that the observed feature is not the result of landslides or other superficial processes. Close to its SE end, there is a small exposure of a polished limestone fault surface on which striations are visible. These indicate a rake angle of  $-85^\circ$ , implying that the predominantly normal-faulting earthquake also involved a small component of left-lateral strike slip. Many exposures of limestone fault surfaces, with an average dip of  $62^\circ$  NE, occur along the observed faulting. As will become clear, an additional reason for regarding these Monte Marzano fractures as the surface expression of deeper

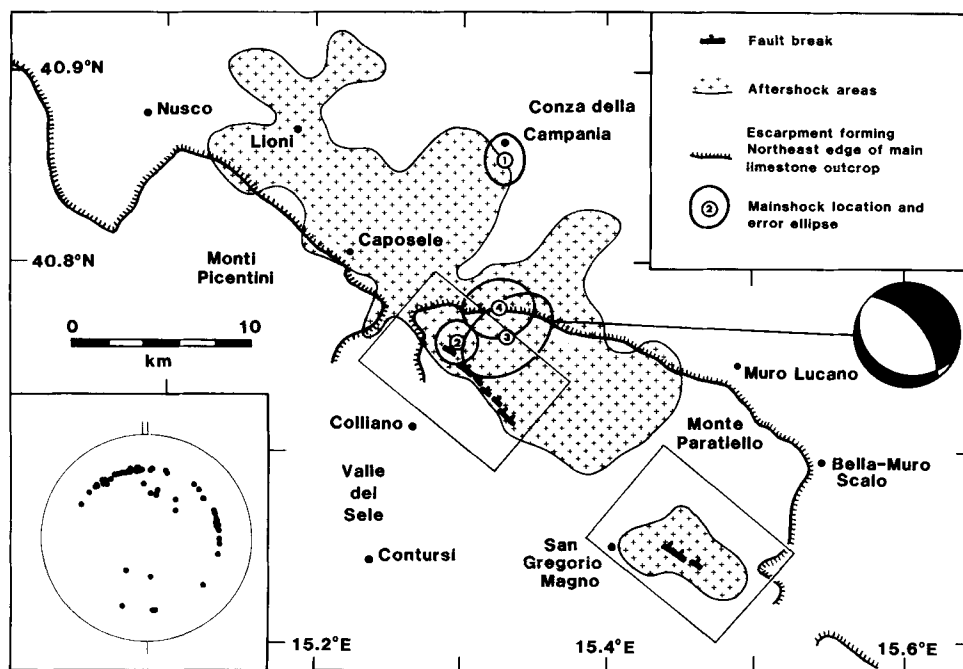


**Figure 3.** Map of the epicentral area, showing mainshock locations (1)–(4) from Table 1, in relation to the areas (shaded) where intense aftershock activity occurred, and in relation to the edge of the outcrop of the Campania–Lucania carbonate platform (with tick marks on the ‘flysch’ outcrops adjacent to it). The inset shows a lower hemisphere equal area projection of the focal sphere indicating the positions of the 63 stations used in location (4). The localities shown in Figs 1 and 2 are outlined.

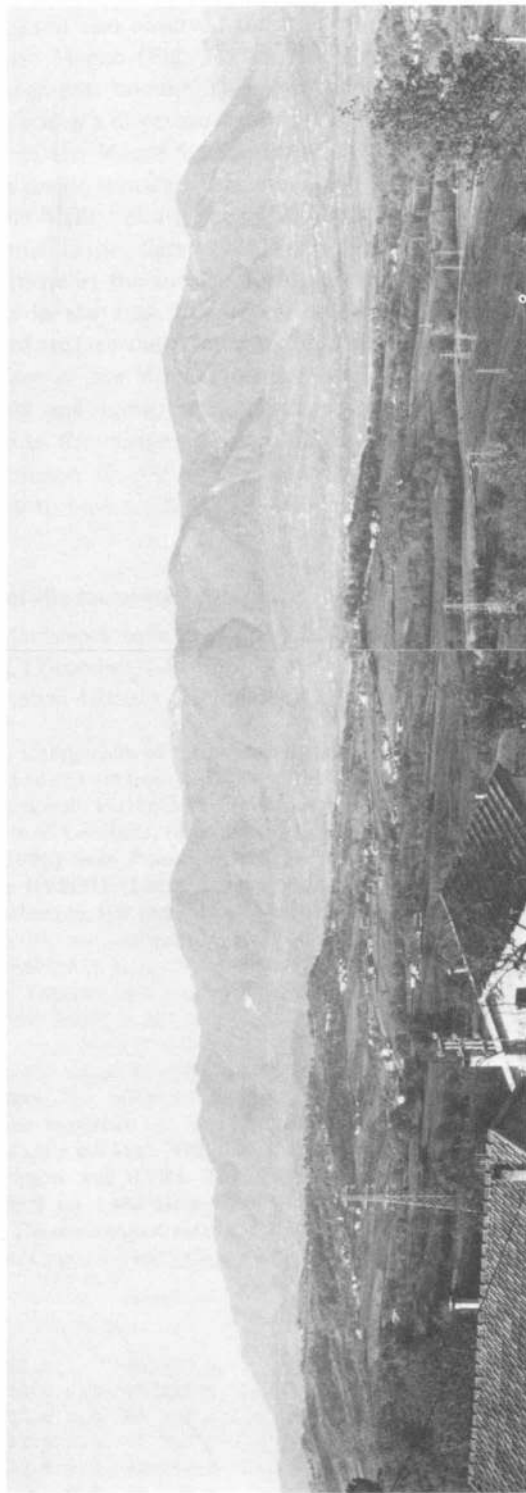


**Plate 1.** View from Sant'Angelo dei Lombardi ( $40.92^{\circ}\text{N}$ ,  $15.18^{\circ}\text{E}$ ) looking S towards the escarpment of the normal fault forming the front of the Monti Picentini range. The escarpment is over 1 km high and extends for 15 km from the northern end of the Sele valley, near Caposele (left) to near Nusco (right). At both ends it is interrupted by transverse discontinuities in geological structure. Waveform modelling (Section 5) and aftershock studies (Fig. 3 and Section 10) suggest that after nucleating further SE the mainshock rupture continued along or parallel to this normal fault, before dying out close to Nusco.

[facing page 380]

faulting in the mainshock, is their location approximately on the updip projection of one of the nodal planes of the first-motion focal mechanism.

Westaway & Jackson also observed that the shorter segment of observed surface faulting, around San Gregorio Magno (Fig. 2), has the same strike as the Monte Marzano segment, and that the two segments line up. This segment does not, however, show any features that conclusively identify it as a direct surface expression of deeper faulting.

At the NW end of the Monte Marzano segment, the general NW trend of the Apennines is interrupted by a major transverse structural discontinuity: the Sele Valley (Valle del Sele in Fig. 3). The Sele Valley is a graben (Ortolani 1975) bounded on its E and W sides by NNE-trending normal faults. Gars (1983) investigated these faults in detail, and concluded that they did not move at the surface during or after the 1980 earthquake, although many landslides occurred in the area. North-west of the Sele Valley, and in line with the Monte Marzano segment of surface faulting, is an abrupt topographic escarpment, over 1 km high, forming the NE face of the Monti Picentini range. This extends for about 15 km past the villages of Caposele and Lioni, before being interrupted by another transverse structural discontinuity close to the village of Nusco (Plate 1 and Fig. 3). This Monti Picentini escarpment was not examined closely by Westaway & Jackson (1984), and we are not aware of any report claiming to have found fresh surface faulting along it, following the 1980 earthquake.

### 3 Determination of the mainshock epicentre

Locations of the mainshock have been published in the bulletins of the International Seismological Centre (ISC) (number 1 in Fig. 3), the US National Earthquake Information Service (NEIS), and the Italian Istituto Nazionale di Geofisica (Table 1) using *P*-wave arrival times

**Table 1.** Comparison of mainshock locations from different sources. Locations (1), (a) and (b) are from bulletins of the International Seismological Centre, the U.S. National Earthquake Information Service, and the Italian Istituto Nazionale di Geofisica, respectively. Location (2) was determined by del Pezzo *et al.* (1983) from *P*-wave arrival times at regional stations, using the location program HYPO71 (Lee & Lahr 1975). We determined location (3) using the same technique, but including *P*-wave data from more stations. We determined location (4), our preferred location, relative to a well-located aftershock. Origin time is quoted in each case to the nearest 0.1 s, and its standard error is given in seconds. Latitude and longitude are quoted in degrees, with standard errors in kilometres. Depth is quoted in km. *N* is the number of stations contributing to each location. Note that the greater the latitude or focal depth of each location, the later the origin time, indicating the extent of trade-off between hypocentral parameters. The preferred relative location, (4), has a covariance matrix of which the longitude (E)–latitude (N) part is  $C_{EE} = 2.7 \text{ km}^2$ ;  $C_{NN} = 2.9 \text{ km}^2$ ;  $C_{EN} = C_{NE} = 0.9 \text{ km}^2$ . The root mean square relative travel-time residual for this location was 0.96 s. The aftershock used as master event occurred at 02:49:38.8 on 1980 December 8, at  $40.805^\circ \text{N}$ ,  $15.229^\circ \text{E}$  and 12 km focal depth. The covariance matrix for its location using temporary local stations includes:  $C_{EE} = 0.5 \text{ km}^2$ ;  $C_{NN} = 0.6 \text{ km}^2$ ;  $C_{EN} = 0.1 \text{ km}^2$ .

Time		Latitude		Longitude		Depth		N	Source
	±		±		±		±		
18:34:53.8		40.900 N		15.400 E		10. FIXED		265	(a)
18:34:52.2	0.1	40.860 N	1.4	15.330 E	1.1	0. FIXED		506	(1)
18:34:52.9	0.3	40.810 N	1.7	15.380 E	2.1	18.0	2.0	36	(b)
18:34:52.5	0.1	40.767 N	1.8	15.300 E	1.4	16.0	1.0	11	(2)
18:34:52.8	0.3	40.762 N	2.4	15.332 E	2.5	15.2	2.6	32	(3)
	0.1	40.778 N	1.7	15.332 E	1.6	FIXED		63	(4)



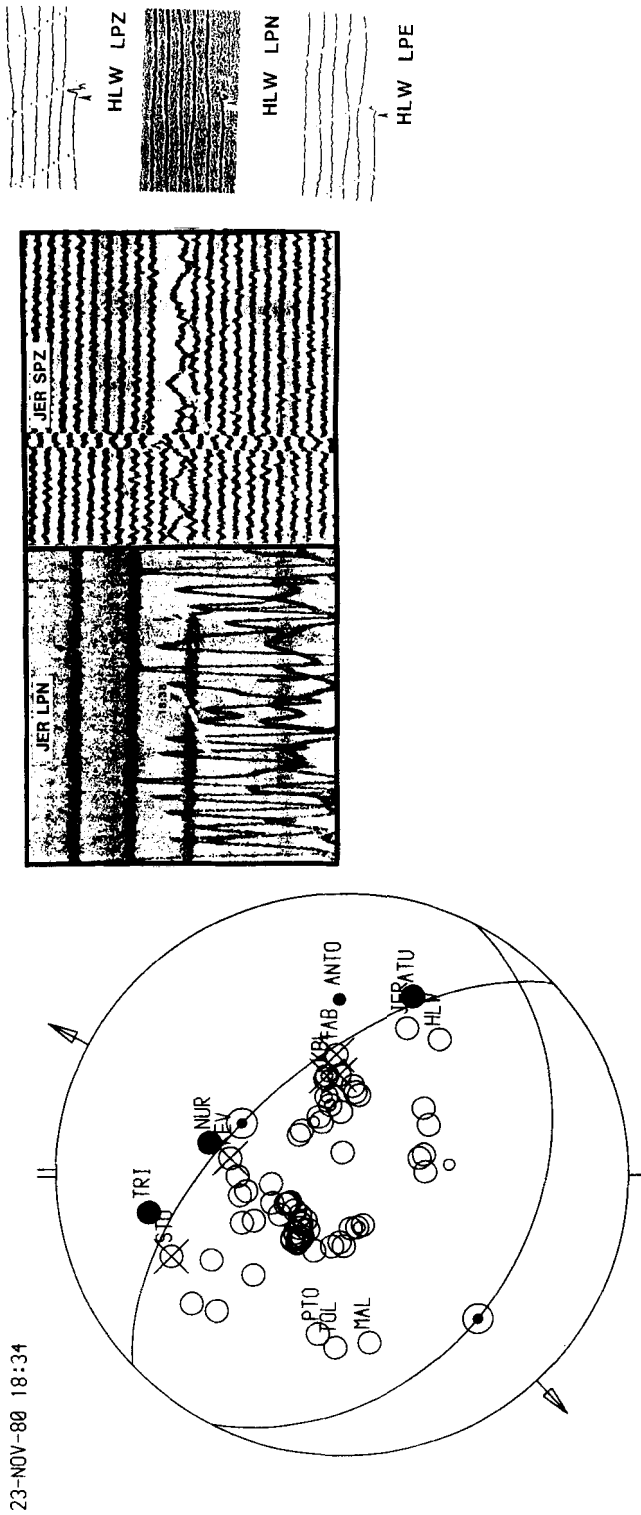
picked at regional and teleseismic stations by station operators. Such locations are likely to be as much as 15–20 km in error (e.g. Soufleris & Stewart 1981; Jackson *et al.* 1982a). Del Pezzo *et al.* (1983) determined the hypocentre (number 2 in Fig. 3) with the location program HYPO71 (Lee & Lahr 1975), using *P*-wave arrival times at 11 stations within 200 km. Since these stations lie only in the NW and SE quadrants, this location is likely to be poorly constrained in the NE–SW direction. We determined the hypocentre (number 3 in Fig. 3) also using HYPO71, but included data from 32 stations within 400 km, in order to provide a better azimuthal distribution. We also determined it relative to one of the largest aftershocks (at 02:49 on 1980 8 December;  $M_L = 4.5$ ), by the technique described by Westaway (1987a), using 63 regional and teleseismic stations that had recorded both the mainshock and the aftershock. This aftershock was independently located by 27 stations of a temporary local seismograph network installed following the mainshock; consequently, its location is reliably known and it can be used as a reference for placing the location of the mainshock relative to it. The standard error ellipses for locations 3 and 4 overlap, but the result of the relative location (number 4) is our preferred solution, as this procedure is less prone to the error caused by lateral variations in velocity structure. This preferred location is beneath the hanging wall of the observed surface faulting, a few kilometres east of the Sele valley. Details of the stations used in these locations are given in Westaway (1985). Note that locations 2, 3 and 4 suggest that the ISC location is misplaced by about 10 km; an amount typical for well-recorded earthquakes in the Mediterranean area (e.g. Soufleris & Stewart 1981; Yielding *et al.* 1981; Jackson *et al.* 1982a). The NEIS location is apparently misplaced by about 20 km.

4 First-motion focal mechanism for the mainshock

Focal mechanisms for the mainshock have been determined from first motion polarities by Gasparini *et al.* (1982), Martini & Scarpa (1983), del Pezzo *et al.* (1983) and Deschamps & King (1983, 1984) (Table 2). Gasparini *et al.* (1982) did not specify the data that were used to constrain their mechanism. However, Martini & Scarpa (1983) and del Pezzo *et al.* (1983) have published a focal mechanism, with the same nodal planes, based on 41 polarity readings at regional and teleseismic stations, including 8 that are inconsistent with the specified nodal planes. Deschamps & King (1983) report a mechanism based on first motion polarities that they read on records from long-period WWSSN (World-Wide Standard Seismograph Network) stations. All these previously published mechanisms have one nodal plane that dips steeply NE and the other, which is less well constrained, that dips at a shallower angle between W and S.

Table 2. Comparison of previously published mainshock focal mechanisms with that determined in this study.

Nodal plane 1		Nodal Plane 2		
Dip	Strike	Dip	Strike	
64	298	29	145	Gasparini <i>et al.</i> (1982), Martini & Scarpa (1983), del Pezzo <i>et al.</i> (1983).
60	320	54	075	Deschamps & King (1983), Deschamps & King (1984).
59	317	31	127	Westaway & Jackson (1984), This study.



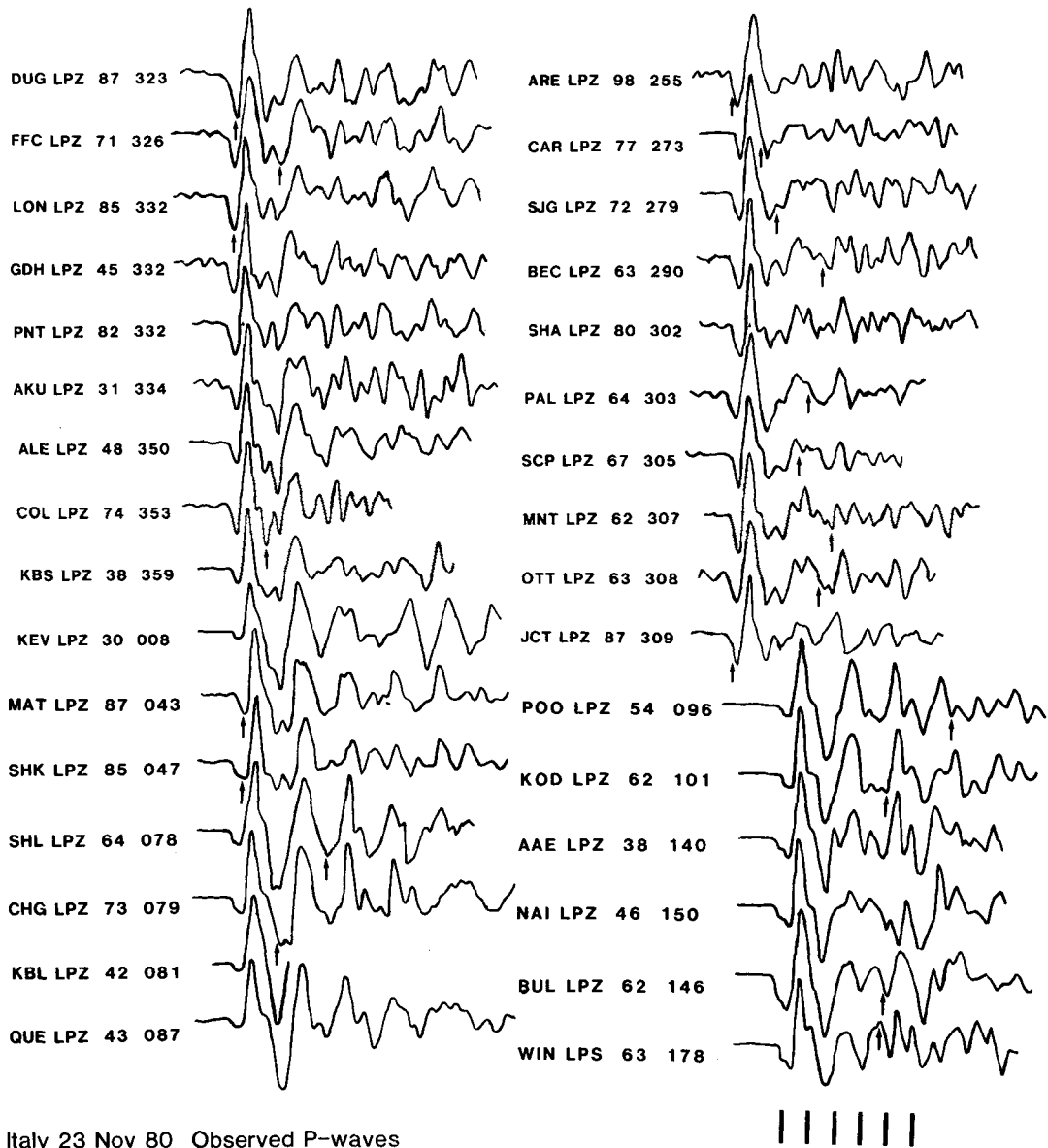
**Figure 4.** Our preferred focal mechanism for the *P*-wave first motion, based on polarities that we have read at long-period stations. A lower hemisphere, equal-area projection of the focal sphere described in the text has been used. Stations that recorded compressional first motions (ATU, NUR, TRI and ANTO) are shown as filled circles, and dilatations (AAE, AAM, AKU, ALE, ALQ, ANT, AQU, ARE, BAG, BEC, BLA, BUL, CAR, CHG, COL, COR, DAG, DUG, ESK, FFC, FVM, GBA, GDH, GEO, HKC, HLW, JCT, JER, KBC, KOD, LON, LOR, MAL, MAT, MNT, NAI, NIL, NNA, NUR, OTT, PAL, PNT, POO, PRE, PTO, SCP, SHA, SHK, SHL, SIG, SNG, TOL, TRN, TUL, VAL, WES, WIN, WRA, YKA, ANMO, BCAA, CHTO, KAAO, SHIO, TATO and ZOBO) as open circles. Crosses (at KBL, KEV, QUE, STU and TAB) indicate first motions that we believe to be genuinely nodal. Polarities measured on SRO and ASRO records (ANMO, ANTO, BCAA, CHTO, KAAO, SHIO, TATO and ZOBO) are indicated by smaller symbols. The slip vectors on both nodal planes, and their horizontal projections, are marked. The insets show waveforms from the critical stations HLW and JER.

Fig. 4 shows a new focal mechanism based on the first motion polarities at 74 long-period stations. The focal sphere in Fig. 4 was centred at  $40.7^{\circ}\text{N}$ ,  $15.3^{\circ}\text{E}$ , 10 km depth, and station positions were calculated using a  $P$ -wave velocity of  $6.8\text{ km s}^{-1}$  below the source. Nodal planes for this mechanism are listed in Table 2. The slip vector on the NE-dipping nodal plane has been constrained to have the same rake as the observed striations on the Monte Marzano segment of surface faulting, discussed in Section 2. The NE-dipping nodal plane is constrained by compressional first motion polarities at ATU, NUR and TRI and by nodal dilatations at TAB, QUE, KBL, KEV and STU. The principal difference between the mechanism of Deschamps & King (1983) and those of Gasparini *et al.* (1982), Martini & Scarpa (1983) and del Pezzo *et al.* (1983) is that Deschamps & King found a large component of left-lateral strike slip on the NE-dipping nodal plane. Deschamps & King constrained the SW-dipping nodal plane using the form of the onset at HLW, which they read as a nodal compression. Fig. 4 shows the three long-period records from HLW, marked to indicate the arrival time of the  $P$  phase read from the short-period record. The first motion, of small amplitude, is down on the vertical component and to the N and W on the horizontal components. Since HLW is SE of the epicentre, all three long-period records from HLW are consistent with the onset being dilatational. The compressional pulse read by Deschamps & King occurs 3 s after the short-period  $P$ -wave arrival time. Fig. 4 also shows the long-period north and short-period vertical component records from JER. The  $P$ -wave first motion on the short-period record coincides with the minute marker at 18:39. The record is of poor quality but indicates that the first 2.5 s of the signal is a low-amplitude pulse towards the N followed by a much larger pulse of opposite polarity. Since JER is also SE of the source, this appearance is consistent with the arrival being a nodal dilatation. Because of multipathing in the distance range  $15^{\circ}$ – $25^{\circ}$ , the apparently nodal character of the onsets of HLW and JER (and also at TOL,  $15^{\circ}$ , and MAL,  $16^{\circ}$  distant, neither of which is critical for constraining the focal mechanism) should be disregarded in constraining the focal mechanism, though the observed polarities are reliable. This means that there are no stations suitably positioned to provide any strong constraint from first motion polarities on the orientation of the SW-dipping nodal plane.

The SW-dipping nodal plane in Fig. 4 can be rotated by up to  $20^{\circ}$  in strike in either direction without introducing any inconsistency with the observed first motion polarities. Thus a mechanism similar to that by Gasparini *et al.*, Martini & Scarpa and del Pezzo *et al.*, with a null axis dipping gently NW, is consistent with all observed polarities. However, a mechanism with a null axis dipping steeply E, like that of Deschamps & King, is not consistent with the first motion polarity at HLW. In our focal mechanism presented in Fig. 4, we have orientated the SW-dipping nodal plane to give the rake angle on the NE-dipping nodal plane indicated by the striations found on the surface fault break at locality 7 in Fig. 1. This orientation is confirmed by the results of our body-wave modelling presented in Section 5.

## 5 Modelling the long-period waveforms of the early mainshock ruptures

We have used the standard technique of Langston & Helmberger (1975), described in detail by Soufleris & Stewart (1981) and many others, to model the first 15 s duration of long-period teleseismic  $P$  and  $SH$ -waves recorded at WWSSN and Canadian WWSSN-compatible stations.  $P$ -wave records were digitized, corrected for skew due to the helical record layout, scaled to a uniform timebase and normalized in amplitude (Fig. 5).  $SH$ -waveforms were obtained from the two horizontal components of motion by resolving in the direction



Italy 23 Nov 80 Observed *P*-waves

**Figure 5.** Normalized long-period vertical component *P*-waveforms from WWSSN and Canadian WWSSN-compatible stations. Arrival times of *PcP* are indicated by a marker below each seismogram. The interval between *P* and *PcP* was calculated using the travel time tables of Herrin (1968). Numbers following each station code are the distance and azimuth to the station, measured at the source, both in degrees. Timing markers are shown every 10 s.

perpendicular to the azimuth at which the *S*-wave arrived at each station (Fig. 6). The sign convention used for polarities of *SH*-waveforms is from Aki & Richards (1980).

The early part of the *P*-wave records is dominated by the *W* pattern caused by interference between the direct *P*-wave and surface reflected phases *pP* and *sP* (e.g. Soufleris & Stewart 1981). On many records, however, two important additional features are apparent. First, the duration of the first downswing at stations to the S and E is about 6 s,

which is 2 s longer than at stations to the N and W. At some stations in the SE quadrant (CHG, SHL, SHK, AAE, NAI, BUL and WIN) an inflexion is observed in this first downswing 3 s after the start of the record. No equivalent inflexion is observed in stations in the NW quadrant. A plausible explanation of these observations is that the initial part of the waveform shows the effect of two separate source ruptures, with the second occurring NW of the first (see, e.g. Yielding *et al.* 1981, or Berberian *et al.* 1984, for similar arguments). Secondly, most records also contain another inflexion in the second downswing. The timing of this feature is also azimuthally dependent, being about 13 s after the start of the record at stations to the north and west, and 14 s at stations to the S and E. This inflexion retards the downswing by about 1.5 s at most stations. These two features in the waveforms are also observed on the horizontal component records (Fig. 6b), suggesting that they represent the *P*-wave signal from the source (i.e. with the same ray parameter as the first arrival), and are not conversions below the receiver.

Modelling of long-period teleseismic *P*-waveforms for this earthquake has already been attempted by Deschamps & King (1983). Their study only considered source models involving a single rupture, and did not attempt to model either of the two inflexions identified above that provide evidence for source complexity. In addition, the focal mechanism that Deschamps & King determined and used in their waveform modelling study is inconsistent with the true *P*-wave first motion at HLW.

We now investigate the observed complexities in the seismograms and see whether they are related to complexities in the seismic source. In a study of this type, it is not possible to prove that any feature in a waveform is definite evidence for source complexity. However, if a feature can be modelled as a source complexity, and then independent evidence can be found that is consistent with the same source model, then that interpretation becomes convincing. In addition to that caused by the source itself, complexity can also be introduced into waveforms by propagation through an inhomogeneous medium. In order to minimize the distorting effects of propagation through the lithosphere and uppermost asthenosphere, modelling has only been carried out for records from the distance range  $30^{\circ}$ – $80^{\circ}$  for *P*-waves and  $45^{\circ}$ – $80^{\circ}$  for *SH*-waves. Crustal structure around either the source or the receiver could also affect the observed waveforms. It is unlikely that the observed inflexions are the result of receiver crustal structure, because different stations at similar azimuths have very similar waveforms (Fig. 5). This similarity is our justification for selecting representative small samples of the available waveforms in later figures. It is not possible to eliminate near-source crustal structure as the cause of the complexity, although it is worth noting that *P*-waveforms from other earthquakes that occurred in 1962 in the same area do not show the features mentioned above (Westaway 1987a). No attempt will be made here to investigate the effect on teleseismic waveforms of complicated near-source velocity structures. Instead, the waveforms will be modelled as due to source complexity, then independent evidence will be examined to see if it can be reconciled with the source model that is determined.

Source and receiver velocity structures used in our modelling procedure are listed in the caption for Table 3. Attenuation due to anelasticity in the mantle was modelled using a Futterman (1962) operator with  $t^*$  equal to 1.0 s for *P*-waves and 4.0 s for *S*-waves; values recommended for long-period waveform modelling by Helmberger (1983). The stations used in the waveform modelling are shown in Fig. 6(c).

### 5.1 THE FIRST TWO SUB-EVENTS

Because the first cycle of the observed waveforms at all stations involves interference of at

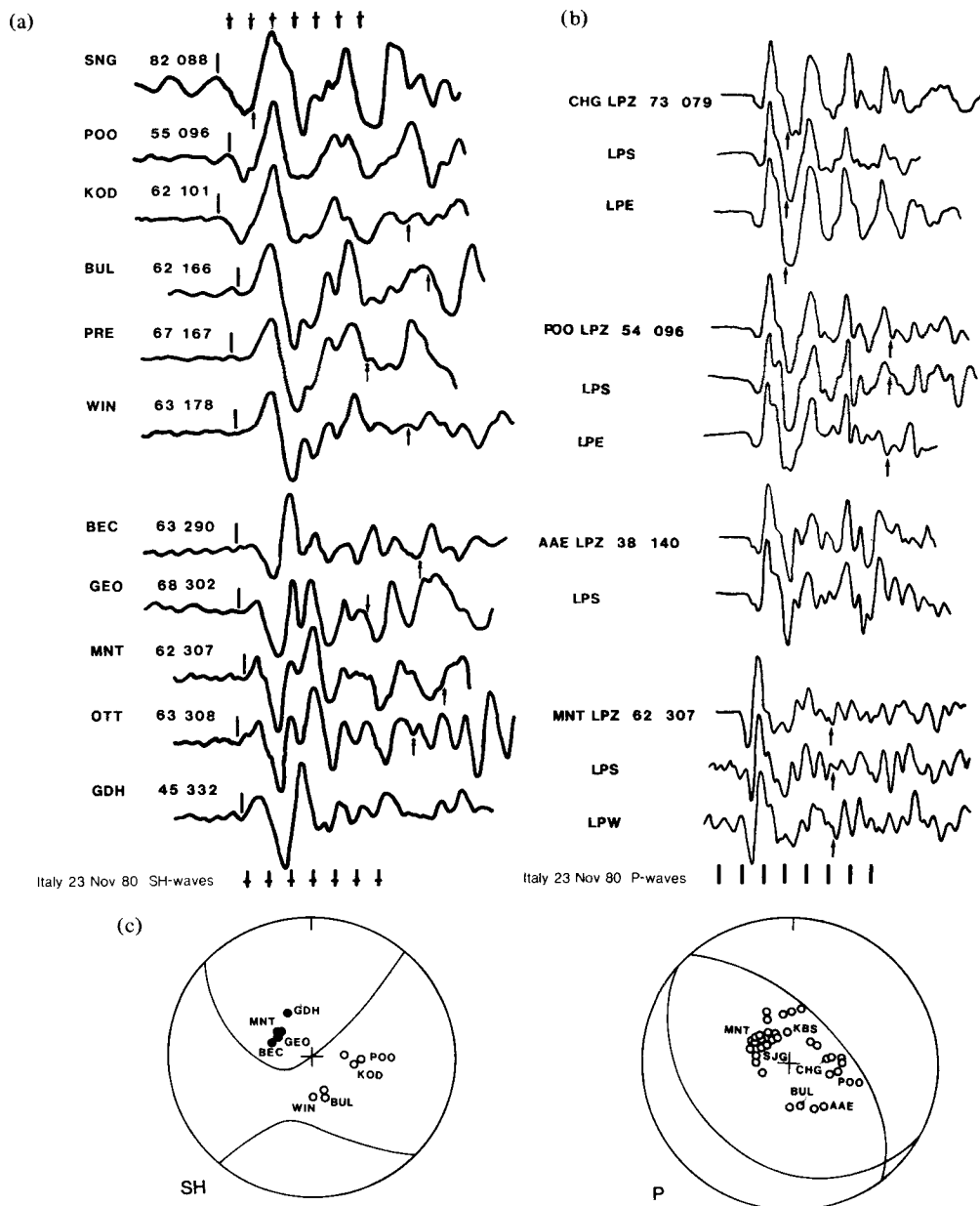


**Figure 6.** (a) Normalized long-period *SH*-waveforms from WWSSN and Canadian WWSSN-compatible stations. *S*-wave arrival times predicted using Jeffreys & Bullen (1967) travel-time tables are indicated by vertical bars. These are up to 5 s different, at some stations, from the true arrival times, estimated by matching observed and synthetic waveforms, due to lateral variations in *S*-wave velocity within the earth. Timing markers are shown every 10 s. The arrival times of *ScS*, also determined using Jeffreys & Bullen tables, are indicated with pointers by the records. At several stations a signal arriving at the predicted time for *ScS* has a relatively large amplitude. (b) Vertical and horizontal component long-period *P*-waveforms from CHG, POO, AAE and MNT. (c) Our preferred *P*- and *SH*-wave focal mechanisms for the first main-shock subevent, indicating the positions on the focal sphere of all stations from which waveforms were available. The stations selected for waveform modelling are identified by their three-letter codes. Open circles indicate stations where dilatational *P*- or negative *SH*-wave polarities are expected. The projections used are the same as that in Fig. 4.

least two discrete source ruptures or subevents, no attempt is made here to model the source as a single rupture. If these two subevents are assumed to have the same focal mechanism and focal depth, their timing and relative moments can be determined. The best match between observed and synthetic waveform shapes occurs with both subevents at 10 or 12 km focal depth, with the moment of the second subevent 2.5 times that of the first, a delay time of 2.5 s, and with the second subevent offset 8 km NW of the first (Fig. 7). Both subevents were assumed to have symmetrical triangular source time-functions of 4 s total duration. Fig. 8 indicates the effects on the observed *P*-waveforms at POO and AAE of varying the relative moments, the delay time and spatial offset, and the focal depths of the two subevents. Comparison of observed and synthetic absolute amplitudes implies a moment of  $2.5 \times 10^{18}$  Nm for the first subevent and  $6.2 \times 10^{18}$  Nm for the second. The uncertainty in these values, caused by mismatch in amplitudes at some stations, is in the region of 20 per cent. The waveforms are sensitive to changes in relative moment, offset and time delay. In contrast to the waveforms produced by a single source, they are relatively insensitive to small changes in focal depth or time-function. However, at focal depths shallower than 8 km the double pulse in the first downswing is not observed at any azimuth, as the effect of *pP* from the first subevent overcomes that of *P* from the second. At depths greater than 16 km an inflexion, that is not observed on any record, occurs on the first upswing. Thus, the focal depth of the two subevents is constrained within the range 8–16 km, with our preferred depth at 10 km. In contrast, Deschamps & King (1983) determined the focal depth of their single source, which they estimated to have a time-function of 7 s duration, to be 16 km.

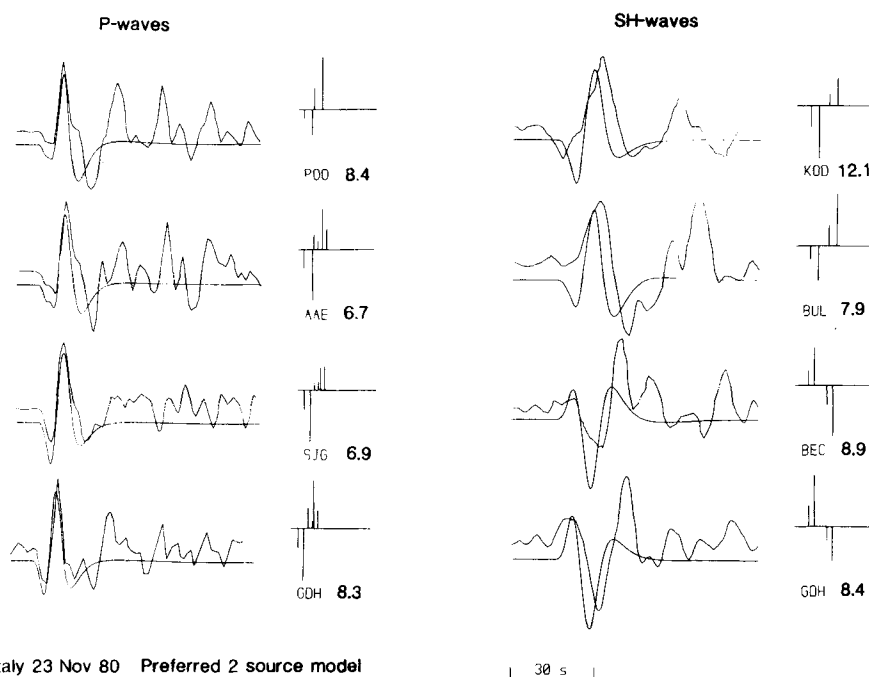


**Figure 7.** Observed and synthetic *P*- and *SH*-waveforms for our preferred two-source model. Here and in subsequent figures, the number to the right of each station code is the moment needed, scaling all subevents within the source in equal proportion, to match the amplitudes of the observed and synthetic waveforms at each station. The bars above each station code indicate the timing and relative amplitudes of the *P*, *pP* and *sP* contributions to the synthetic seismograms.

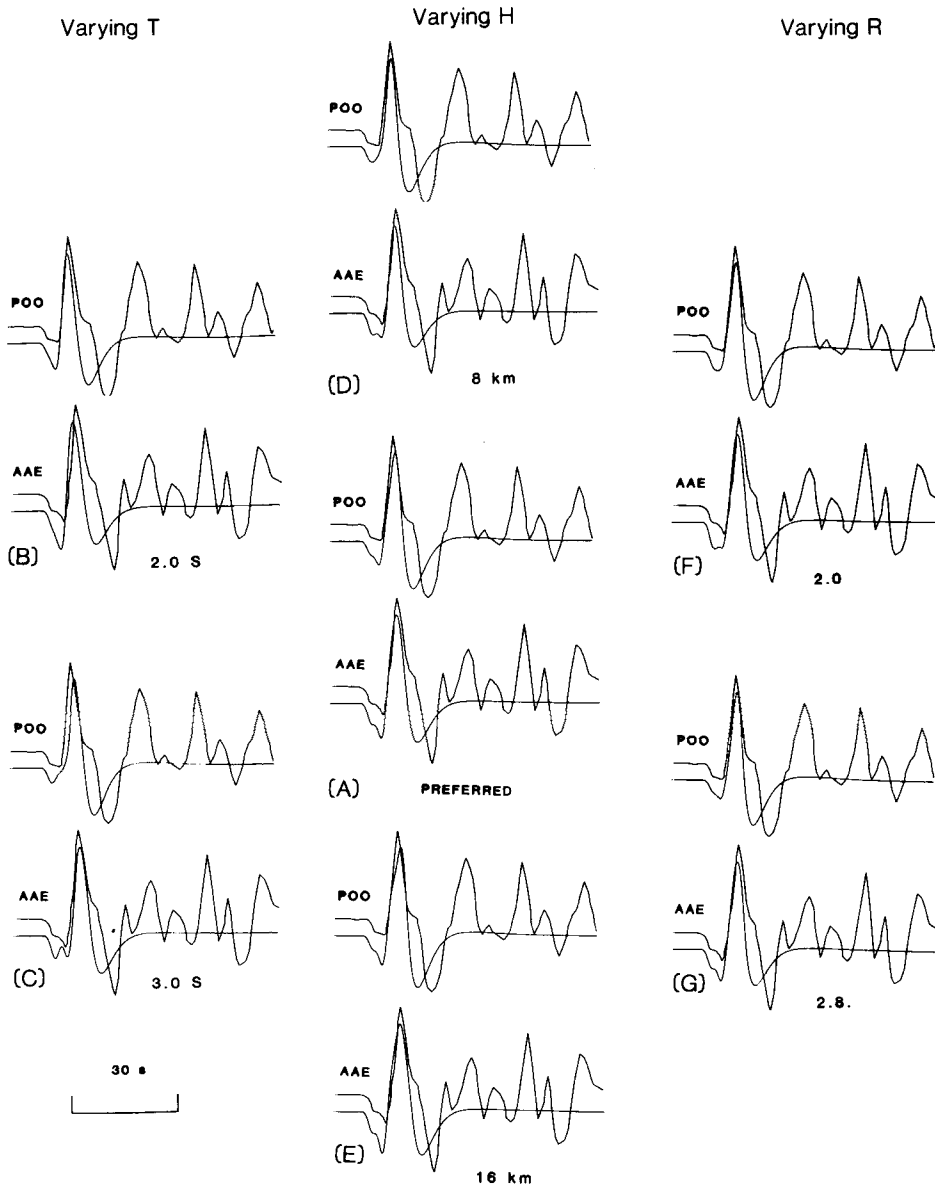


**Figure 8.** Effect on synthetic long-period  $P$ -waveforms at POO and AAE of varying the ratio of seismic moments  $R$ , the delay time  $T$ , and the focal depth  $H$  of the two sources about the values determined in the preferred two-source model: (a)  $R = 2.5$ ,  $T = 2.5$  s,  $H = 10$  km (preferred); (b)  $R = 2.5$ ,  $T = 2.0$  s,  $H = 10$  km; (c)  $R = 2.5$ ,  $T = 3.0$  s,  $H = 10$  km; (d)  $R = 2.5$ ,  $T = 2.5$  s,  $H = 8$  km; (e)  $R = 2.5$ ,  $T = 2.5$  s,  $H = 16$  km; (f)  $R = 2.0$ ,  $T = 2.5$  s,  $H = 10$  km; (g)  $R = 2.8$ ,  $T = 2.5$  s,  $H = 10$  km.

Their greater focal depth and longer time-function result from having assumed that the whole of the first downswing on the observed seismograms was caused by a single subevent, illustrating the importance of correct parameterization of source time-functions for the accurate determination of focal depth (see, e.g. Nabelek 1984).

Observed and synthetic  $P$ -waveforms for the preferred two-source model are shown in Fig. 7. This model can account for the azimuthal dependence of the shape and duration of



the first cycle of these waveforms. Fig. 7 also shows observed and synthetic *SH*-waveforms for stations POO and KOD using the same source model. These synthetic waveforms have the correct polarity, though the duration of their first cycle is too short.

## 5.2 THE THIRD SUB-EVENT

The duration of the observed *SH*-wave records and the inflexion in the second downswing of the observed *P*-wave records may both be explained by the inclusion of a third subevent. The interval between the first motion and the inflexion in the second downswing of the

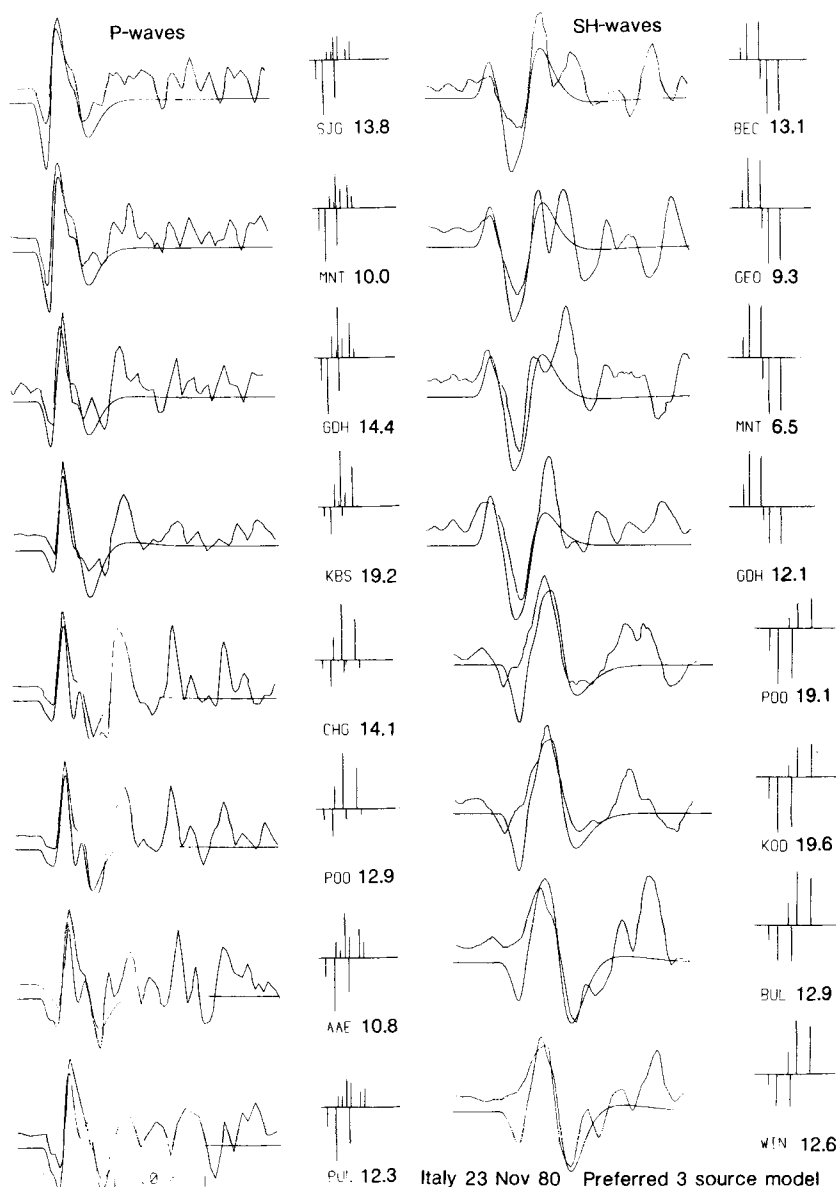


**Figure 9.** Observed and synthetic long-period *P* (left) and *SH* (right) waveforms for our preferred three-source model.

teleseismic *P*-waveforms is approximately 2 s longer at stations to the SE than at stations to the NW, suggesting that the third subevent, like the second, is to the NW of the first. This inflexion looks very similar at all available teleseismic stations, suggesting that all these stations lie in a single quadrant of the *P*-wave radiation pattern for the third subevent. The effect of the third subevent on teleseismic *SH*-waveforms is to broaden them but in other respects to leave their form largely unchanged in comparison with synthetic waveforms for the first two subevents alone. This implies that the orientation of the third subevent source is similar to that of the first two. Our modelling indicates that synthetic seismograms are very sensitive to the origin time of the third subevent. Observed *P*-wave seismograms can only be matched when the third subevent is initiated between 6.5 and 7.5 s after the first. Our best-fitting model (Fig. 9) indicates that the position of the third subevent is 14 km NW of the first, but sources up to 5 km away from this point result in only a marginally worse fit. With a delay relative to the first subevent of 7 s, any source within 21 km of the first subevent is causal, assuming a rupture velocity no greater than 3 km s<sup>-1</sup>. Over 200 sets of synthetic seismograms were generated, incorporating this extra subevent, in order to determine a satisfactory match to the *P*-wave records, allowing all parameters describing the third subevent to vary. The third subevent produces the inflexion in the second downswing of the *P*-wave records because the compressional backswing from its own dilatational *P* pulse interferes with the dilatational backswing of the compressional pP and sP pulses from the first two subevents. In order to obtain synthetic seismograms with inflexions of the correct amplitude at all stations, we found that the NE-dipping nodal plane must be slightly steeper

**Table 3.** Our preferred source model from teleseismic waveform modelling. For each subevent, *T* is the origin time in seconds, *X* the westward offset in km, *Y* the northward offset in km, all relative to the first subevent, and *H* the focal depth, in km. *M*<sub>0</sub> is the seismic moment in 10<sup>18</sup> Nm; *φ* the strike, *δ* the dip and *λ* the rake, all in degrees. *T*<sub>R</sub>, *T*<sub>P</sub> and *T*<sub>F</sub> are the rise time, plateau time and fall-off time of the source time-function, all in seconds. We have assumed, throughout, a near-source velocity structure consisting of a layer 6 km thick, with *P*-wave velocity 4.5 km s<sup>-1</sup>, *S*-wave velocity 2.6 km s<sup>-1</sup> and density 2800 kg m<sup>-3</sup>, above a layer with *P*-wave velocity 6.8 km s<sup>-1</sup>, *S*-wave velocity 3.9 km s<sup>-1</sup> and density 3000 kg m<sup>-3</sup> that contained the seismic sources. Beneath this was material with *P*-wave velocity 8.0 km s<sup>-1</sup>, representing the mantle. The velocity in the crustal layer containing the source was chosen to be the same as that used in the focal mechanism described in Section 4. The near-surface layer was to allow for low velocity material above the hypocentre when modelling delay times of surface reflections. Velocity structure within the crust beneath all stations was assumed to consist of a single layer with *P*-wave velocity 6.0 km s<sup>-1</sup>, *S*-wave velocity 3.4 km s<sup>-1</sup> and density 3000 kg m<sup>-3</sup>.

	<i>T</i>	<i>X</i>	<i>Y</i>	<i>H</i>	<i>M</i> <sub>0</sub>	<i>φ</i>	<i>δ</i>	<i>λ</i>	<i>T</i> <sub>R</sub>	<i>T</i> <sub>P</sub>	<i>T</i> <sub>F</sub>
(1)	0.0	0.0	0.0	10.	2.5	317	59	-85	2.0	0.0	2.0
(2)	2.5	5.5	5.5	10.	6.2	317	59	-85	2.0	0.0	2.0
(3)	6.8	10.0	10.0	10.	4.5	317	64	-85	2.3	0.0	2.0
(4)	12.8	-16.0	-16.0	10.	2.0	317	65	-85	2.0	0.0	2.0
(5)	19.0	0.0	6.0	12.	4.0	320	20	-105	4.0	0.0	4.0
(6)	38.0	0.0	12.0	12.	3.0	320	20	-105	2.0	0.0	2.0

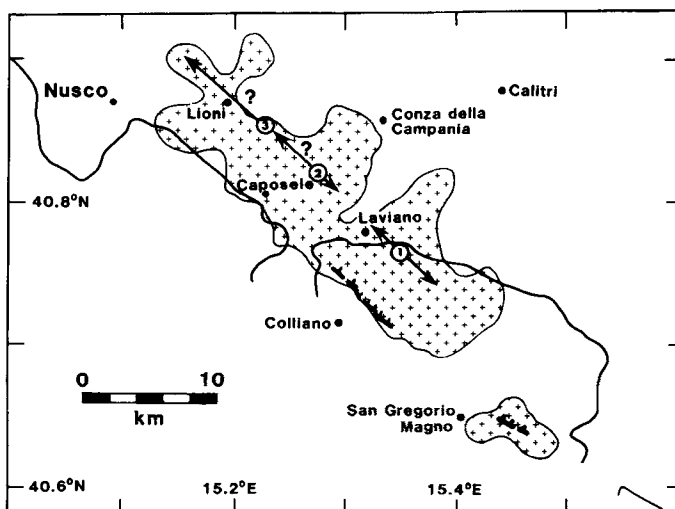
in the third subevent than in the first two, so that the direct *P*-wave for stations to the east takes off close to this nodal plane. Otherwise the upswing produced by the third subevent at stations to the E is too large. A moment of  $4.5 \times 10^{18}$  Nm is estimated for the third subevent. It is interesting to note that the larger the moment of this third subevent, the smaller the amplitude of the synthetic *P*-wave seismograms. This is because of the destructive interference between the upward backswing from the first two subevents and the dilatational *P* pulse from the third subevent. The focal depth of the third subevent is constrained by the timing of the inflexion in the second downswing of the *P* waveforms. This inflexion disappears from the synthetic seismograms if the depth is less than 8 km and is too late if the depth is greater than 14 km. Our preferred depth is 10 km. Table 3 describes fully this three-source model for the early mainshock ruptures. The locations of the sources are shown in Fig. 10(a).

The least satisfactory feature of the match between observed and synthetic seismograms is the negative polarity first pulse of the synthetic *SH*-waves at stations BUL and WIN, to the S. The Jeffreys & Bullen (1967) arrival time of *SH* is approximately 5 s before a large positive *SH*-wave pulse, which matches the first upswing in the synthetic *SH* records. The form of the observed *SH* onset suggests that these southern stations are close to a nodal surface in the *SH*-wave radiation pattern. The amplitude of the negative *SH* onset at these stations can be reduced by small changes in the orientation of the focal mechanism, but only at the expense of making it inconsistent with the observed *P*-wave polarities at ATU and NUR. No source model could be found that satisfies both the *SH*-wave polarities at BUL and WIN, and is consistent with all observed *P*-wave polarities. It is possible that the apparently nodal *SH* onsets at these southern stations are produced by destructive interference between a negative *SH* pulse and a positive pulse forming part of the *P*-wave coda.

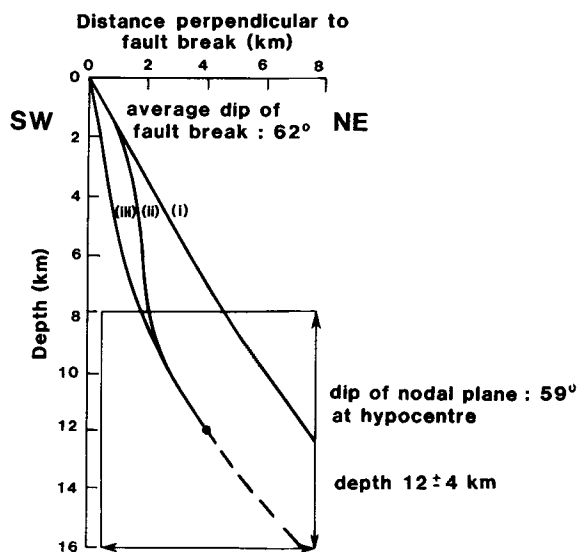
## 6 Summary of observations concerning the early mainshock ruptures

The focal mechanism for the mainshock involves normal faulting with nodal planes striking NW and SE (Table 2 and Fig. 4). Observations of surface faulting extending for more than 10 km (Fig. 1), and measurements of elevation changes (Arca *et al.* 1983) obtained through releveling, show that this NE-dipping nodal plane is the fault plane. Our preferred mainshock hypocentre indicates that the earthquake nucleated underneath the NE edge of the outcrop of the Campania–Lucania carbonate platform (Fig. 3). This is in contrast to agency locations that are systematically mislocated further N. It has been suggested (Deschamps & King 1983) that the earthquake involved faulting on the NE edge of the Campania–Lucania carbonate platform. The mainshock hypocentre and surface faulting presented here do not support this suggestion; instead, they are consistent with the earthquake having nucleated on a normal fault situated within the limestone mountains that form the Campania–Lucania carbonate platform (Fig. 3).

Fig. 10(b) shows a NE–SW cross-section indicating the relative positions of the surface faulting and the hypocentre. The dip of the NE-dipping nodal plane in the mainshock focal mechanism is slightly less than the average dip of the surface faulting. If the mainshock is assumed to have nucleated near the NE surface of its error ellipsoid, then a downward continuation of the surface faulting passes close to this hypocentre. The relative positions of the hypocentre and the surface faulting thus suggest that the fault which moved is approximately planar from the surface to the depth at which the earthquake nucleated. Such a planar geometry is seen for other active normal faults for which earthquake source



(a)



(b)

**Figure 10.** (a) Inferred extent of the three sources in the preferred three-source model, shown in relation to the areas (shaded) where intense aftershock activity occurred, and in relation to the edge of the outcrop of Mesozoic limestone of the Campania–Lucania carbonate platform. (b) Section striking SW–NE, across the Monte Marzano segment of surface faulting, indicating the relative positions of this faulting and the hypocentre of the first mainshock subevent. Our waveform modelling (Fig. 8) indicates a focal depth between 8 and 16 km for this subevent, with a preferred value 10 km. Our preferred location (Table 1) has uncertainty in its horizontal position (95 per cent confidence limit, or double the standard error) of 3.6 km in the plane of the section. The mean dip of the surface faulting, measured by Westaway & Jackson (1984) at places where planar limestone surfaces were exposed, was  $62^\circ$  NE. The corresponding nodal plane of the focal mechanism (Fig. 4) dips at  $59^\circ$  NE. Three interpretations are suggested: (i) The true hypocentre was at 12 km depth, 3 km NE of its preferred position, and the fault dip increased slightly from  $59^\circ$  to  $62^\circ$  NE from the hypocentre to the surface, (ii) The hypocentre was at location (4), and the fault surface has an S-shaped curvature, (iii) The hypocentre was at location (4), and the fault steepens towards the surface.

parameters are well resolved (e.g. Jackson & McKenzie 1983; Eyidogan & Jackson 1985; Stein & Barrientos 1985).

Body-wave modelling indicates that a moment of about  $2.5 \times 10^{18}$  Nm was released in the first subevent of the mainshock. If the shear modulus of the rocks involved in this faulting was  $3 \times 10^{10}$  Nm<sup>-2</sup> and the fault that moved extended 10 km along strike, and from the surface to 10 km depth at a dip of 60°, then the average displacement on the fault expected would be 0.8 m, and is thus in good agreement with the average value of 1.0 m observed for the surface faulting around Monte Marzano. The available data is therefore consistent with the first subevent corresponding to the motion that formed the Monte Marzano segment of faulting. The positions of the second and third subevents inferred from teleseismic waveform modelling suggest that after initiating on the eastern side of the Sele valley, the rupture propagated across it and continued northwestwards. The third subevent has similar moment to the first one, and so, presumably, involved a similar amount of slip on a fault of similar area. The second subevent was larger. Thus, the inferred NW limit of the faulting is about 10 km beyond the location of the third subevent, or about 20 km NW of the Sele valley. As will be seen later, this position corresponds to the NW limit of intense aftershock activity, though some aftershocks occurred beyond it. This suggests that motion in the second and third subevents occurred on a normal fault parallel to the escarpment forming the NE edge of the Monti Picentini range (Plate 1 and Fig. 10a). Long-period waveform modelling suggests that a moment of about  $10^{19}$  Nm was released in faulting along this segment; more than was released on the segment to the E of the Sele Valley. In 1984 we searched for a continuation of the surface faulting to the W of the Sele Valley, but because of the inaccessibility of this area and the dense coverage of vegetation, our search was inconclusive. However, the escarpment west of Caposele (Plate 1) does resemble topographically the fault escarpment N of Monte Valva, on which the NW end of the Monte Marzano segment of surface faulting was found (Fig. 1).

This concludes a summary of our results concerning the first three subevents of the mainshock. However, it is clear from Fig. 9 that there are complexities in the later parts of the waveforms that are not accounted for by these subevents. These later features in the waveforms are investigated in the next three sections.

## 7 Overall moment tensor of the mainshock from inversion of long-period waveforms

In this section overall moment tensors for the mainshock, determined using a variety of procedures, are compared and used to investigate the size and orientation of the seismic moment not already accounted for by the long-period waveform modelling in Section 5.

Boschi *et al.* (1981) determined a moment tensor (tensor A in Table 4) using the centroid-moment tensor inversion technique of Dziewonski, Chou & Woodhouse (1981) with body wave (at 45–60 s periods) and mantle wave (at 135–180 s periods) data from 24 stations of the Global Digital Seismograph Network (GDSN). These consisted of 12 SRO (Seismological Research Observatory), or ASRO (Abbreviated SRO), 1 DWSSN (Digital WWSSN) and 11 IDA (International Deployment of Accelerometers) stations. Their solution for the centroid time was 17 s after the nominal origin time, suggesting that the earthquake had much longer duration source time–function than the 11 s accounted for by the waveform modelling in Section 5. Their location of the centroid is at 40.73°N, 14.97°E, which is 40 km SW of our mainshock epicentre. The offset of this centroid from the hypocentre calculated from *P*-wave arrival times is due to the finiteness of the source and to lateral variations in velocity structure on a global scale (Dziewonski *et al.* 1981). The major double couple (defined in the caption for Table 4) of the solution (number 1 in Fig. 11a) corres-

**Table 4.** Moment tensors *A* to *H*, discussed in the text.  $M_i$  ( $i = 1$  to 3) is the  $i$ th eigenvalue; the orientation of the corresponding eigenvector is indicated by its plunge, *P*, and plunge azimuth, *A*, both in degrees. Moment tensor elements are indicated in the designated co-ordinate system, together with their fractional standard errors, where determined. The centroid parameters listed are latitude and longitude, in degrees; depth, *H*, in km; scalar moment,  $M_0$ , in  $10^{18}$  Nm; mean square mismatch, *R*, between the observed and synthetic seismograms used in each solution; assumed source duration,  $T_A$ , and centroid time relative to origin time,  $T_C$ , both in seconds; strike,  $\phi$ , dip,  $\delta$ , and rake,  $\lambda$ , of major double couple, in degrees, using the convention of Aki & Richards (1980). Except for the centroid depth for tensor *E*, in all cases shown the centroid latitude, longitude, depth and time have been determined in the inversion, and were not constrained *a priori*. Tensor *H* is the major double couple of tensor *G*. All the moment tensors listed here have been constrained to have zero isotropic component.

Eigenvectors				Moment Tensor						Centroid Parameters				
<i>i</i>	$M_i$	<i>P</i>	<i>A</i>	(	$M_{ZZ}$	$M_{ZS}$	$M_{ZE}$	)		Lat.	Lon.	<i>H</i>		
				(	$M_{SZ}$	$M_{SS}$	$M_{SE}$	)	$M_0$	$\phi$	$\delta$	$\lambda$	$T_A$	$T_C$
A (1)	25.0	13	062	(	-30.6	9.7	-9.3	)	40.73	14.97	25.			
	(2)	9.0	6 331	(	9.7	10.8	-5.1	)	29.5			20.	17.	
	(3)	-34.	76 218	(	-9.3	-5.1	20.0	)	332.	57.	-80.			
B (1)	27.7	0	037	(	-28.0 11%	0. FIXED	0. FIXED	)	40.92	15.37	10.			
	(2)	3.5	0 127	(	0. FIXED	17.1 21%	-14.0 21%	)	28.0			10.		
	(3)	-28.0	90	(	0. FIXED	-14.0 21%	10.9 34%	)	309.	45.	-90.			
C (1)	25.8	11	036	(	-26.0 0.9%	10.6 9.0%	-3.1 26%	)	40.93	15.27	13.6			
	(2)	2.7	7 305	(	10.6 9.0%	15.5 1.2%	-10.5 1.2%	)	27.2	.304	30.	17.1		
	(3)	-28.5	76 184	(	-3.1 26%	-10.5 1.2%	10.5 1.6%	)	300.	57.	-98.			
D (1)	24.8	8	039	(	-25.8 1.5%	4.5 17%	-6.1 13%	)	40.90	15.29	14.			
	(2)	2.2	4 130	(	4.5 17%	15.3 1.2%	-10.6 1.2%	)	25.9	.306	30.	16.		
	(3)	-27.0	81 243	(	-6.1 13%	-10.6 1.2%	10.6 1.2%	)	313.	53.	-86.			
E (1)	25.2	16	051	(	-21.4 2.6%	3.1 64%	-15.0 14%	)	40.92	15.37	12.			
	(2)	2.1	15 145	(	3.1 64%	10.7 4.7%	-10.8 8.0%	)	26.3	.292	30.	11.3		
	(3)	-27.3	68 275	(	-15.0 14%	-10.8 8.0%	10.7 5.4%	)	333.	63.	-74.			
F (1)	20.0	14	043	(	-17.5	5.9	-7.4	)						
	(2)	0.0	4 134	(	5.9	9.8	-8.8	)	20.0					
	(3)	-20.0	75 241	(	-7.4	-8.8	7.7	)	317.	59.	-85.			
G (1)	6.7	7	208	(	-8.3 4.7%	-1.4 59%	1.3 52%	)						
	(2)	2.0	3 298	(	-1.4 59%	5.5 3.2%	-1.8 7.5%	)						
	(3)	-8.7	82 049	(	1.3 52%	-1.8 7.5%	2.9 5.1%	)						
H (1)	6.7	7	208	(	-6.5 6.0%	-1.3 64%	1.1 61%	)						
	(2)	0.0	3 298	(	-1.3 64%	5.1 3.5%	-2.7 5.0%	)	6.7					
	(3)	-6.7	82 049	(	1.1 61%	-2.7 5.0%	1.4 11%	)	284.	34.	-100.			

ponds to a focal mechanism similar to that determined from *P*-wave first-motion polarities. The non-zero middle eigenvalue indicates a substantial non-double-couple component in the overall moment tensor.

Kanamori & Given (1982) determined a moment tensor by inverting very long-period (around 250 s) Rayleigh waves recorded at IDA stations. However, because the focal depth is small compared with the wavelength and vertical extent of these Rayleigh waves, this inversion technique cannot resolve the  $M_{ZS}$  and  $M_{ZE}$  moment tensor elements (tensor B in Table 4; number 2 in Fig. 11a). Consequently, Kanamori & Given constrained these elements to be zero. This is equivalent to constraining one of the three eigenvectors of the moment

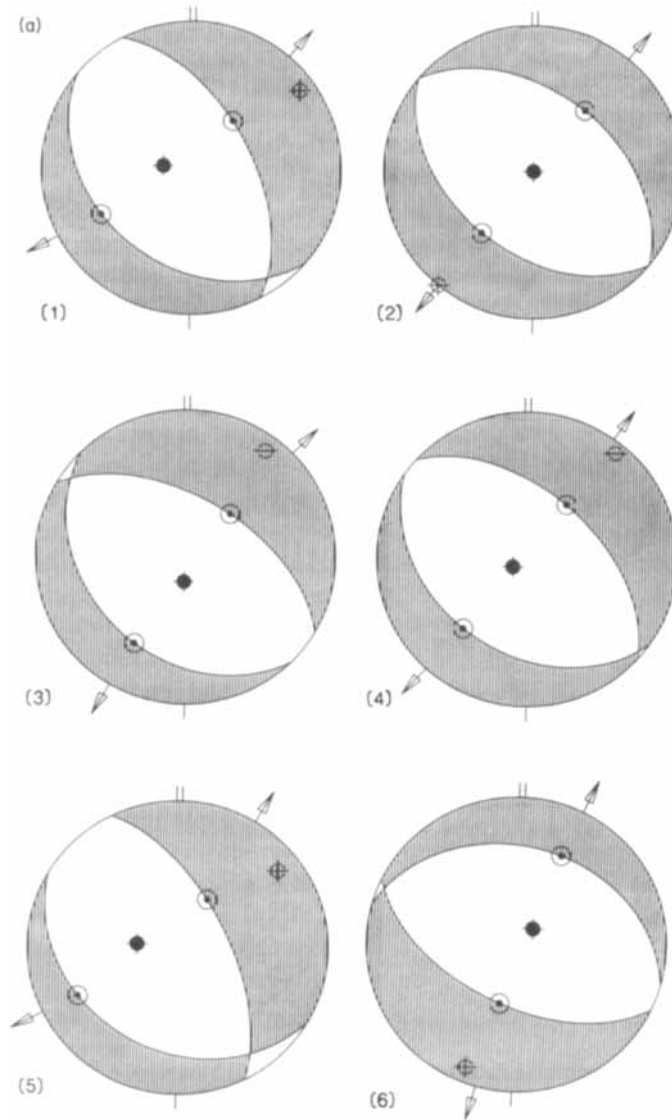


**Figure 11.** (a) Lower hemisphere equal area projections showing the major double couples for the following six moment tensors: (1) tensor A from Boschi *et al.* (1981); (2) tensor B from Kanamori & Given (1982); and (3) tensor C; (4) tensor D; (5) tensor E; (6) tensor G, all determined in this study. The orientations of the largest and smallest eigenvectors of each tensor are indicated by crosses inside open and filled circles. The tensors are described fully in Table 4. The major double couple,  $Y$ , of a moment tensor,  $X$ , is a tensor with the same eigenvectors as  $X$ , but with eigenvalues modified as follows: the middle eigenvalue of  $Y$  is set to zero; the middle eigenvalue of  $X$  is subtracted from the eigenvalue of  $X$  furthest from zero, giving, depending on its sign, the largest or smallest eigenvalue of  $Y$ ; the remaining eigenvalue of  $Y$  is equal to the remaining eigenvalue of  $X$ . (b) Waveforms from the inversion for moment tensor D of Table 4. Examples are shown to indicate the match between observed (upper) and synthetic (lower) seismograms. The 23 GDSN stations from which records were used were MAJO, TATO, CTAO, CHTO, KAAO, ANTO, SNZO, GUMO, NWAQ, BCAA, ZOBO, ANMO, GRFO, KONO (SRO and ASRO), LON (DWSSN), KMY, GUA, GAR, TWO, SUR, BDF, NNA and ESK (IDA). (i) Body wave records from SRO stations MAJO, GUMO, TATO, CTAO, CHTO, KAAO, ANTO, SNZO, NWAQ and BCAA (vertical components only), and from WWSSN stations BUL and POO. (ii) Mantle wave records from MAJO, GUMO, TATO, CTAO, CHTO, KAAO, ANTO, SNZO, NWAQ and BCAA.





tensor to be vertical and the other two to be horizontal. Because, in this case, the null axis has been determined to be horizontal, this constraint makes the dip of both nodal planes  $45^\circ$ .

In order to check the degree of constraint of the moment tensor of Boschi *et al.* (1981), we incorporated additional long-period body-wave data from 11 WWSSN stations (KEV, QUE, POO, KOD, AAE, BUL, WIN, LON, JCT, AKU and GDH) into the inversion procedure. Records were digitized, deskewed, baseline-corrected and resampled at 1 s intervals, the resampling being synchronized with the minute markers. The records were Fourier transformed and the WWSSN instrumental response (described after Hagiwara 1958) was removed by spectral division. The spectra were then multiplied by the frequency response of a 'typical' SRO instrument, that was also used to normalize amplitude and phase responses of the different SRO instruments, and low-pass filtered with a cosine-squared roll-off between 45 and 60 s period. After being transformed back into the time domain, these records were merged into this inversion procedure as equivalent to SRO records, together with digital data from 23 GDSN stations.

First, the GDSN data were used on their own to determine a moment tensor, repeating the work of Boschi *et al.* (1981), but with the laterally varying earth model used by Dziewonski, Franzen & Woodhouse (1985) instead of the spherically symmetrical earth model used by Boschi *et al.* The tensor obtained (tensor C in Table 4; number 3 in Fig. 11a) is similar to that determined by Boschi *et al.* (tensor A in Table 4), the main difference being that use of the more accurate velocity model has moved the centroid much closer to our preferred epicentre calculated from *P*-wave arrival times. Synthetic waveforms were calculated for the digitized WWSSN stations, though records from these stations were not used to constrain this inversion. Many features in the observed WWSSN waveforms were reproduced in the synthetic waveforms. This suggested that the digitized WWSSN records contain enough information at long periods to help further constrain the moment tensor.

Consequently, we attempted a second inversion, combining the filtered digitized WWSSN records and the GDSN data. The moment tensor we determined (tensor D in Table 4; number 4 in Fig. 11a) represents an improvement over tensors A and C in that the standard errors of elements  $M_{ZS}$  and  $M_{ZE}$  are reduced. Representative observed and synthetic seismograms for this inversion are shown in Fig. 11(b).

Finally, an inversion was carried out using only the digitized WWSSN records (tensor E in Table 4; number 5 in Fig. 11a). The centroid remained close to our preferred epicentre, the match between observed and synthetic filtered WWSSN seismograms was similar to that in Fig. 11(b), and the moment tensor remained similar to tensors A, C and D. However, the number of stations and the quality of the data are, in this case, insufficient to constrain elements  $M_{ZS}$  and  $M_{ZE}$  well.

Thus, the solution for the overall moment tensor is very similar regardless of the set of data used to determine it, though it is less well constrained when only digitized WWSSN data or very long period IDA data are used. In all the cases presented here the tensor has a scalar moment close to  $26 \times 10^{18}$  Nm, a non-double-couple component of the order of 10 per cent of the total moment, a maximum eigenvalue with eigenvector (the *T*-axis) plunging steeply SW, a middle eigenvalue with eigenvector (the null axis) subhorizontal and plunging at a shallow angle NW or SE, and a minimum eigenvalue with eigenvector (the *P*-axis) also subhorizontal but plunging at a shallow angle NE or SW. The moment tensor is stable with respect to changes in the set of data used to determine it, and can be used to provide an overall constraint on the size and orientation of moment release in the mainshock. The major double couple for each moment tensor has a similar orientation to the focal mechanism determined from first motion polarities (Fig. 4), suggesting that a large

proportion of the moment release occurred on faults parallel to those that moved in the early ruptures.

An important result of this investigation is that a satisfactory, though less well constrained, moment tensor, could be determined from filtered, digitized, records at 11 WWSSN stations, indicating that WWSSN records of an earthquake of this size contain sufficient information at long periods (45–60 s) to enable this to be done. Use of this technique can thus enable moment tensors to be determined for large earthquakes that occurred before GDSN stations were deployed.

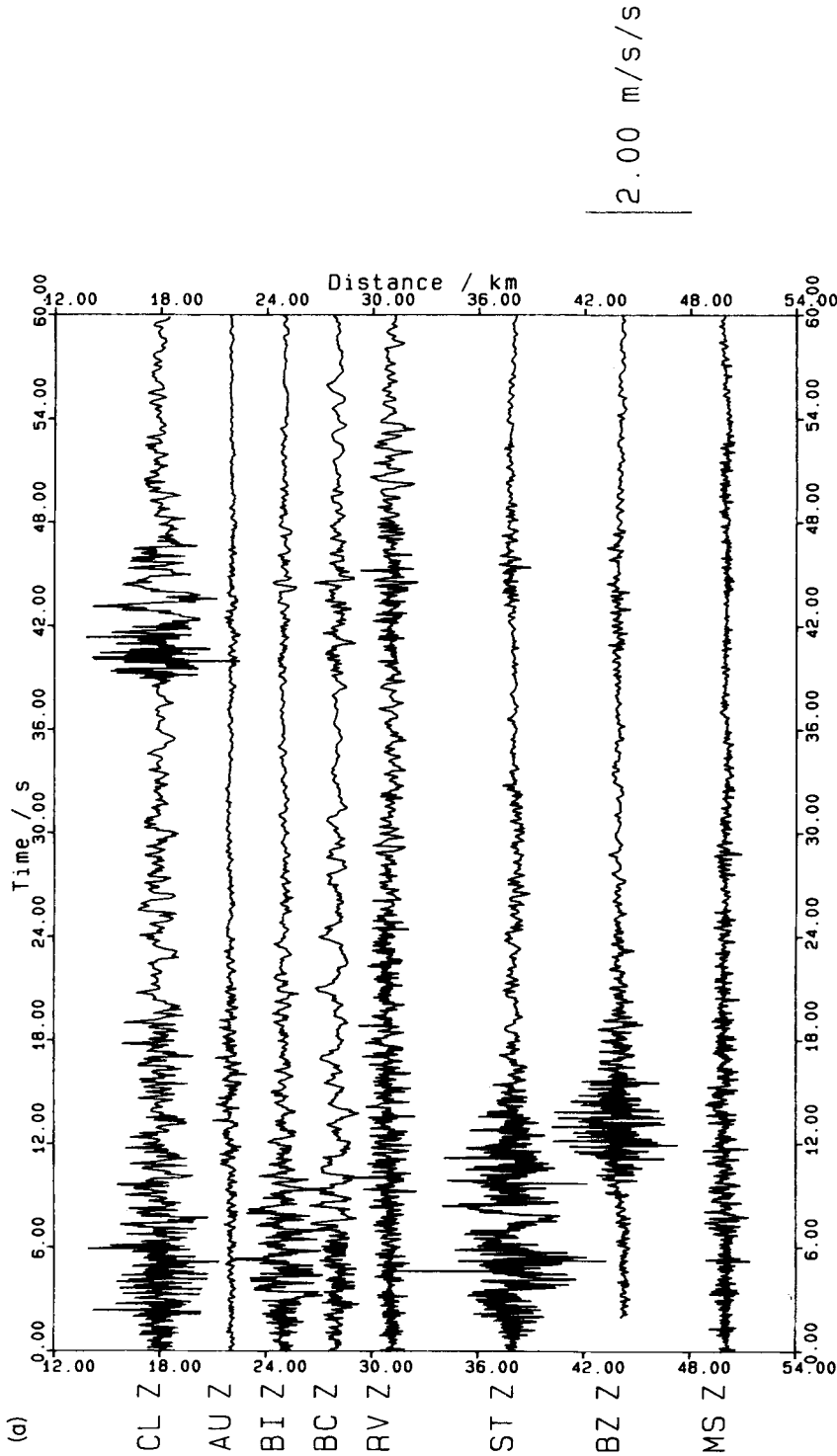
Like many other earthquakes (Dziewonski *et al.* 1981), this event has a moment tensor with a substantial non-double-couple component. Attempts have been made to explain the non-double-couple component of such moment tensors in terms of a compensated linear vector dipole term, caused by processes not involving shear motion on a fault (e.g. Knopoff & Randall 1970; Julian 1983). This type of source behaviour will not be considered here. A second possibility is that a non-double-couple component can arise because the inversion procedure to determine the moment tensor is poorly constrained, either because of poor azimuthal coverage of stations or because of use of an inappropriate velocity model (e.g. Johnston & Langston 1984). However, the testing discussed above has established that the preferred moment tensor, tensor D in Table 4, is well-constrained and stable with respect to changes both in the velocity model and in the set of waveform data used to determine it. A third possibility, which we pursue later, is that the non-double-couple component arises from the superposition of two or more double couple mechanisms with different orientations (e.g. Berberian *et al.* 1984; Eyidogan & Jackson 1985). At this point, it is important to note that the total scalar moment of tensor D,  $26 \times 10^{18}$  Nm, is roughly double the moment accounted for by waveform modelling in Section 5 of the three early ruptures.

## 8 Short-period ground acceleration in the mainshock

The mainshock of 1980 November 23 triggered 21 analogue accelerograph stations that form part of a network operated by the Italian Electricity Board (ENEL) and Nuclear Energy Authority (ENEA). Eight of these stations (Table 5) were within 50 km of the mainshock hypocentre, and are used here to investigate the geometry of faulting of the mainshock in more detail than was possible from long-period teleseismic recordings alone. All of the instruments whose records are used here were sited so as to record true ground acceleration,

**Table 5.** Positions of the eight accelerograph stations for which data are used in this study. From Berardi, Berenzi & Capozza (1981), with corrections by Westaway (1985). Each station comprised a three-component set of Kinometrics SMA-1 instruments (Berardi *et al.* 1981), designed to be triggered by ground acceleration in excess of  $0.1 \text{ ms}^{-2}$  and to record subsequent ground acceleration on 70 mm photographic film, the film running at  $10 \text{ mm s}^{-1}$ .

	Latitude	Longitude	Site	Name
AU	40 33.62 N	15 23.50 E	stiff	Auletta
BC	41 00.78 N	15 22.55 E	stiff	Bisaccia
BI	40 49.25 N	15 04.17 E	rock	Bagnoli Irpino
BZ	40 28.45 N	15 38.10 E	soft	Brienza
CL	40 55.02 N	15 26.32 E	rock	Calitri
MS	40 47.48 N	14 45.85 E	soft	Mercato San Severino
RV	40 55.77 N	15 40.17 E	soft	Rionero in Vulture
ST	41 01.35 N	15 07.03 E	rock	Sturno



CAMPANIA-BASILICATA 23 NOVEMBER 1980 MS=6.9

**Figure 12.** (a) Vertical component records from the 8 accelerograph stations within 50 km of our preferred mainshock hypocentre, plotted against approximate hypocentral distance. Note that after the early signal dies out, further signals are visible at about 40 s after trigger time. (b) Peak horizontal ground acceleration in the first 10 s after trigger time, for the six closest accelerograph stations. Acceleration has been normalised empirically (see Table 6), for a source distance of 20 km, and is plotted against azimuth about our preferred mainshock hypocentre.

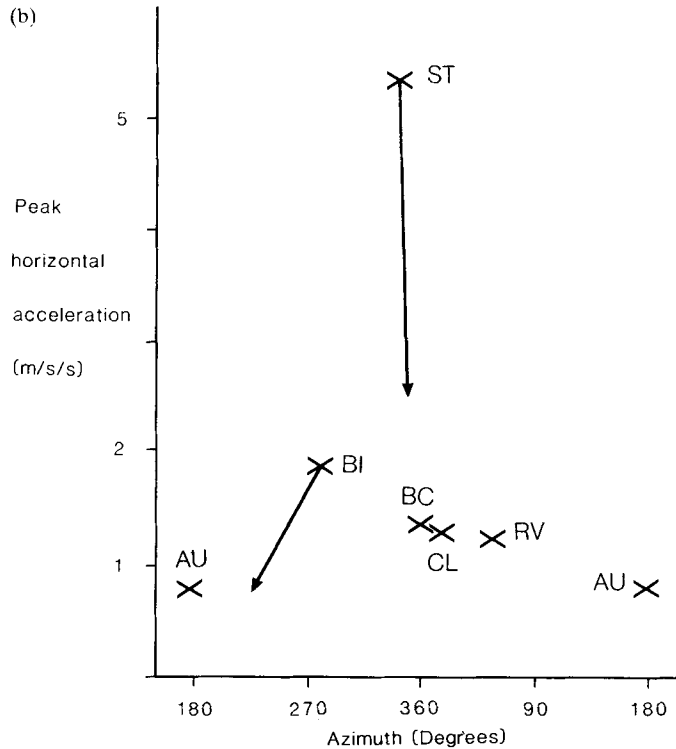


Figure 12—continued

unmodified by any man-made structures. Instruments at rock sites were anchored directly on to the rock, and those on unconsolidated material were attached to concrete piles to ensure good coupling with the ground. The instruments had, typically, natural frequencies around 26 Hz, with sensitivity around  $2 \text{ mm ms}^{-2}$  (meaning that a ground acceleration of  $1 \text{ ms}^{-2}$  will generate a record 2 mm in amplitude) and damping about 0.6 of critical. This form of instrumental response enables frequencies below the natural frequency of the instrument to be recorded with roughly equal sensitivity, and with a roughly constant phase relationship between the record and the ground acceleration, making correction for the instrumental response unnecessary. The records were digitized by ENEA at Rome, using a laser scanner, and supplied on magnetic tape, ground acceleration being sampled every 0.0029 s. Absolute timing was not recorded.

Fig. 12(a) shows the vertical component of ground acceleration at the stations within 50 km of the mainshock hypocentre. A more complete set of records is displayed in Berardi *et al.* (1981). After the ground acceleration first dies out, further strong signals are visible about 40 s after trigger time at most stations. This suggests that after the early ruptures died out, further faulting took place approximately 40 s after the origin time of the mainshock.

We now examine the variations in peak horizontal ground acceleration recorded at the closest accelerograph stations. Because these stations lie at different distances from the earthquake source, we need to correct for distance before investigating the dependence of peak acceleration on other source properties. Many people have derived empirical scaling laws that predict ground acceleration around earthquake sources (see Campbell 1985, for a review of this subject). We base our correction for distance on the principle used in the

scaling law of Joyner & Boore (1981). They suggest that within about 40 km of a source, variations with distance of peak horizontal ground acceleration are caused mainly by geometrical spreading, rather than crustal anelasticity, leading to the  $1/r$  factor in their scaling law; a feature which we consider to be physically sensible. The distance parameter  $r$  used by Joyner & Boore is defined as

$$r = (d^2 + k^2)^{1/2},$$

where  $d$  is the distance from the station to the closest point on the surface projection of the fault rupture and  $k$  is a constant equal to 7.3 km. Fig. 12(b) shows peak horizontal ground acceleration at the six closest stations, corrected for distance and plotted against azimuth about our preferred first-motion hypocentre. For stations AU, BC, CL and RV, we have measured  $d$  from the epicentre above this hypocentre. In Section 5 we demonstrated that the fault rupture propagated predominantly northwestward from this hypocentre. Consequently, for stations to the NW of this epicentre (BI and ST) we indicate a range of normalized peak horizontal acceleration, corresponding to measuring  $d$  either from this epicentre, or from the closest point to each station on the Monti Picentini segment of faulting. The second of these alternatives is required if the actual Joyner & Boore scaling law is to be used. However, because the peak accelerations at ST and BI occurred only 5 and 4 s after trigger time, respectively, we consider it likely that they were produced by fault ruptures that occurred within a few kilometres of our first motion hypocentre, and hence we prefer the first alternative. Regardless of the distance correction used, peak horizontal acceleration varies systematically with azimuth (Fig. 12b), the strongest normalized acceleration being recorded at ST, at an azimuth of  $324^\circ$ , close to the strike of the fault plane ( $317^\circ$ ). In the near-field, the strongest high-frequency signal should be radiated in the direction towards which the source rupture propagates (e.g. Madariaga 1983). Thus, the high peak ground acceleration observed to the NW is consistent with the interpretation that the predominant direction of rupture propagation was NW, as deduced in Section 5 from teleseismic waveform modelling. Rupture propagation has a much greater effect than local site conditions in determining the strength of ground acceleration at each station (Table 6).

The azimuthal dependence of peak ground acceleration in the 40 s subevent can be used to investigate the orientation of this source. Key & Crosson (1984) and Crosson *et al.* (1986) have already attempted to do this. They noticed that if the 40 s subevent is assumed to have nucleated at  $40.81^\circ\text{N}$ ,  $15.25^\circ\text{E}$ , close to Caposele at the northern end of the Sele valley (Fig. 3), then the peak horizontal ground acceleration has an azimuthal dependence different from that in Fig. 12(b), with the largest peak accelerations being the NE. This is taken to indicate that the source of the 40 s signals involved a rupture propagating NE along strike of a normal fault downthrown to the SE. As will be seen, we believe the epicentre of this subevent is about 20 km NE of that assumed by Crosson *et al.* and Key & Crosson. We also show that rupture on a NE-striking normal fault does not provide a satisfactory match to most observed long-period waveforms or to the overall moment tensor.

Another feature of the strong ground motion records in Fig. 12(a) is that the peak ground acceleration at stations AU and BZ, SE of the epicentre of the first subevent, occurs between 10 and 15 s after trigger time. In contrast, peak acceleration at other stations, including those further from the hypocentre of the first subevent, occurs well before 10 s after trigger time. If the largest-amplitude ground acceleration is due to  $S$ -waves, and realistic average  $S$ -wave velocities around  $3 \text{ km s}^{-1}$  are assumed for the paths to the SE stations, then the strongest signals at AU and BZ are several seconds too late to be explained as the  $S$ -wave arrival from the first subevent, even if it is assumed that the instruments triggered at the  $P$ -wave arrival time. This suggests that the signals arriving at 10–15 s at AU and BZ were

**Table 6.** Peak horizontal ground acceleration,  $a_r$ , in the first 10 s after trigger time, at the six closest accelerograph stations, against station azimuth  $\theta$  about our preferred first subevent hypocentre. Observed ground accelerations have been scaled to correct distance using the following empirical rule derived from the results of Joyner & Boore (1981):  $a_{20} = a_r \cdot (r/20) \cdot 10^{-0.00255(20-r)}$ . The final column lists  $a_{20}$ , the peak horizontal acceleration scaled to a distance,  $r$ , of 20 km. The two Joyner & Boore distance parameters,  $d$  and  $r$ , are defined in the text. At all stations, we use the distance from each station to the epicentre of the first subevent as an estimate for  $d$ . In the bottom two rows, peak horizontal acceleration at BI and ST is scaled instead using the distance to the closest point on the Monti Picentini segment of faulting, rather than the distance to this epicentre. Site conditions are from Berardi *et al.* (1981).

Code	$d$ /km	$r$ /km	$\theta$	$a_r$ /ms <sup>-2</sup>	$a_{20}/a_r$	$a_{20}$ /ms <sup>-2</sup>	Site
AU	25	26	178	0.63	1.35	0.85	Stiff
BC	26	27	358	0.95	1.41	1.34	Stiff
BI	23	24	285	1.54	1.23	1.89	Rock
CL	17	19	015	1.36	0.94	1.28	Rock
RV	32	33	059	0.71	1.78	1.26	Soft
ST	32	33	324	3.00	1.78	5.34	Rock
BI	6	10	225	1.54	0.47	0.73	
ST	15	17	348	3.00	0.84	2.51	

radiated by an additional source that has not yet been accounted for. We investigate these signals in more detail later in this section.

In the remainder of this section, we use short-period records of ground acceleration to study three separate features of the mainshock. First, we attempt to locate the source of the 40 s signals. We do this in three independent ways: by identifying *S*- and *P*-wave arrivals and using the *S*–*P* interval to obtain the distance between the hypocentre and each station; by using the interval between the *S*-wave arrivals from the first subevent and the 40 s subevent to locate the 40 s subevent relative to the first subevent; and, by using the azimuth of particle motion to infer the direction from which the *P*-wave signal from the 40 s subevent arrived at each station. Secondly, we attempt to explain the strong ground acceleration signals at stations AU and BZ 10–15 s after trigger time as due to an additional subevent of fault rupture. We suggest that these signals were produced by the fault rupture that formed the San Gregorio segment of surface faulting (Section 2). This interpretation is then tested by synthesizing long-period teleseismic waveforms incorporating this extra subevent. Thirdly, we use the azimuth of *P*-wave particle motion to infer, in more detail than was possible in Section 5, the time-history of rupture propagation in the first few seconds of the early mainshock ruptures.

### 8.1 LOCATION OF 40 S SUBEVENT

First, we locate the 40 s subevent. The *S*-wave arrival for this subevent is clear at most stations (e.g. at ST in Fig. 14e, about 42 s after trigger time). This phase can be identified as an *S*-wave because it produces greater acceleration (and velocity; see Fig. 14) on the horizontal components than on the vertical component. At several stations (e.g. at CL in Fig. 14c, around 38.5 s after trigger time), a clear phase with much smaller amplitude precedes it. This phase is strongest on the vertical component records, and is therefore identified as the

*P*-wave arrival from the 40 s subevent. Also, at most stations (e.g. at ST in Fig. 16e, around 4.5 s after trigger time), a phase that produces greater acceleration on the horizontal components than on the vertical component can be identified as arriving a few seconds after trigger time. This phase is identified as the *S*-wave arrival from the first subevent. The trigger time cannot necessarily be assumed to be the *P*-wave arrival time from the first subevent, because the *P*-wave first motion may have been insufficiently strong to trigger the instruments. However, the phases that can be reliably picked allow the 40 s subevent to be located in two ways: by using its *S*–*P* interval to find its absolute position, and by using the interval between the *S*-wave arrival times for the first and 40 s subevents to find its location relative to the first subevent.

For the location based on *S*–*P* interval (Table 7a), the hypocentral distance was calculated assuming an average *S*-wave velocity of  $3.0 \pm 0.5 \text{ km s}^{-1}$  along the ray-path, and a

**Table 7.** Location of the 40 s rupture using arrival times of seismic phases picked from records of ground acceleration: (a) Using the *P* to *S* interval; (b) Using difference in *S* wave arrival time relative to the first subevent. In Tables 7(a) and 7(b), quantities are listed followed by their estimated uncertainties. *T* denotes arrival time of seismic phases and *D* and *E* distance between stations and hypocentres or epicentres, respectively, of subevents of mainshock faulting. Superscripts denote the subevent (40 the 40 s subevent and 0 the first subevent). Subscripts indicate the type of phase, *P* or *S*. In the location using *S*–*P* interval, *T<sub>T</sub>* is the trigger time, and *T<sub>O</sub>* the origin time of each subevent considered. The origin time of the first subevent was calculated from the trigger time, calculating the hypocentral distances from the epicentral distances in Table 6, for a source 10 km deep, assuming the trigger time was the same as the *P*-wave arrival time for the first subevent, and assuming the *P*-wave velocity for this signal was  $5.25 \text{ km s}^{-1}$ . In the relative location, the value in brackets following the *S*-wave arrival time is the expected *S*–*P* interval for the first subevent, calculating the source–station distance in the same way, and assuming an *S*-wave velocity of  $3.0 \text{ km s}^{-1}$  and a *P*-wave velocity of  $5.25 \text{ km s}^{-1}$ ; *T<sub>R</sub>* and *D<sub>R</sub>* are, at each station, the difference between the observed *S*-wave interval and 38 s, and the difference in distance between the hypocentres of the first and 40 s subevents assuming this difference in *S*-wave interval. Phases were assumed to travel in straight lines between each source and station. Other assumptions are stated in the text.

(a)

Code	$T_S^{40}$ / s	$T_P^{40}$ / s	$T_S^{40} - T_P^{40}$ / s	$D^{40}$ / km	$E^{40}$ / km	$T_O^{40} - T_T$ / s	$T_O^{40} - T_O^0$ / s
BC	40.8 0.3	38.3 0.3	2.5 0.5	17.5 3.5	12.7 5.8	35.0 2.3	40.1 2.6
BI	43.4 0.2	38.5 0.2	4.9 0.4	34.3 2.8	32.1 3.6	32.0 1.9	36.5 2.2
CL	40.1 0.2	38.8 0.4	1.3 0.6	09.1 4.2	0 to 5.7	37.1 2.4	40.7 2.8
RV	44.0 0.5	40.0 0.5	4.0 0.7	28.0 4.9	25.3 4.7	34.7 2.6	40.9 3.0

(b)

Code	$T_S^{40}$ / s	$T_S^0$ / s	$T_S^{40} - T_S^0$ / s	$T_R$ / s	$D_R$ / km	$D^0$ / km	$D^{40}$ / km	$E^{40}$ / km
BC	40.8 .3	4.7 .4 (4.0)	36.1 .5	-1.9 .5	-6.6 2.7	28.0 2.	21.4 2.7	17.7 5.0
BI	43.4 .2	3.0 .2 (3.6)	40.4 .3	2.4 .3	8.4 2.3	24.8 2.	33.2 2.3	31.0 3.0
CL	40.1 .1	3.7 .4 (2.9)	36.4 .4	-1.6 .4	-5.6 2.2	20.4 2.	14.8 2.2	8.7 <13.7
ST	42.2 .3	4.0 .3 (4.9)	38.2 .4	0.2 .4	0.7 1.4	34.1 2.	34.8 1.4	32.7 .2.0

ratio of  $P$ -wave velocity to  $S$ -wave velocity of 1.75. Distance from each station to the epicentre of this subevent was calculated from the distance to the hypocentre, assuming that the 40 s subevent had a focal depth of  $12 \pm 2$  km. In Section 10, a focal depth of 12 km is shown to produce a reasonable match to the long period seismograms of the 40 s subevent. The results of this location study (Fig. 13a) suggest that the 40 s subevent had an epicentre between 10 and 20 km NNE of the first subevent. The origin time of this late subevent is calculated to be about 38 s after the origin time of the first subevent (Table 7a).

Next, the difference between  $S$ -wave arrival times for the first and 40 s subevents is used to obtain the relative locations of the two events. The difference is smallest at stations to the north of the first subevent epicentre (Table 7b), again suggesting that the 40 s subevent occurred to the north of the first subevent. In this relative location, the first subevent was assumed to be at our preferred epicentre (Section 3), and to have nucleated at a depth of 10 km. The  $S$ -wave velocity for the differential ray path was assumed to be  $3.5 \pm 0.5$  km s<sup>-1</sup>; slightly higher than the velocity used in the location from  $S$ - $P$  interval above, because this differential ray-path was at mid-crustal depths. The origin time of the 40 s subevent was taken as 38 s after the origin time of the first subevent, consistent with the  $S$ - $P$  interval (above) and with long-period waveform modelling that will be described in Section 9. The focal depth of the 40 s subevent was again assumed to be  $12 \pm 2$  km. The results of this relative location (Fig. 13b) suggest that the epicentre of the 40 s subevent was 5–15 km NE

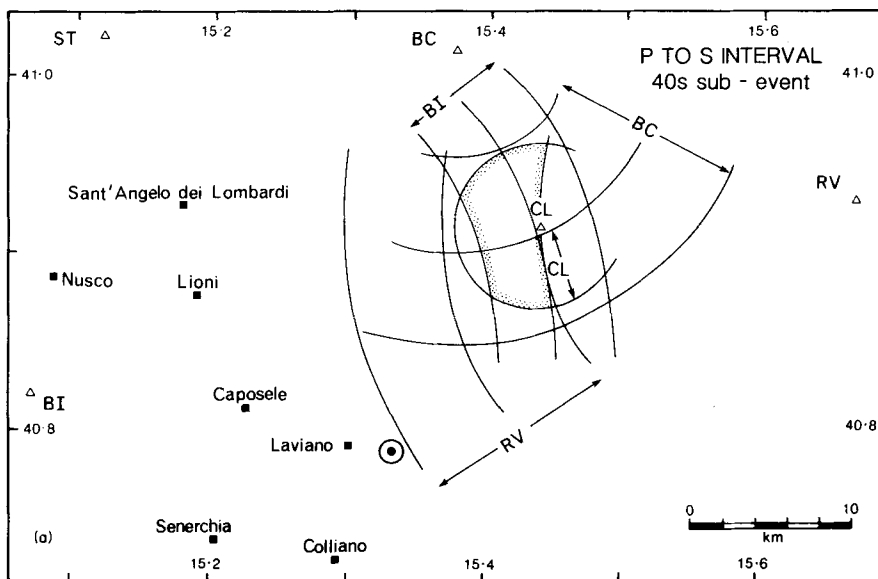


**Figure 13.** (a) Location of the 40 s subevent using  $S$ - $P$  interval. The shaded area indicates possible positions of the epicentre of this subevent, consistent with our calculated error bounds. The epicentre of the first subevent is indicated by a dot surrounded by a circle. For CL, only the outer error bound is shown, because the arrival times at this station are consistent with a hypocentre directly beneath CL. (b) Location of the 40 s subevent relative to the first subevent. The shaded area indicates possible positions of the epicentre of this subevent, consistent with our calculated error bounds. The epicentre of the first subevent is indicated by a dot surrounded by a circle. For CL, the inner error bound is not shown, because the arrival times at this station are consistent with a hypocentre directly beneath CL. (c) Location of the 40 s subevent using azimuths of  $P$ -wave particle motion. Here, an epicentre has been chosen that is consistent with the results shown in Fig. 13(a) and (b), and possible ray paths to the stations have been constructed. See text for discussion.



of the epicentre of the first subevent. Thus both the  $S$ - $P$  interval and the relative  $S$ -wave arrival times are consistent with the epicentre of the 40 s subevent being 10–15 km NNE of the epicentre of the first subevent.

Where the  $P$ -wave arrival for the 40 s subevent can be identified, the direction of  $P$ -wave particle motion can be used to infer the azimuth from which the  $P$ -wave arrived. If sufficient stations at different azimuths around the epicentre of the 40 s subevent are available, such information can be used to locate the subevent. Our technique is similar to that used by Niazi (1982), to study the Imperial Valley, California, earthquake of 1979 October 15.

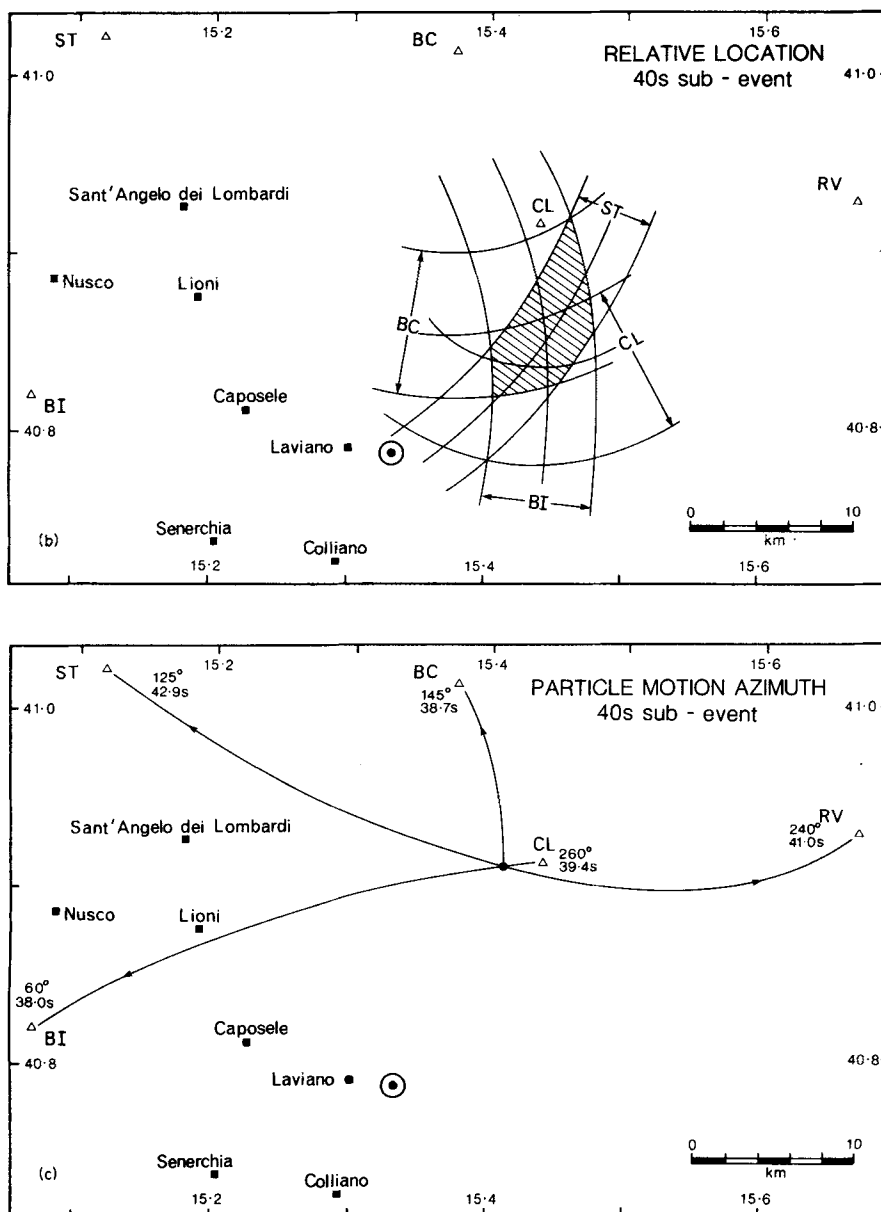


Figure 13-continued

Acceleration records were numerically integrated to give ground velocity, the integral being calculated every 0.025 s, then filtered using an eighth order band-pass Butterworth filter (Kanasewich 1981) applied in the forward direction only so as to be causal. The corner frequencies of the filter were 5 and 19 Hz, the lower value to eliminate long-period baseline errors and relatively long-period signals that are insensitive to detail in the source time-history. The horizontal component velocity records  $V_N$  and  $V_E$  were resolved parallel to different azimuths  $\theta$ , and the component of velocity at this azimuth was squared to give a quantity  $\chi$  proportional to the power in the signal:

$$\chi(\theta) = [V_N \cos(\theta) + V_E \sin(\theta)]^2.$$

The records were broken into bins of duration 0.4 s, each overlapping its neighbours by 0.2 s.  $\chi$  was summed over each bin to give  $X$ , proportional to the total energy in the signal received during the time interval covered by the bin:

$$X(\theta, T) = \sum_T^{T+0.4\text{ s}} \chi(\theta, t).$$

The function  $X$  was calculated for  $0 < \theta < 180^\circ$  in steps of  $4^\circ$ , for the first 10 s of record, and the values obtained were contoured (Fig. 14).  $X$  has a periodicity of  $180^\circ$ , making it unnecessary to calculate it for the remaining two quadrants. The chosen filter and bin duration enable variations of azimuth of the incoming signal to be resolved on a time scale of less than 1 s. The azimuth of  $P$ -wave particle motion (Fig. 13c) is consistent with the 40 s subevent epicentre being north of the first subevent epicentre. This is most strikingly demonstrated by the azimuth of the relatively strong signal from the 40 s subevent at CL. The three independent locations of the 40 s subevent, and the large amplitude of this signal all suggest that the epicentre of this subevent was close to CL, and thus the large amplitude of the signal at CL from this subevent is not an effect of rupture propagation. The particle motion directions observed at other stations are not precisely those expected for  $P$ -waves propagating through a homogeneous medium. In Fig. 13(c), ray paths have been drawn with smooth curvature, consistent with average horizontal  $P$ -wave velocity gradients of the order of  $0.1 \text{ km s}^{-1} \text{ km}^{-1}$  across the area containing the stations. Alternatively, the observed directions of  $P$ -wave particle motion could be effects of refraction across dipping interfaces separating smaller areas with different velocity structure. Lateral variations in geological structure (e.g. those shown in Fig. 3) suggest that strong lateral variations in seismic velocity are to be expected across the area containing the accelerograph stations. Consequently, it would be surprising if the  $P$ -wave signal arrived at all stations at precisely the azimuth predicted by ray theory through a uniform velocity structure.

## 8.2 ORIGIN OF THE SIGNAL 10–15 S AFTER TRIGGER TIME AT AU AND BZ

We now attempt to explain the large-amplitude ground acceleration signals that occurred 10–15 s after trigger time at stations AU and BZ, SE of the first subevent epicentre. We show that the timing of these signals and their large amplitudes at these stations are consistent with their having been caused by faulting under the Pantano di San Gregorio: where a short segment of surface faulting was found (Section 2), and where there was local intense aftershock activity (Section 10). We first use  $P$ - and  $S$ -wave arrival times to determine the distance of this source from BZ and also to determine its origin time. We then check whether these are consistent with the record at AU. Finally, we incorporate this additional subevent into synthetic long-period seismograms and compare them with those that were observed.

(a)

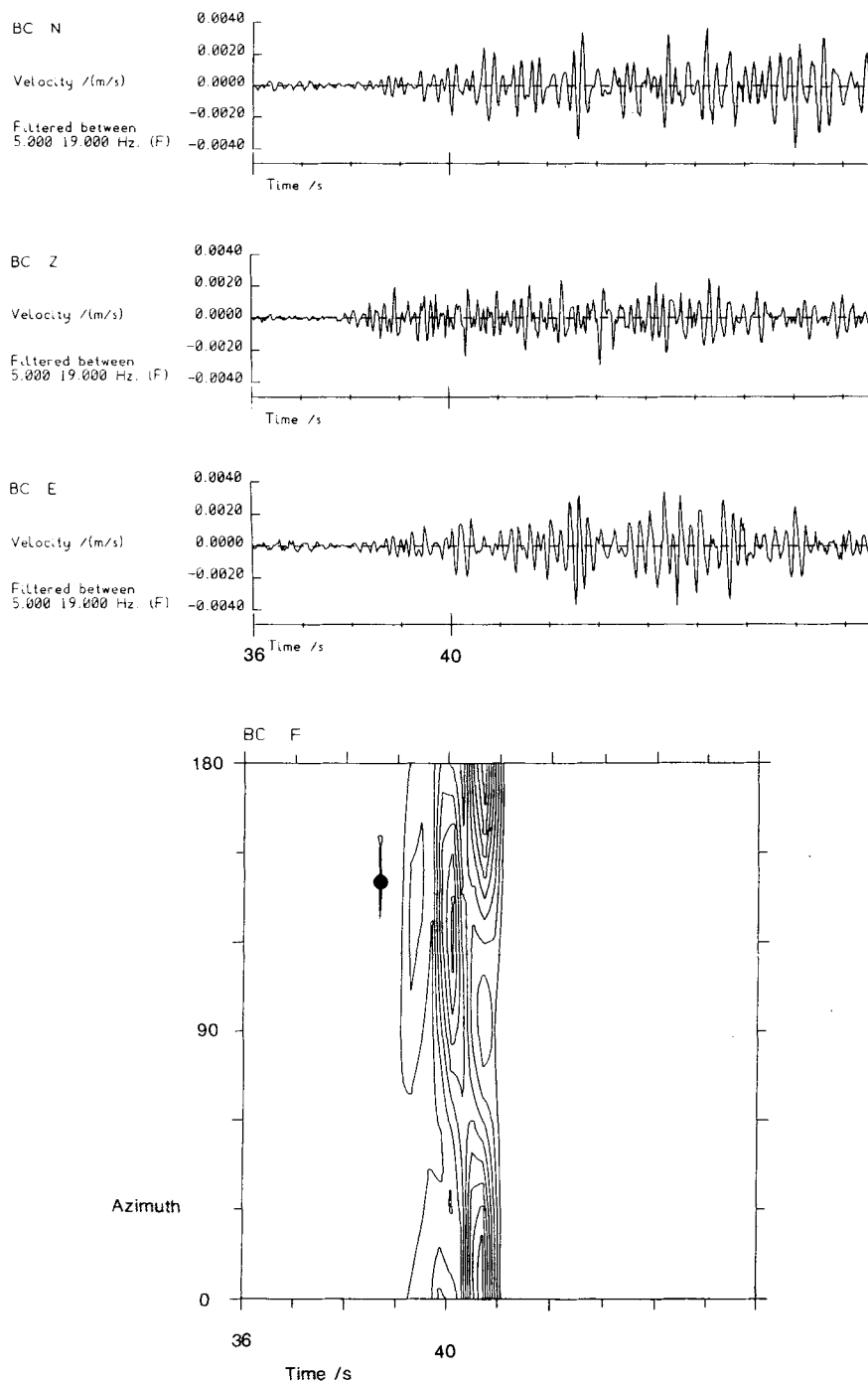


**Figure 14.** (This page and next four pages.) Filtered records of ground velocity and contours of  $X(\theta, t)$  (see text) for  $0 < \theta < 180^\circ$  and  $36 < t < 46$  s after trigger time, at stations BC (a), BI (b), CL (c), RV (d) and ST (e). The contour intervals are equal, and local maxima of  $X$ , that indicate the direction of  $P$ -wave particle motion, are marked with dots.

(b)

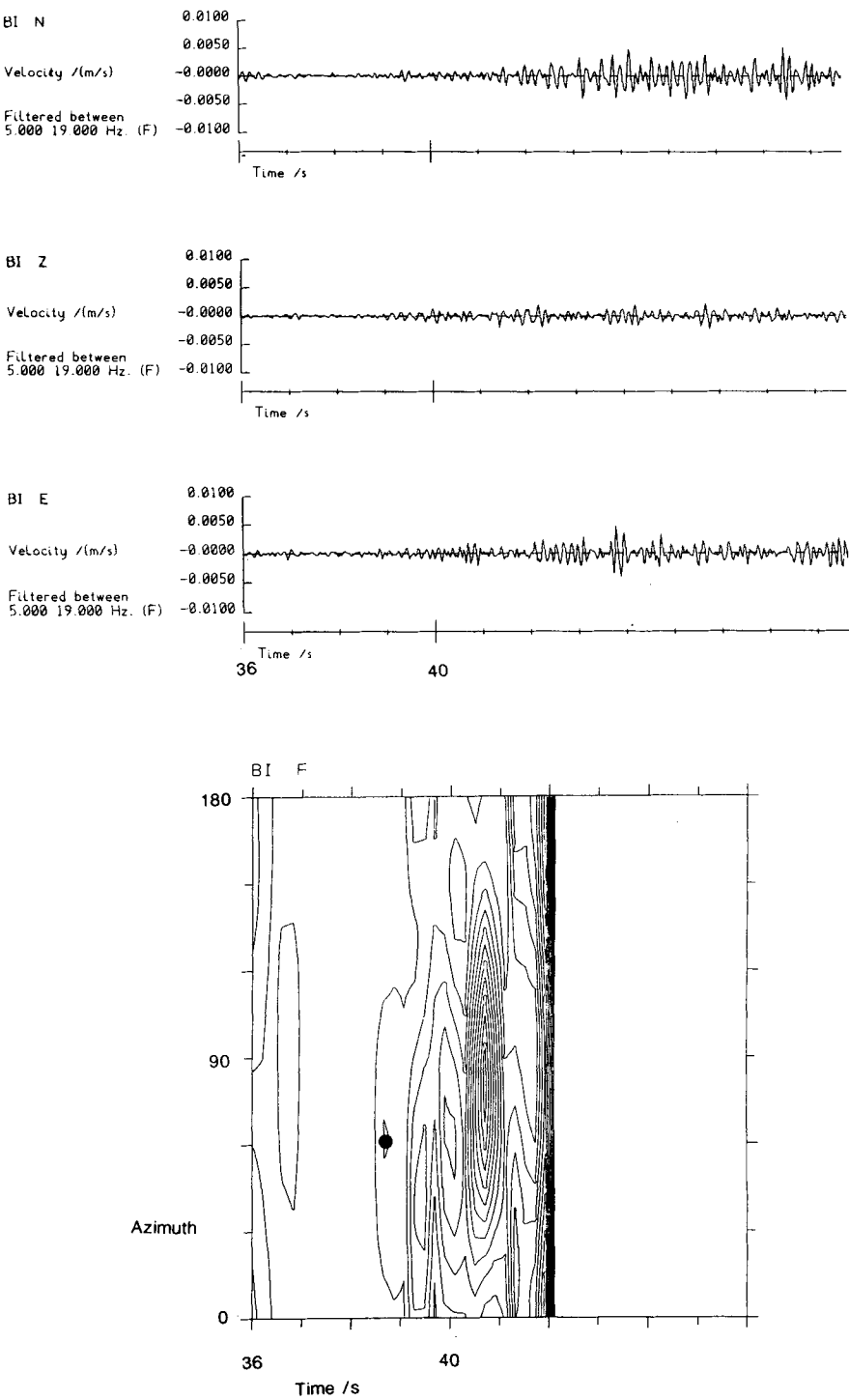


Figure 14—continued

(c)

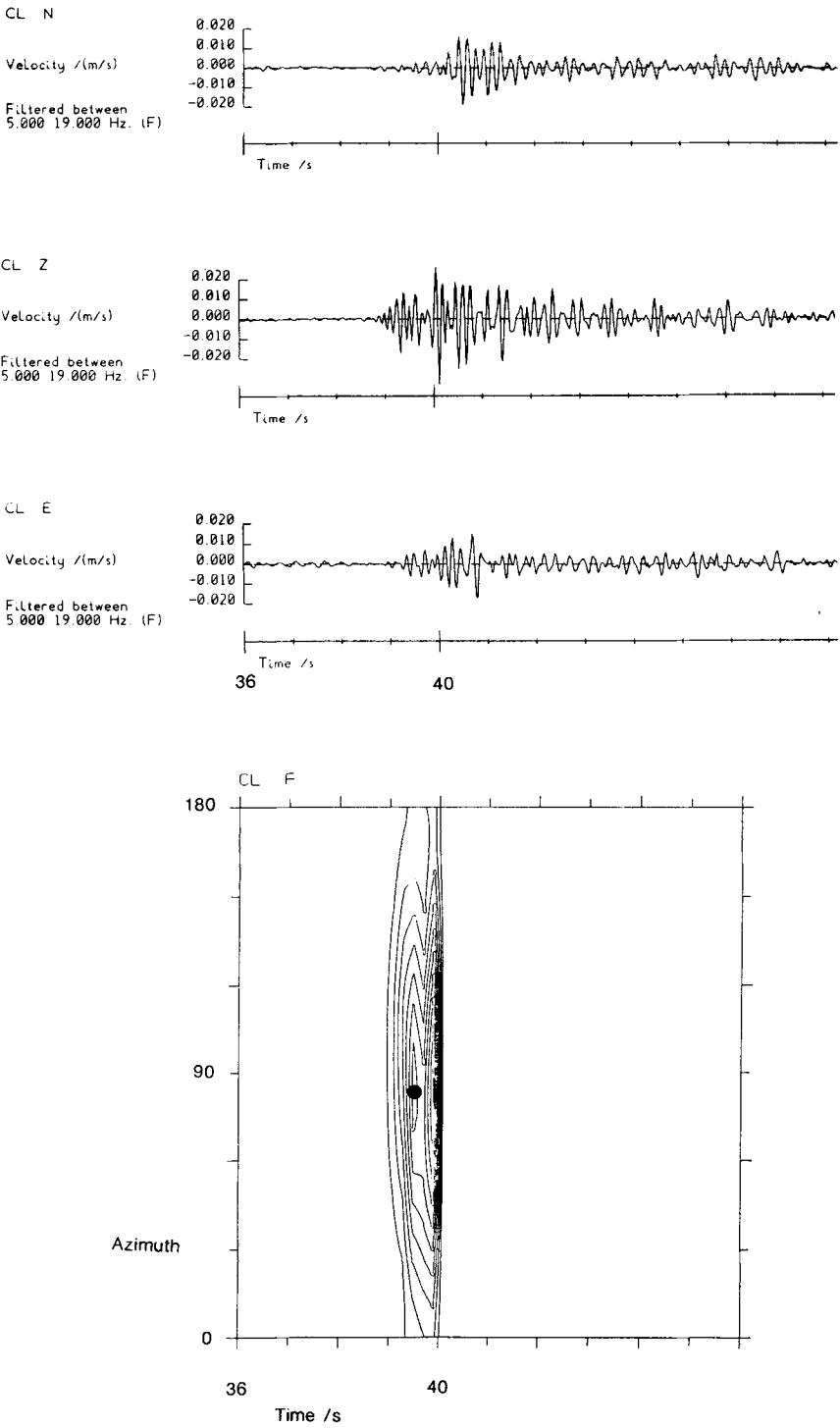


Figure 14—continued

(d)

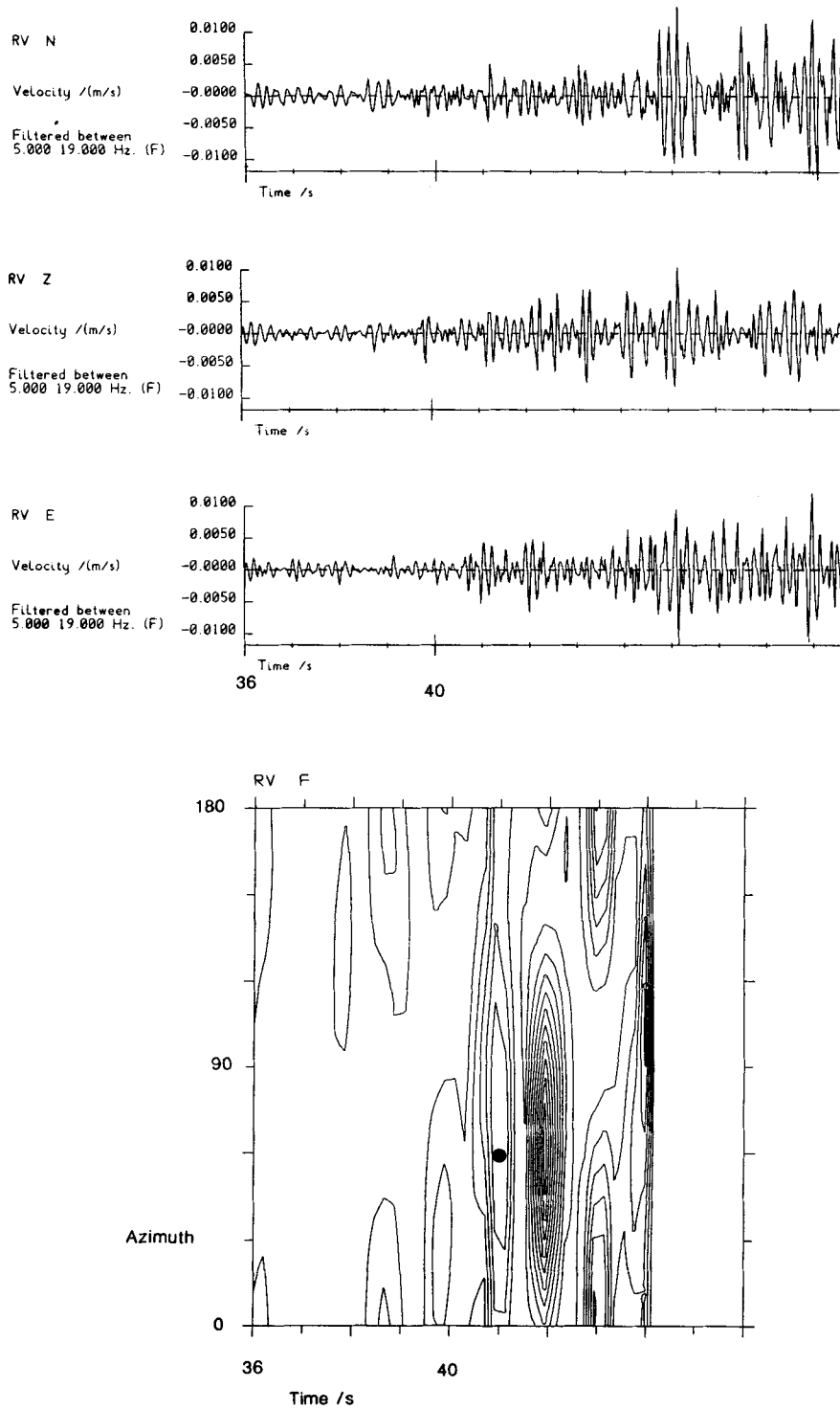


Figure 14—continued

(e)

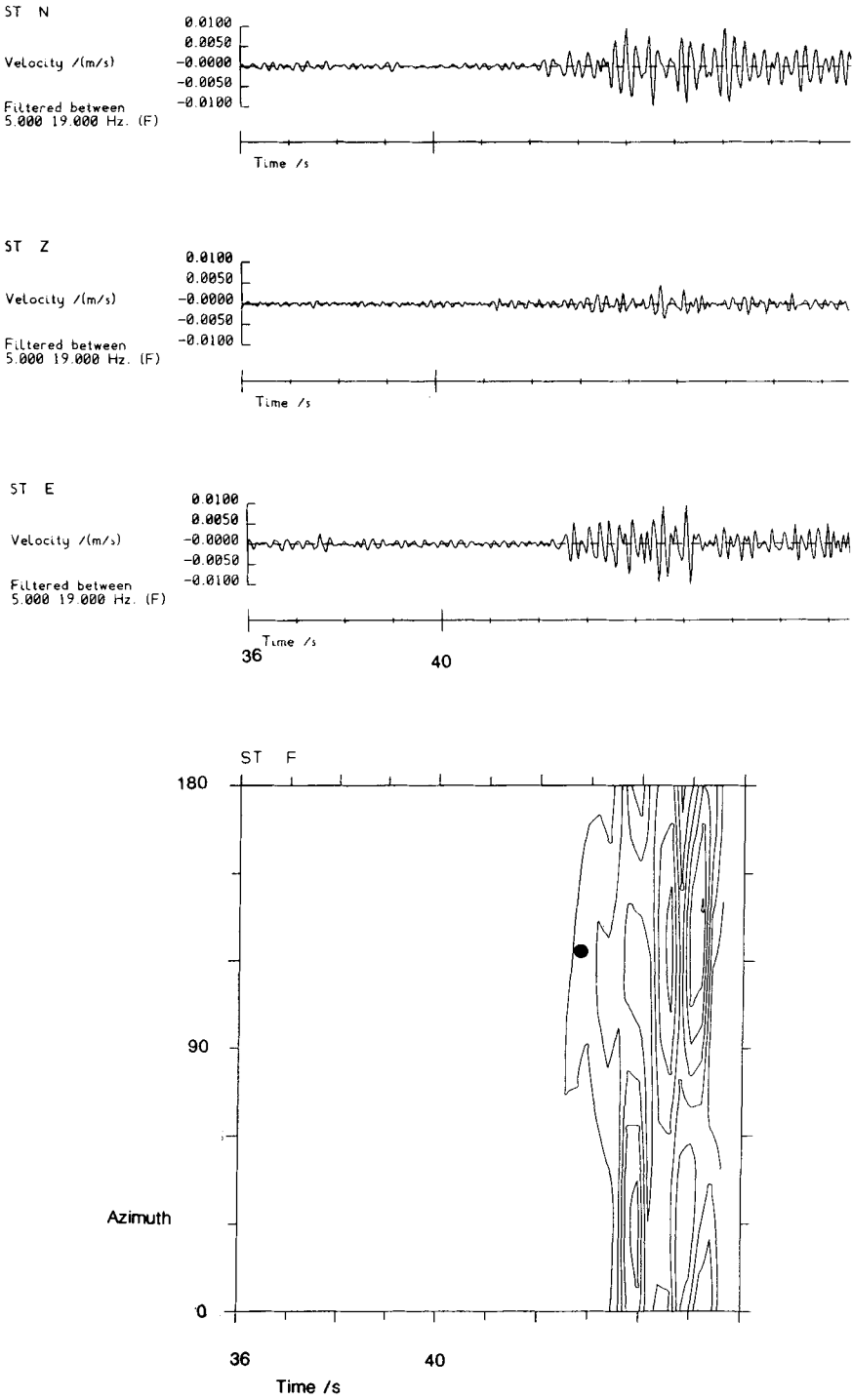


Figure 14—continued

In the following discussion of the arrival times,  $T$ , of ground acceleration signals and distances,  $D$ , between accelerograph stations and hypocentres of subevents, superscripts denote different subevents within the seismic source (0 = first subevent; 40 = 40 s subevent; \* = subevent responsible for large amplitude ground acceleration after 10 s at AU and BZ) and subscripts denote phases ( $T_P$  and  $T_S$ ), origin times ( $T_O$ ) and trigger time ( $T_T$ ).  $V_P$  and  $V_S$  are  $P$ - and  $S$ -wave velocities.

The signals from the 40 s subevent are visible several seconds earlier on the vertical component record at BZ than on the vertical component record at ST (Fig. 12a). It was shown above that the 40 s subevent is located NE of the first subevent. Because ST is NW and BZ is SE of both subevent epicentres, only small differences in relative timing of the first and 40 s subevent signals are expected when comparing records from these stations. It is unlikely that differences in velocity structure can account for this difference in relative timing. Instead, we suggest that the record at BZ was, in fact, triggered by the  $S$ -wave, not the  $P$ -wave, arrival from the first subevent. Because BZ is 42 km from the first subevent hypocentre, this implies that the instrument at BZ was triggered about 5 s later than it would have been if it had been triggered by this  $P$ -wave. Using the record shown in Fig. 12(a), we estimate the  $S$ -wave arrival time for the unaccounted-for subevent as 9.0 s after trigger time, and the  $P$ -wave arrival time as 5.5 s after trigger time.

Thus, at BZ,

$$T_P^* - T_T = 5.5 \text{ s} \quad \text{and} \quad T_S^* - T_T = 9.0 \text{ s}.$$

So,

$$D^* = V_P(T_S^* - T_P^*)/(\gamma - 1) = 28 \text{ km} \quad (1)$$

(assuming  $V_P = 6 \text{ km s}^{-1}$  and  $V_P/V_S = \gamma = 1.75$ ).

Also

$$T_P^* - T_O^* = (T_S^* - T_P^*)/(\gamma - 1) = 4.7 \text{ s}.$$

So

$$T_O^* - T_T = 0.8 \text{ s},$$

and, if the start of the record at BZ is 5 s after the  $P$ -wave arrival time, and the  $P$ -wave travel time (at  $6 \text{ km s}^{-1}$ ) to BZ (42 km distant) for the first subevent is 7 s then

$$T_T - T_O^0 = 12 \text{ s}$$

and

$$T_O^* - T_O^0 = 12.8 \text{ s}, \quad (2)$$

i.e. the origin time of the 10–15 s signal at BZ was 12.8 s after the origin time of the first subevent. Assuming a hypocentral depth of 10 km, a source at  $40.65^\circ\text{N}$ ,  $15.5^\circ\text{E}$ , close to the Pantano di San Gregorio (Fig. 3), is 28 km from BZ. Thus, such a source is consistent with the record at BZ.

This interpretation can be checked by investigating the timing of signals at AU. Station AU is 17 km from a hypocentre under the Pantano di San Gregorio and 27 km from our preferred hypocentre for the first subevent. Assuming the same average  $P$ -wave velocity as for BZ,

$$T_P^0 - T_O^0 = (27/6) \text{ s} = 4.5 \text{ s}$$



and

$$T_P^* - T_O^* = (17/6) \text{ s} = 2.8 \text{ s},$$

and

$$T_S^* - T_O^* = 4.9 \text{ s}.$$

If

$$T_O^* - T_O^0 = 12.8 \text{ s [result (2) above]},$$

then

$$T_O^* - T_P^0 = 8.3 \text{ s}$$

and

$$T_P^* - T_P^0 = 11.2 \text{ s}$$

and

$$T_S^* - T_P^0 = 13.2 \text{ s}. \quad (3)$$

Large amplitude pulses are observed at AU about 14 s after trigger time. These are consistent with the onset of the *S*-wave being a few tenths of a second earlier, and therefore consistent with the source of the large-amplitude signals observed at AU being close to the Pantano di San Gregorio, about 12.8 s after the origin time of the first subevent.

Formally, the location and timing of this San Gregorio subevent are not well constrained. They can, however, be tested by synthesizing long-period teleseismic waveforms incorporating this additional subevent. Fig. 15 shows observed and synthetic *P*- and *SH*-wave seismograms for the preferred three-source model from Section 5, including an additional source with dip  $65^\circ$ , strike  $317^\circ$ , rake  $-85^\circ$ , moment  $2.0 \times 10^{18}$  Nm, and focal depth 10 km, at the position and time suggested from the short-period study above. At the NW stations (e.g. MNT, GDH and KBS), this additional source causes an inflexion in the second upswing that matches a similar feature in the observed waveforms. At the eastern (CHG and POO) and southern (AAE and BUL) stations, the match is not as good, but the extra subevent does interfere with the second downswing from the earlier subevents and increases its amplitude so as to match that which is observed (cf. Fig. 9). This additional subevent is too small to substantially influence the form of the synthetic *SH*-waveforms.

### 8.3 DETAILED TIME-HISTORY OF THE EARLY SUBEVENTS

Finally, we use the azimuth of particle motion in the first few seconds of the *P*-wave signal to investigate the time-history of the early mainshock ruptures in more detail. The records of ground acceleration (Fig. 12a) suggest that all the instruments shown were triggered during the *P*-wave arrival from early in the source rupture, though the absence of absolute timing means that it cannot be determined whether any were triggered by the *P*-wave first motion. These records were processed (Fig. 16) in the same way as those shown in Fig. 14. The azimuth of the first *P*-wave signal (Fig. 16) is consistent at all the stations shown with the source of this signal having been close to the hypocentre determined from *P*-wave arrival times (Fig. 3), shown as source 1 in Fig. 17. This suggests that all these close instruments were, in fact, triggered by the *P*-wave first motion. However, by 0.4–1.6 s after trigger time signals appear to arrive from a source SE of the first subevent hypocentre (source 1b in Fig.

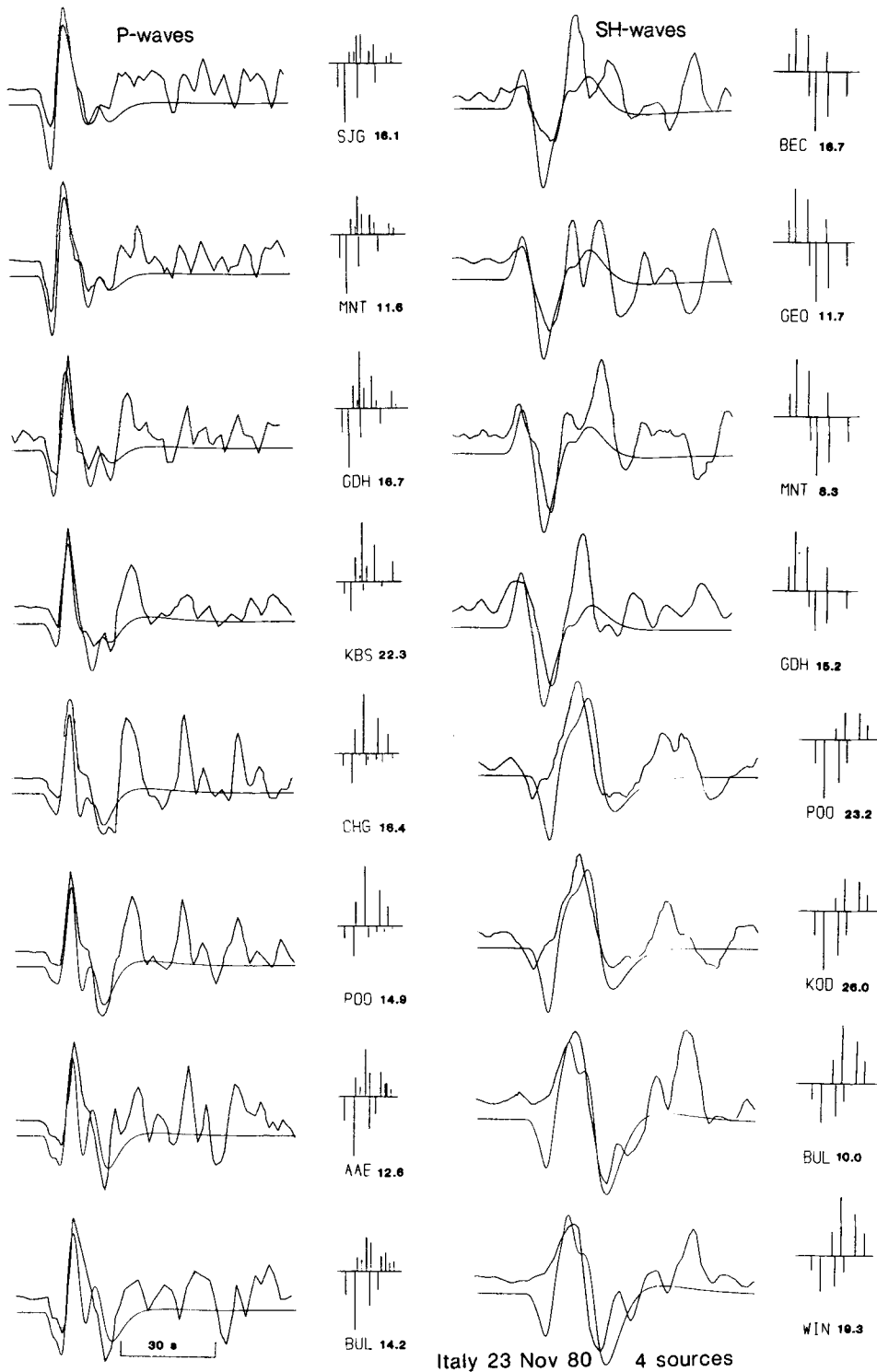


**Figure 15.** Observed and synthetic *P*- and *SH*-waves for our preferred three-source model, with an extra source to attempt to model the faulting in the Pantano di San Gregorio area.

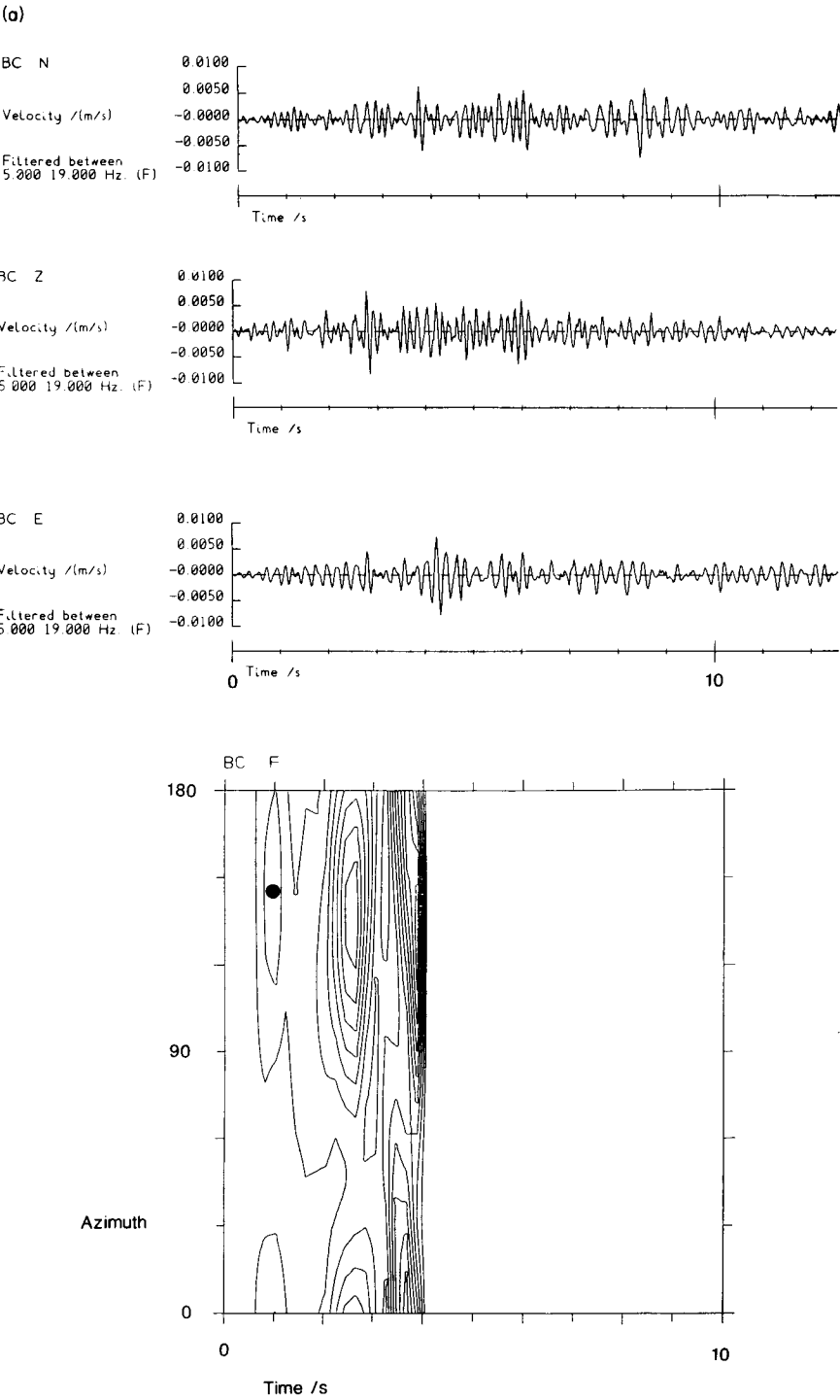
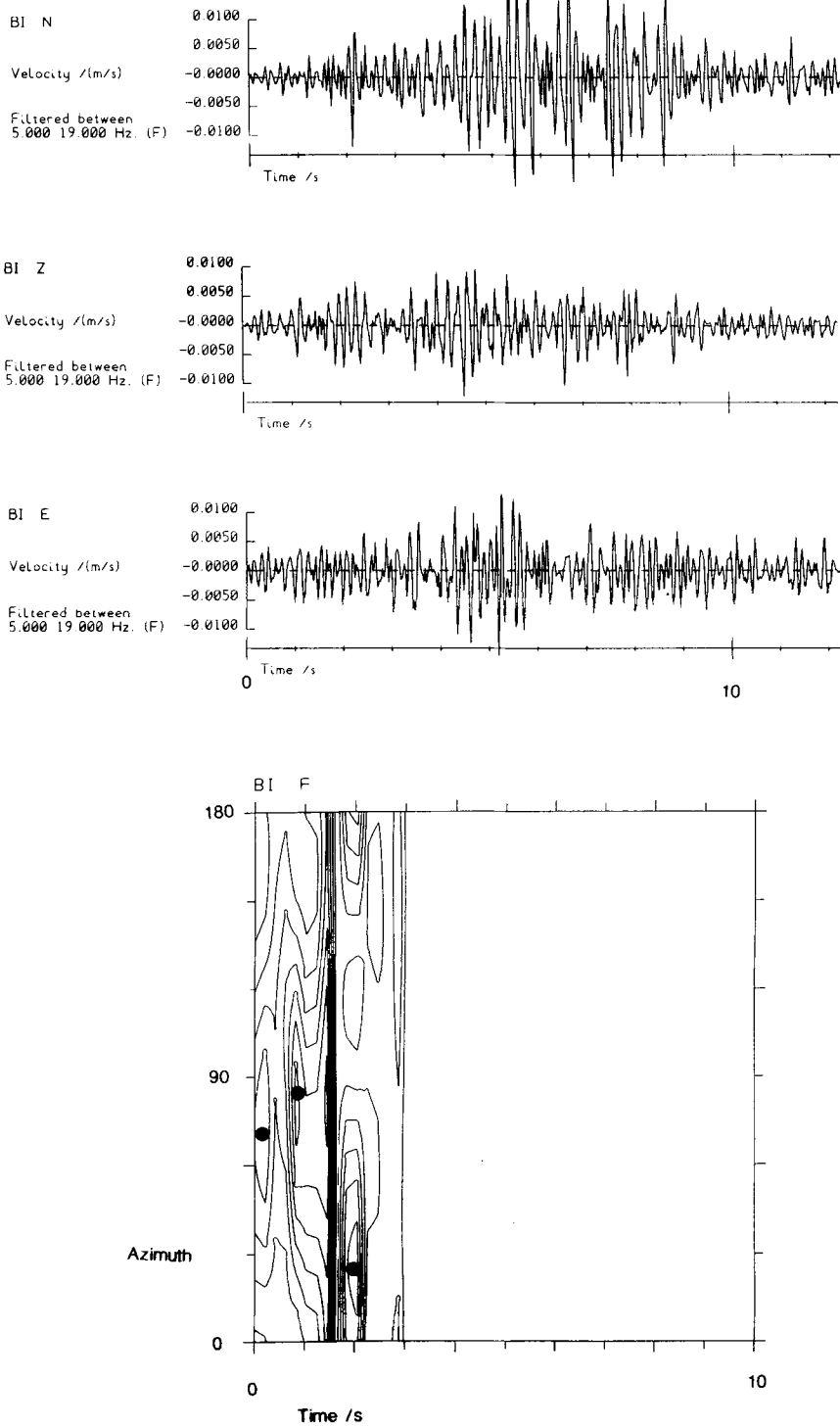


**Figure 16.** (This page and next four pages.) Filtered records of ground velocity and contours of  $X(\theta, t)$  (see text) for  $0 < \theta < 180^\circ$  and  $0 < t < 10$  s after trigger time, at stations BC (a), BI (b), CL (c), RV (d) and ST (e). The contour intervals are equal, and local maxima of  $X$ , that indicate the direction of  $P$ -wave particle motion, are marked with dots.

(b)



(c)

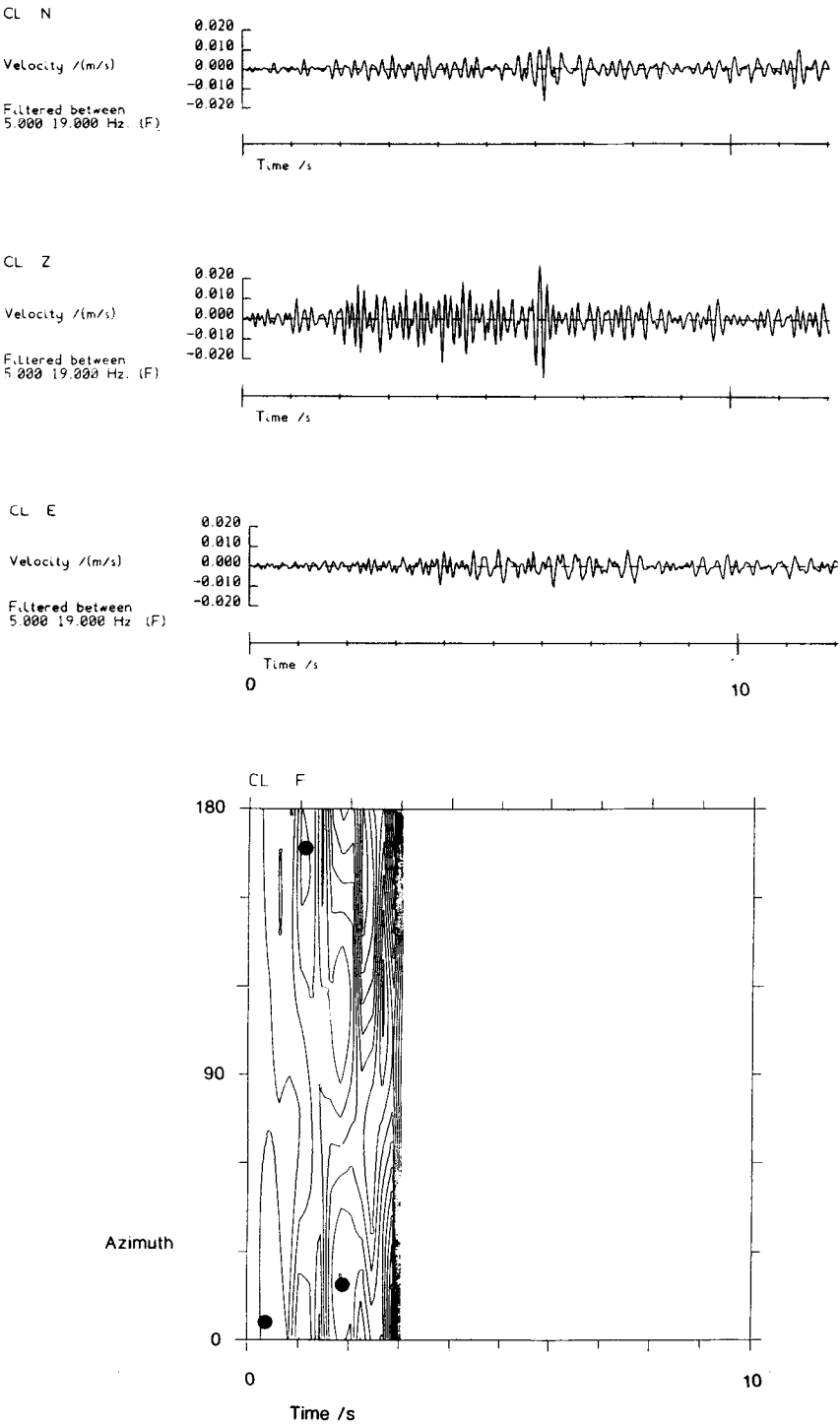
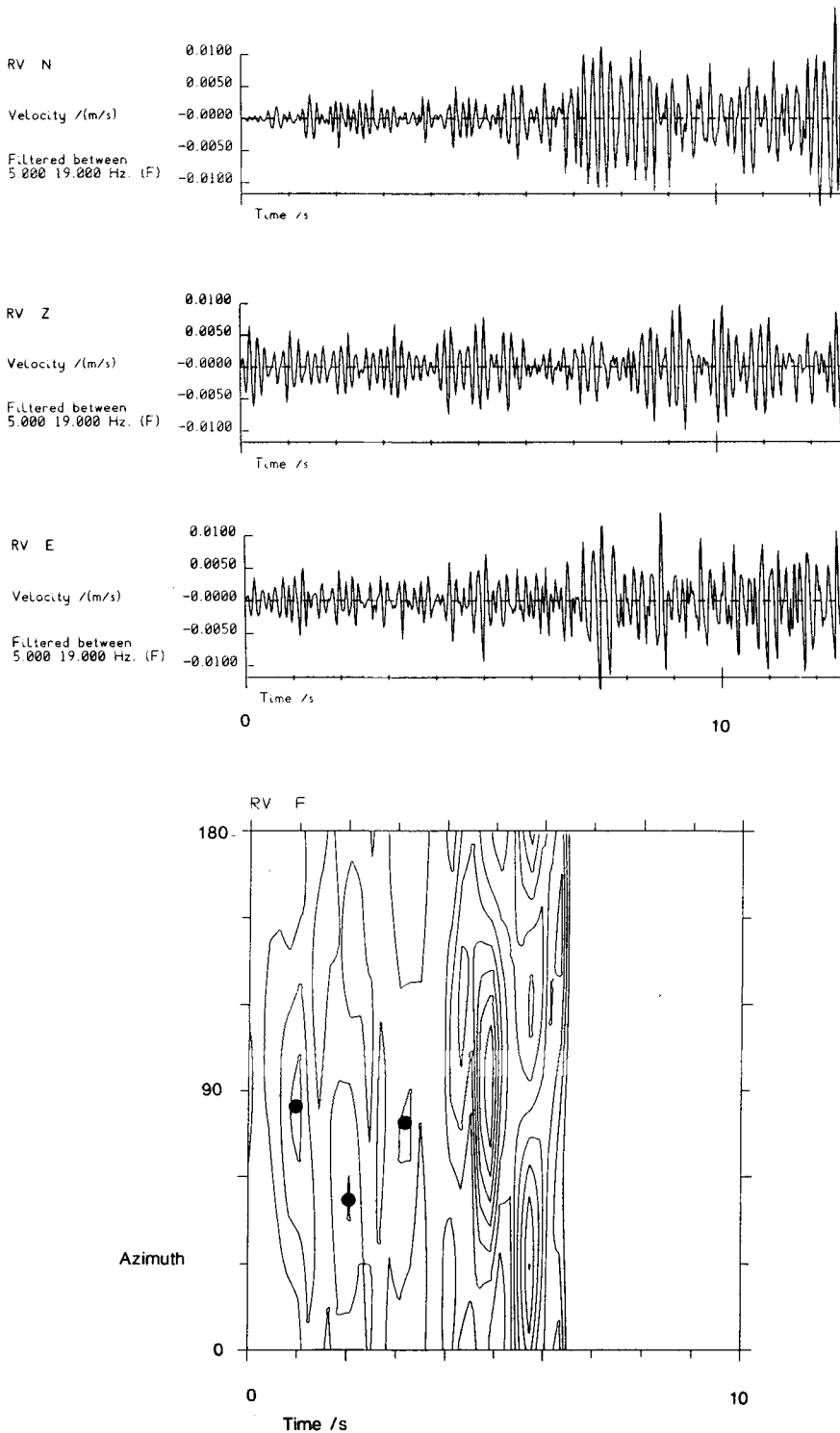


**Figure 16—continued**

(d)



(e)

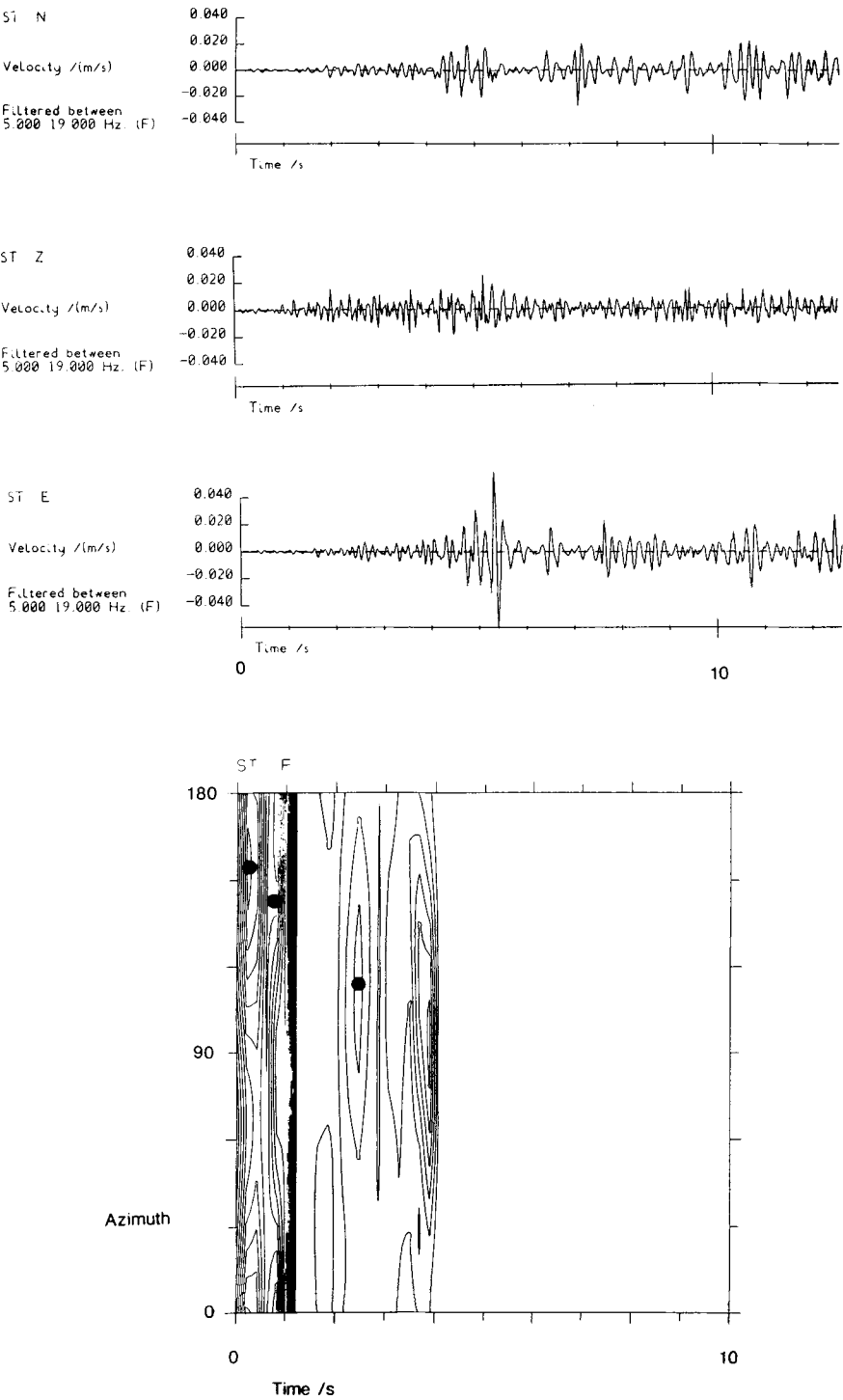
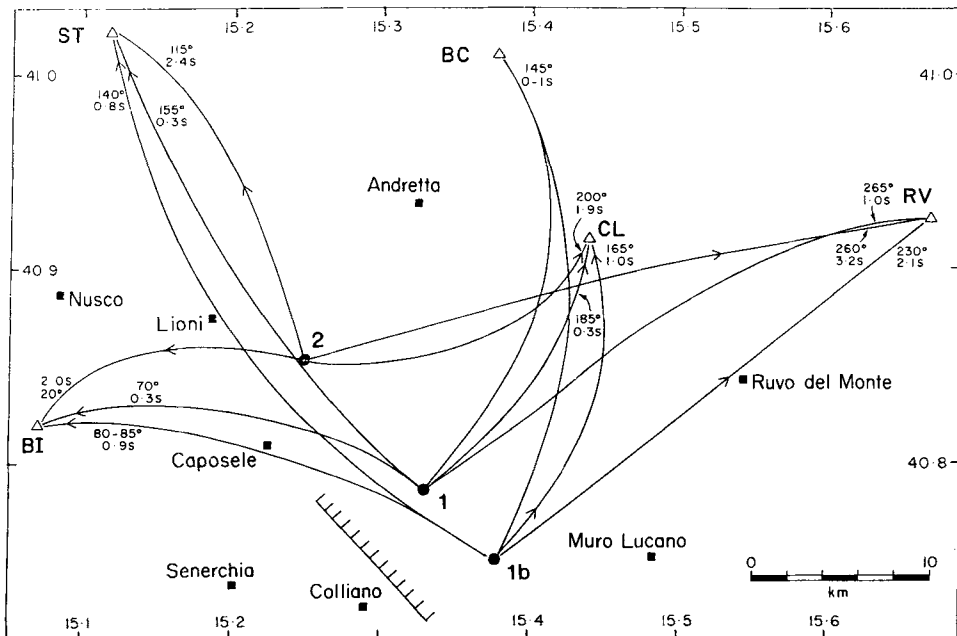


Figure 16—continued



**Figure 17.** Sources of signals from the early mainshock ruptures using azimuths of *P*-wave particle motion. Here, the earliest pulse (1) observed at each station is shown as originating from a source beneath the epicentre determined from *P*-wave arrival times (Fig. 3). Between 0.4 and 2.0 s after-trigger time, signals reaching the stations are consistent with a source further SE of this position (1b). After this, the signals reaching all stations are consistent with a source further NW (2). See text for discussion.

17). By 2 s after trigger time, the signals appear to arrive from a region NW of the first subevent hypocentre (source 2 in Fig. 17). Like those for the 40 s subevent (Fig. 14), ray paths in Fig. 17 have been drawn with smooth curvature. The significant effect is the variation in signal azimuth with time, which is in a consistent sense at all stations, and not the precise azimuths, that may depend on details of the velocity structure beneath each station. This analysis depends on all the signals being *P*-waves not *S*-waves. We think this is justified because the distance between the stations and the first subevent hypocentre is, in all cases, such that the *S*–*P* interval would exceed 3 s. In Fig. 17, source 2 is in the same place used for modelling the long-period waveforms (Section 5) of the subevent nucleating 2.5 s after the first motion. It is possible that the *P*-wave pulse apparently originating at the SE end of the Monte Marzano segment of surface faulting, was radiated when the fault rupture reached the end of this segment. The pulses about 2 s after the start of each record, which appear to originate NW of the hypocentre, are probably from the start of the rupture on the Monti Picentini fault segment.

In summary, the records of ground acceleration suggest that the first mainshock subevent nucleated near the NW end of the Mont Marzano fault segment (consistent with our preferred hypocentre from Section 3) and propagated SE. Two seconds later, rupture initiated near the SE end of the Monti Picentini segment and propagated NW. It was presumably rupture on the Monti Picentini fault segment that caused the large amplitude ground acceleration at stations to the NW. The strong signals observed at AU and BZ between 10 and 15 s after trigger time are consistent with their source having been faulting SE of the hypocentre of the first subevent. We suggest that this faulting occurred beneath



the Pantano di San Gregorio, where some surface faulting (Section 2) and local intense aftershock activity (Section 10) were observed. The source of the strong signals 40 s after trigger time was about 10–15 km NNE of the hypocentre of the first subevent.

## 9 Modelling of long-period waveforms of late mainshock ruptures

In Section 5, the first 15 s of long-period teleseismic *P*- and *SH*-wave records were modelled to determine the geometry of faulting in the first three mainshock ruptures. In Section 8 it was further suggested that a few more seconds of the teleseismic records can be accounted for by an additional rupture on a steep normal fault around the Pantano di San Gregorio, where a short segment of surface faulting was observed (Fig. 2). Fig. 5 indicates that large amplitude signals are visible on *P*-wave records at many teleseismic stations about 20 and 40 s after the first motion. The second of these occurs at the same time as the late signals observed on short-period records of ground acceleration (Fig. 12a). The similarity in timing suggests that both sets of delayed signals are produced by additional late mainshock ruptures. In this section, the geometry of faulting in these ruptures is investigated.

The late arrivals that are observed teleseismically occur at the same time, at about 20 s and 40 s, at all stations where they are observed (GDH, AKU, ALE, COL, KBS, KEV, MAT, SHK, SHL, CHG, QUE, POO, KOD and AAE in Fig. 6b). They are also observed on the horizontal component records (Fig. 6b) and have the same amplitude, relative to the signal from the early ruptures, on all three components of ground motion. This also indicates that they represent late *P*-wave signals from the source (i.e. with the same ray parameter as the first arrival) rather than conversions below the receiver. The late arrivals are unlikely to be caused by reverberations within a complicated receiver velocity structure, because records at widely separated stations, for example AAE in Ethiopia, POO in India and SHK in Japan, have similar appearance. Structural complexity could also exist in the source region. However, seismograms from the smaller earthquakes of 1962 August 21, that occurred only 50 km from the 1980 event (Westaway 1987a), do not show similar late pulses. Having excluded these possibilities as causes of the seismogram complexity, it is worthwhile pursuing the obvious suggestion from the ground acceleration records (Section 8), that these later complexities are caused by rupture in additional subevents, and to see whether a source model can be found that can match them.

### 9.1 THE 20 S SUBEVENT

The main features to be modelled are the large amplitude compressional pulses in the *P*-wave records at stations to the NE and E. These pulses are also present at smaller amplitude on records from stations to the N and SE, but virtually absent on records from stations at other azimuths. These compressional pulses are not followed by significant dilatational pulses. The most obvious way to produce such a pattern is by the constructive interference of the compressional backswing from dilatational *P* pulse with a compressional pulse from either *pP* or *sP*. To obtain the largest amplitudes at stations to the NE and E one nodal plane of the focal mechanism should strike between S and SE and dip steeply SW. Fig. 18 shows observed and synthetic *P*- and *SH*-wave seismograms incorporating the first three subevents and the Pantano di San Gregorio subevent, with an additional subevent 19 s after the origin time. This later subevent has a focal mechanism with dip 20°, strike 320° and rake −105°. This model can account for the relative amplitudes and azimuthal distribution of the compressional pulses about 25 s into the records. At stations to the NE the dilatational

*P*-wave pulse from the 19 s subevent also contributes to the large amplitude dilatation that precedes this compressional pulse. This additional subevent can account for the positive pulses present in *SH*-waveforms from BUL and WIN to the south about 25 s after the start of the record, and the second part of the double positive pulse observed at BEC, GEO and MNT to the west. It also produces a relatively small *SH*-wave signal at POO and KOD, to the east, consistent with the observed lower amplitudes between 20 and 40 s in comparison with earlier in the records.

This subevent is not as well constrained as the early ones. However, some source parameters, particularly the dip of the nodal planes, are more important than others. Fig. 19 shows the variation in synthetic *P*- and *SH*-wave seismograms at MNT and POO due to changes in dip of the NE-dipping nodal plane of the additional subevent. When this nodal plane has dip  $2^\circ$ , amplitudes of synthetic *SH*-wave seismograms at both stations are too large, and synthetic *P* waves at MNT are too small. When it has dip  $40^\circ$ , synthetic *SH*-wave amplitudes at both stations are too small; both stations lie close to nodal surfaces in the *SH*-wave radiation pattern. When the dip of this nodal plane is changed to  $60^\circ$ , both stations cross a nodal surface of the *SH*-wave radiation pattern, and the synthetic *SH*-waves look very unlike those observed. Changing the rake of the focal mechanism by  $\pm 15^\circ$ , does not substantially alter the synthetic seismograms.

The synthetic *P*- and *SH*-waves provide a strong constraint on the origin time of this fifth subevent. At a focal depth of 12 km, the best match to the observed *P*-waves is with an origin time 18 s after the first subevent. However, this origin time gives a poor match for *SH*-waves, failing to reproduce the double positive pulse observed at stations to the W. The best match for *SH*-waves is obtained with the origin time of the fifth subevent delayed to 21 s. Fixing the origin time at 19 s gives a reasonable match for both *P*- and *SH*-waves. The observed seismograms are not strongly sensitive to the position of the source used to model this subevent. A position 6 km N of the hypocentre has been assumed here, because, as will be seen later, of the similarity of this 20 s subevent with the 40 s subevent. The time-function of this 20 s subevent must be relatively long in order to match the duration of the large-amplitude compressional pulses in the *P*-wave records, produced by interference of the backswing from *P* with *sP*, at CHG and POO to the E (Fig. 18). In the models already discussed, a symmetrical triangular time-function of 8 s duration was used. If the subevent

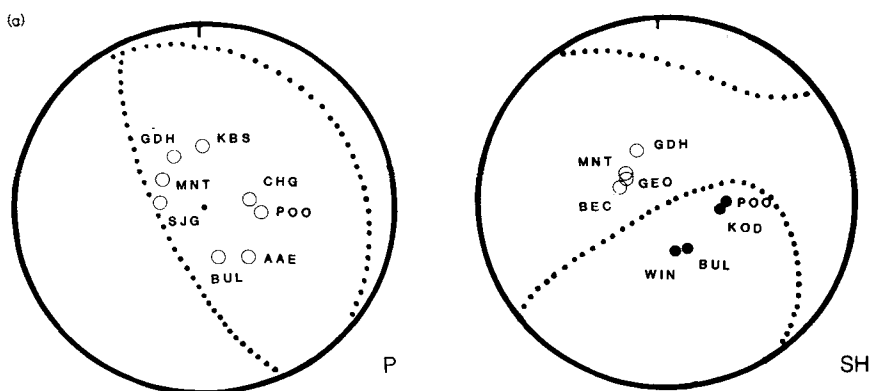


**Figure 18.** (Above and opposite.) (a) *P*- and *SH*-wave focal mechanisms, using the same projection as in Fig. 4, for a source with dip  $20^\circ$ , strike  $320^\circ$  and rake  $-105^\circ$ , showing the positions on the focal sphere of the stations used in waveform modelling. (b) Observed and synthetic *P*- and *SH*-waves for our preferred source model incorporating a late subevent, around 20 s after the origin time, with the orientation shown in Fig. 18(a).

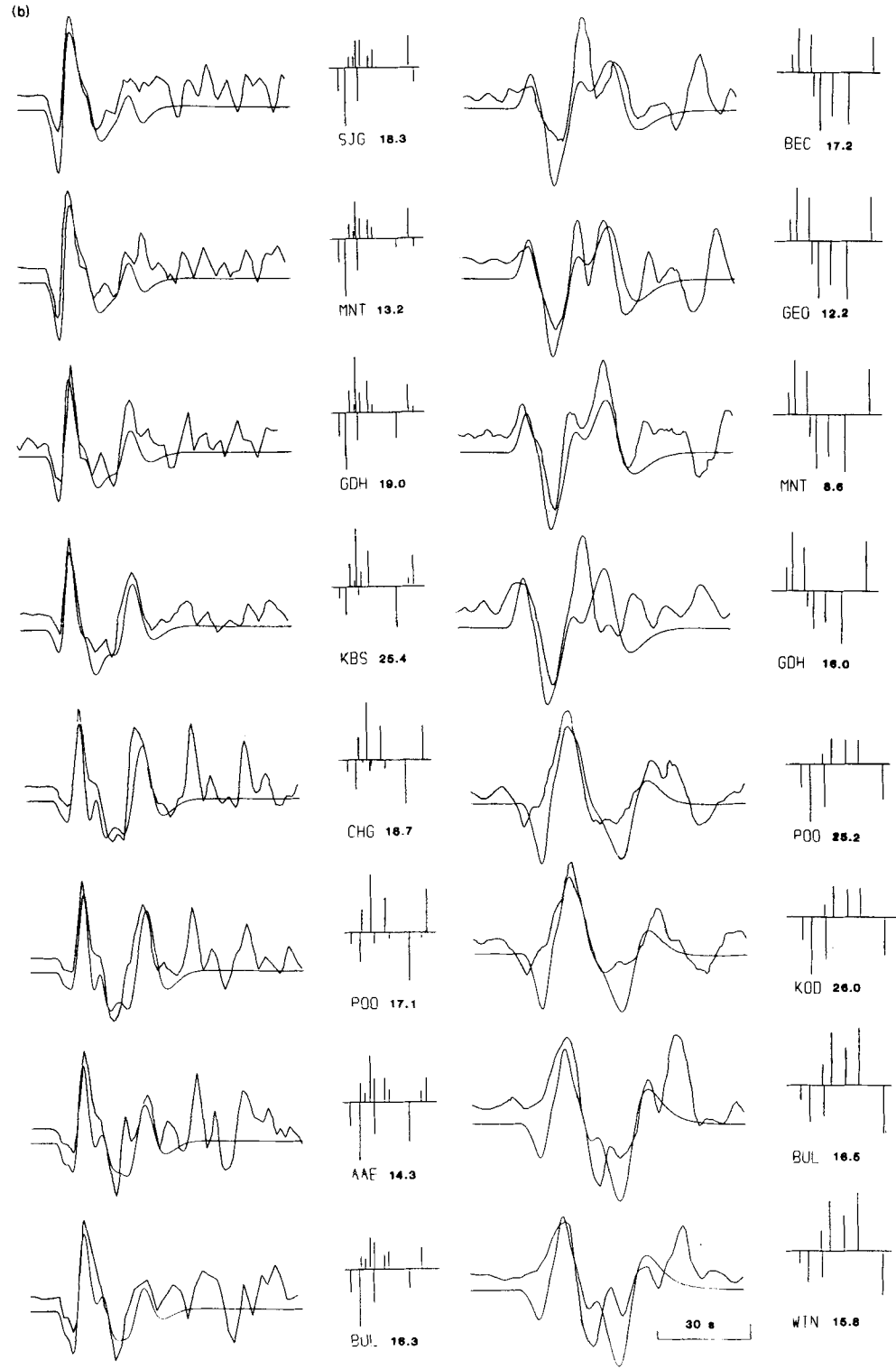
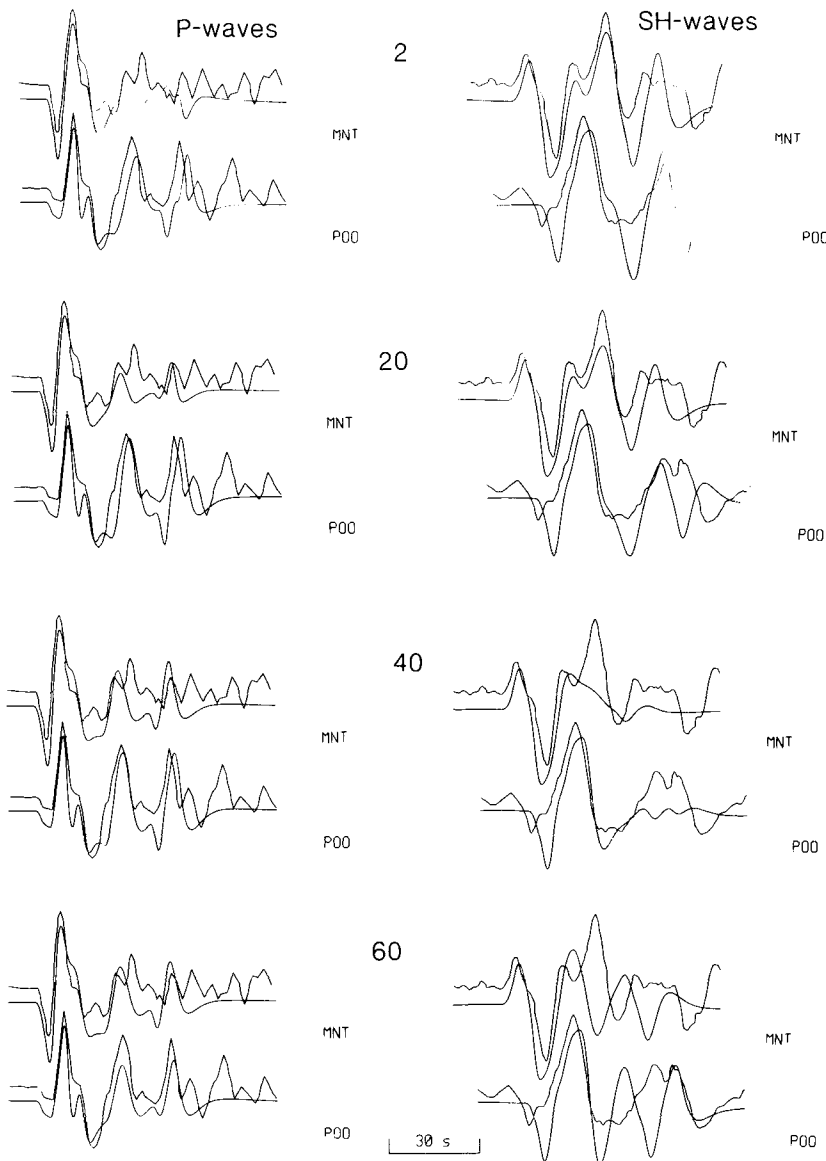


Figure 18 – continued

was deeper, at around 16 km, then a similar interference pattern for  $P$  can be produced with a shorter source time-function of 5 s duration. In this case the broadness of the compressional pulses is caused by the increased delay between  $P$  and  $sP$ . However, this alternative, deeper, source model produces less satisfactory matches between observed and synthetic  $SH$ -waves. Consequently, we prefer the model with the shallower source and longer-duration time-function.

Careful inspection of the ground acceleration records in Fig. 12(a) indicates that a signal from this 20 s subevent is identifiable, from changes in the frequency content of the records,



**Figure 19.** Observed and synthetic  $P$  (left) and  $SH$  (right) waveforms at MNT and POO for the preferred source model incorporating late ruptures around 20 and 40 s after the origin time. The late ruptures have strike 320° and rake -105°; synthetic seismograms are calculated for dips 2, 20, 40 and 60°.

at some stations (e.g. RV, ST and MS). However, at no station is this signal as strong as that from the 40 s subevent.

## 9.2 THE 40 S SUBEVENT

The *P*-wave radiation of the 40 s subevent shows a very similar azimuthal distribution to the 20 s one. Consequently, the most obvious starting point for modelling it is to assume it

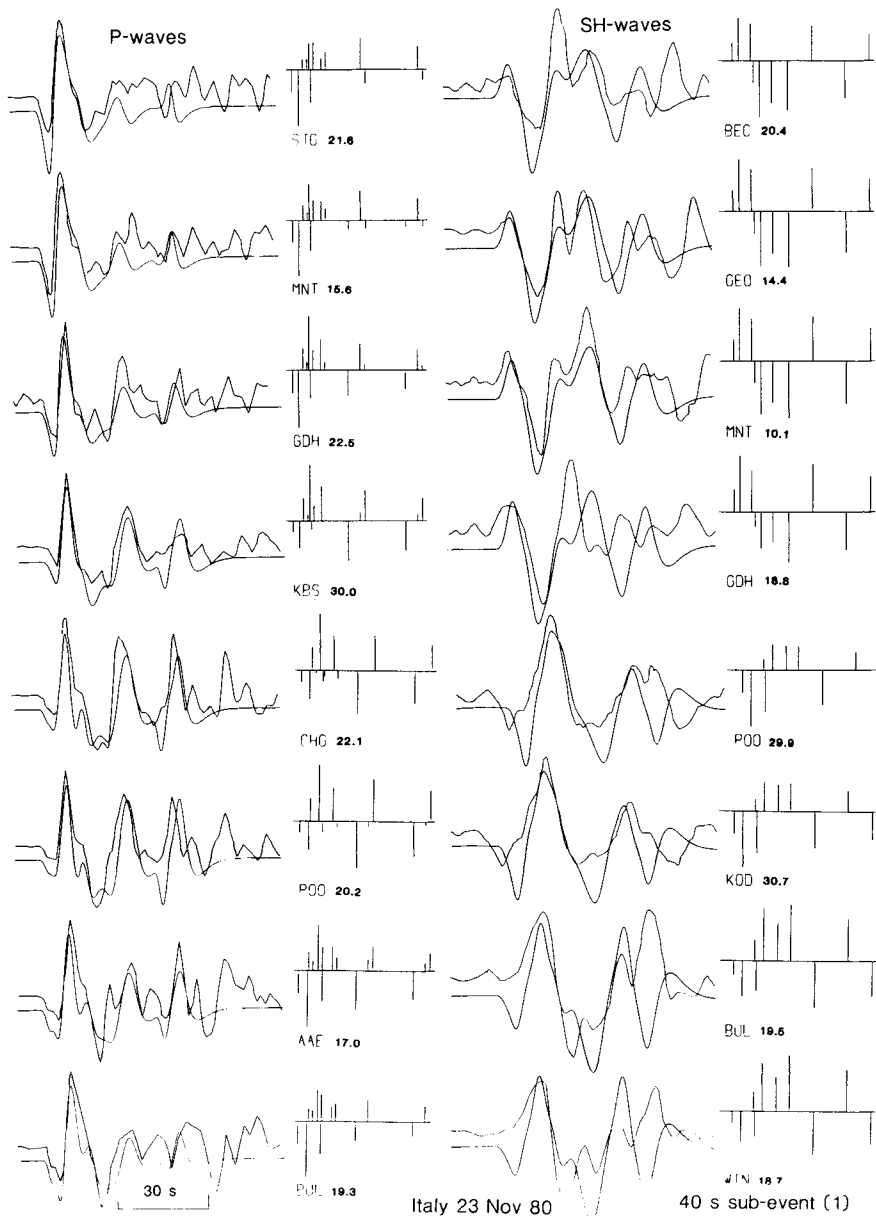


**Figure 20.** Observed and synthetic *P*- (left) and *SH*- (right) waveforms for our preferred source model incorporating two late subevents, around 20 and 40 s after the origin time. In this model, both late subevents have sources with the orientation shown in Fig. 18(a).

involved motion on a fault with the same orientation as that which moved in the 20 s subevent. Fig. 20 shows observed and synthetic *P*- and *SH*-wave records, in which an extra subevent has been added with this same orientation, a moment of  $3 \times 10^{18}$  Nm, and a time-function of 4 s duration, at an origin time 38 s after the first subevent. Because of computational limitations, the small San Gregorio subevent has been omitted. With a delay approaching 40 s, *P*-waves from this subevent arrive earlier than *PcP* from the first subevent only at POO, AAE, GDH and KBS, and *S*-waves arrive earlier than *ScS* from the first subevent only at POO, BUL, WIN and GDH. *P*-wave records are matched adequately at all stations shown in Fig. 20 but *SH*-wave records are not. The most serious mismatch is at stations BUL and WIN, to the S, at which a large amplitude negative pulse occurs in the synthetic seismograms at a time (about 42 s after the first *S*-wave motion) when the observed seismograms show a large amplitude positive pulse.

The suggestion of Key & Crosson (1984) and Crosson *et al.* (1986) that the 40 s subevent involved motion on a steep normal fault striking NE and dipping SE has already been mentioned in Section 8. Observed and synthetic *P*- and *SH*-wave seismograms for a source model with this orientation are compared in Fig. 21. This model manages to match the form of observed *SH*-wave records at BUL and WIN. However, the match of the *P*-waves is unsatisfactory. The model generates large amplitude compressional *P*-wave pulses at stations to the W and small amplitude signals at stations to the N and E. Over 100 models were tested in order to find one that gave a satisfactory match to the observed *P*-waves and could also match the form of the observed *SH*-waveforms at BUL and WIN. However, no model that matched both could be found.

The orientation of the focal mechanism of the late mainshock ruptures, determined above by waveform modelling, can be checked by decomposition of the overall moment tensor determined in Section 7. If a tensor with the orientation in Fig. 18(a), with moment  $7 \times 10^{18}$  Nm (equal to the sum of the moments of the two late ruptures), is subtracted from our preferred overall moment tensor, incorporating both GDSN and WWSSN records (tensor D in Table 4), the result is a tensor with a similar orientation to the early mainshock ruptures, and moment  $20 \times 10^{18}$  Nm. Alternatively, if a tensor (tensor F in Table 4) with the same orientation as the first subevent and moment  $20 \times 10^{18}$  Nm is subtracted from tensor D

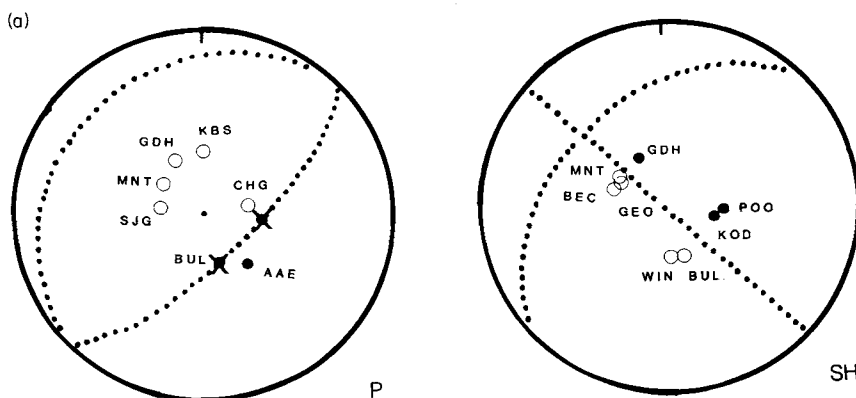


**Figure 21.** (Above and opposite.) (a) *P*-wave and *SH*-wave focal mechanisms, using the same projection as in Fig. 4, for a source with dip  $70^\circ$ , strike  $45^\circ$  and rake  $-90^\circ$ , showing the positions on the focal sphere of the stations used in waveform modelling. (b) Observed and synthetic *P*- (left) and *SH*- (right) waveforms for a source model incorporating two late subevents, around 20 and 40 s after the origin time. Here, the first of these sub-events has the orientation shown in Fig. 18(a) and the second that shown in Fig. 21(a).

in Table 4, the result is a tensor (tensor G in Table 4; number 6 in Fig. 11a) with the same scalar moment,  $7 \times 10^{18}$  Nm, and a similar orientation to the focal mechanism determined by waveform modelling for the late mainshock ruptures (Fig. 18a). This decomposition also suggests that in addition to the  $15 \times 10^{18}$  Nm of moment accounted for by the first three subevents in Section 5, and by the San Gregorio subevent in Section 8, another  $5 \times 10^{18}$  Nm may also have been released on steep normal faults striking NW. We recall that in Section 5 that adding moment to the third subevent reduced the amplitude of the synthetic seismograms by destructive interference. Consequently, it is possible that additional moment

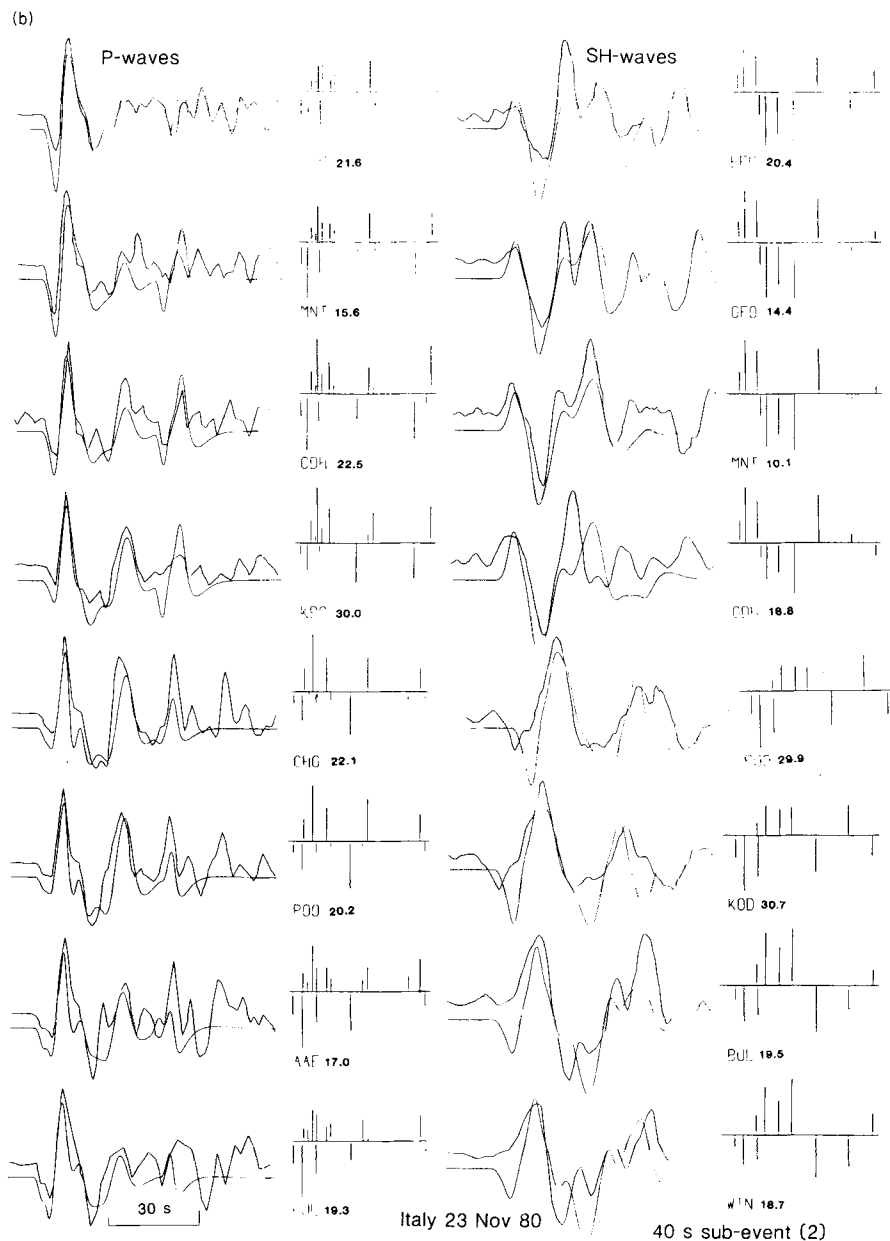


Figure 21—continued

release occurred around the same time as the first three subevents, but which left the waveform amplitudes largely unaltered. We suggest that this extra moment may have occurred in several small subevents that do not markedly influence the synthetic seismograms. These additional ruptures may have occurred NW of Nusco (Fig. 3), where aftershock activity occurred that was less intense than around the segments of mainshock faulting already identified. A potential problem with the use of this decomposed moment tensor is that the delay of the 40 s rupture is comparable to the period (45–60 s) of the filtered signals used in the determination of the moment tensor. However, because the centroid time was 16 s after the nominal origin time, and the source was modelled with a duration of 30 s centred on this centroid time, the phase of the signals from both the 20 and 40 s subevents is likely to have been adequately modelled. The decomposed moment tensor analysis suggests that the 40 s subevent did have a similar focal mechanism to the 20 s subevent. It does not help to explain why the waveform modelling above cannot match some of the *SH*-waveforms, though it does suggest that the suggestion made by Key & Crosson (1984) and Crosson *et al.* (1986) concerning the orientation of the faulting in the 40 s subevent is wrong.

To summarize, a focal mechanism for the 40 s subevent the same as that of the 20 s subevent produces a reasonable match to the observed *P*-wave arrivals. No substantially different model could be found that produced a significantly better match to the *P*-wave records or could match both the *P*-wave records and the *SH*-wave records at stations to the S.

## 10 Relationship between mainshock and aftershocks

Following the mainshock, a network of 37 temporary seismographs was installed in the epicentral area and was operated for several weeks to record aftershocks. We use results from this aftershock survey to investigate aspects of the relationship between faulting in the mainshock and in the aftershocks, that are relevant to our discussion of the geometry of faulting as a whole. Three points are considered here. First, the interpretation of Deschamps & King (1984), that several aftershocks of the normal-faulting mainshock have reverse-faulting focal mechanisms whose nodal planes strike NW, is confirmed, and we investigate the relationship between these aftershocks and the geometry of faulting in the mainshock. Secondly, the distribution of seismic moment from aftershocks is shown to be related to the geometry of faulting in the mainshock that we determined in the previous sections. Thirdly, the overall interpretation of the aftershocks by Deschamps & King, mentioned in Section 1, is shown to be wrong.

Deschamps & King (1984) and Westaway (1985) have each located more than 1000 aftershocks with  $M_L > 2$ . Both studies used the location program HYPO71 (Lee & Lahr 1975). Deschamps & King worked with layered crustal velocity models, while Westaway used a modified version of this program that allowed a vertical velocity gradient to be used. Root mean square travel-time residuals, averaged over many aftershocks, are comparable for both velocity models, and, for well-constrained events, hypocentres from both studies usually lie within 1 km of one another. This indicates that sufficient data exist for the choice of parameterization of velocity model not to have a significant effect on hypocentral locations. In both studies, many aftershocks could be located with standard errors in each hypocentral coordinate of the order of 1 km. Deschamps & King also determined 160 aftershock focal mechanisms, many of which were similar to the mainshock, involving normal faulting with nodal planes striking NW. About 15 per cent of their focal mechanisms, however, involved reverse faulting with nodal planes striking NW. Deschamps & King found mechanisms of this type throughout the aftershock zone. Inspection of these mechanisms (fig. 7 of Deschamps & King 1984) indicates that many of them are constrained only by identifying one or more



*P*-wave polarities as nodal, and then fitting nodal planes to pass close to these apparently nodal stations. Deschamps & King did not state how they identified nodal *P*-wave arrivals, and, because of potential multipathing in local velocity structure, we are not confident that nodal arrivals can be reliably identified. If the nodal first motions are reclassified either as ordinary first motions of appropriate polarity, or are discarded as being ambiguous, then most of these reverse-faulting focal mechanisms become poorly constrained. Apart from mechanisms with one very steep nodal plane striking NW that, with a small adjustment, may indicate either normal or reverse faulting, only four well-constrained reverse faulting mechanisms exist (Fig. 22), all of which are located close to the northern end of the Sele valley. Fig. 22 also shows 10 focal mechanisms determined by Westaway (1985) with nodal planes striking NE, from the same area, and from around Nusco, further NW, where another transverse structural discontinuity, similar to the Sele valley, interrupts the north-westward trend of the Apennines. The concentration of aftershock focal mechanisms very different from that of the mainshock near discontinuities in geological structure, has also been observed in other earthquakes (e.g. by Whitcomb *et al.* 1973, for aftershocks of the San Fernando, California, earthquake of 1971 February 9). However, around these discontinuities, as elsewhere, both Deschamps & King (1984) and Westaway (1985) found that focal mechanisms similar to that of the mainshock are much more numerous than these

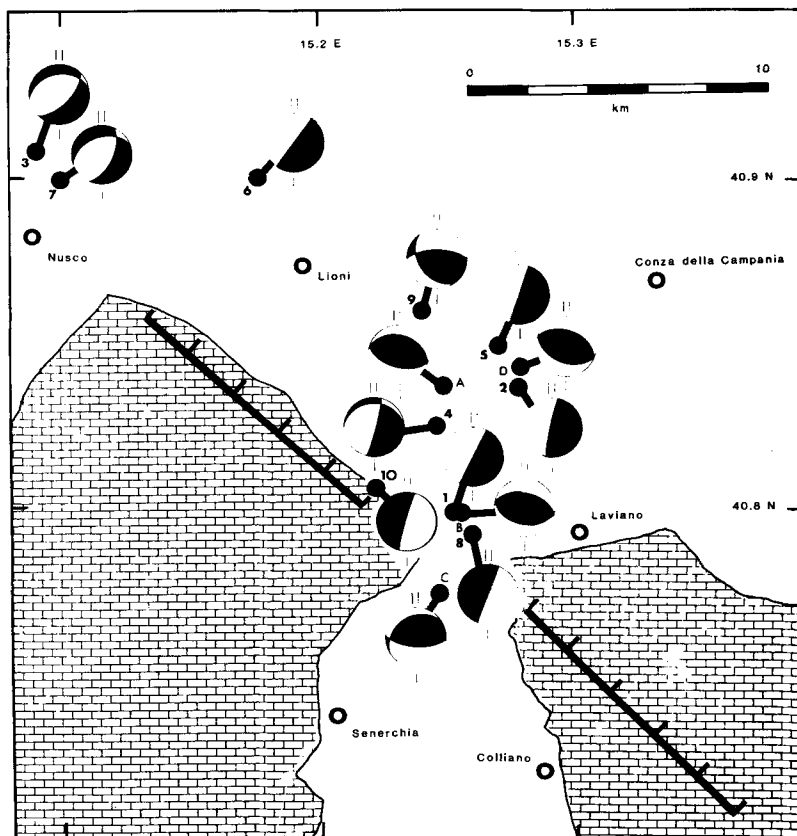


Figure 22. Map of the area around the northern end of the Sele valley, showing epicentres of 14 'anomalous' aftershocks, listed in Table 8, with focal mechanisms substantially different from the mainshock. Other aftershocks with focal mechanisms similar to the mainshock, that were much more numerous, are not shown in order to preserve clarity.

**Table 8.** Locations and focal mechanism for the 14 aftershocks displayed in Fig. 22. Dip and strike of the nodal planes are denoted by  $\delta$  and  $\phi$ . The polarity in each quadrant of each focal mechanism can be determined by inspection of Fig. 22. Events 1–10 are from Westaway (1985) and events A–D from Deschamps & King (1984).

	Origin time	Latitude	Longitude	Depth / km	$M_L$	Focal mechanism			
						$\delta$	$\phi$	$\delta$	$\phi$
1	7-12-80 07:06	10.6	40 47.94N	15 15.04E	11.88	3.0	90 025	0 205	
2	11-12-80 11:07	40.3	40 50.20N	15 16.56E	11.72	2.7	85 192	5 012	
3	11-12-80 19:56	04.8	40 54.64N	15 05.25E	8.16	2.4	62 045	33 260	
4	12-12-80 01:59	13.0	40 49.55N	15 14.61E	10.43	2.4	85 015	20 271	
5	12-12-80 05:34	09.9	40 50.98N	15 16.11E	12.31	3.2	90 020	0 200	
6	12-12-80 12:45	39.3	40 54.12N	15 10.45E	8.45	2.5	90 035	0 215	
7	12-12-80 17:46	33.2	40 54.11N	15 05.79E	7.77	2.6	40 250	60 024	
8	12-12-80 19:29	51.4	40 47.54N	15 15.40E	11.93	2.7	90 020	0 200	
9	12-12-80 22:02	40.3	40 51.47N	15 13.70E	9.10	2.1	65 270	39 145	
10	14-12-80 07:16	40.0	40 48.42N	15 13.14E	14.61	2.5	85 200	5 020	
A	10-12-80 15:50	24.7	40 50.26N	15 14.79E	13.99	3.4	35 288	55 108	
B	10-12-80 17:55	33.0	40 47.94N	15 15.10E	9.33	2.7	42 102	48 282	
C	12-12-80 20:37	28.6	40 46.50N	15 14.31E	12.31	2.7	65 095	30 240	
D	14-12-80 22:56	39.0	40 50.59N	15 16.64E	12.45	2.5	45 290	45 110	

other orientations. They are omitted from Fig. 22 to preserve clarity. We agree with the conclusions of Deschamps & King (1984) that minor reverse-faulting earthquakes cannot be taken to imply regional compression: a result with obvious geological implications (e.g. Jackson, King & Vita-Finzi 1982b).

Westaway (1985) determined local magnitudes  $M_C$  from coda durations (Bakun 1984) and, using the moment ( $M_0$ )–magnitude relation

$$\log_{10}(M_0/\text{Nm}) = 9.0 + 1.5 M_C,$$

estimated moments of individual aftershocks and hence the cumulative moment for 1498 aftershocks that occurred between December 5 and 15 (Fig. 23a). He estimated that these aftershocks accounted for about 7 per cent of the moment of the complete aftershock sequence. Using the above moment–magnitude relation, the total moment released throughout the aftershock sequence can be estimated as of the order of 1 per cent of the moment released in the mainshock. Thus the total deformation of the epicentral area caused by aftershocks was much smaller than that caused by the mainshock. The largest aftershock ( $M_L = 4.9$ ) occurred at 23:54 on 1980 December 3. Its moment was less than one-thousandth of the moment released in the mainshock.

To estimate the spatial distribution of moment from aftershocks, the moment of each aftershock has been distributed over elements, occupying a volume equal to the standard error ellipsoid for each event, of a cuboidal mesh extending throughout the aftershock zone, and the moments about each mesh element have been summed. Fig. 23(a) shows a plan view of the aftershock area showing contours of cumulative aftershock moment-density (in  $\text{Nm}^{-1}$ , or  $\text{Nm}$  per unit horizontal area). The figure also shows areas where faulting is inferred to have occurred during the mainshock, from other evidence. Areas of maximum aftershock moment-density lie along these segments of fault. Moment density has its peak value ( $> 2 \times 10^7 \text{Nm}^{-1}$ ) close to the observed or inferred Monte Marzano, Monti Picentini and San Gregorio segments of mainshock faulting. It decreases much more rapidly SW into the foot-wall, then NE into the hanging wall, where high moment-density extends for more than 10 km. Fig. 23(b) shows a vertical section 6 km thick across the Monte Marzano segment of faulting, showing contours of cumulative aftershock moment per unit volume (in  $\text{Nm}^{-2}$ ),

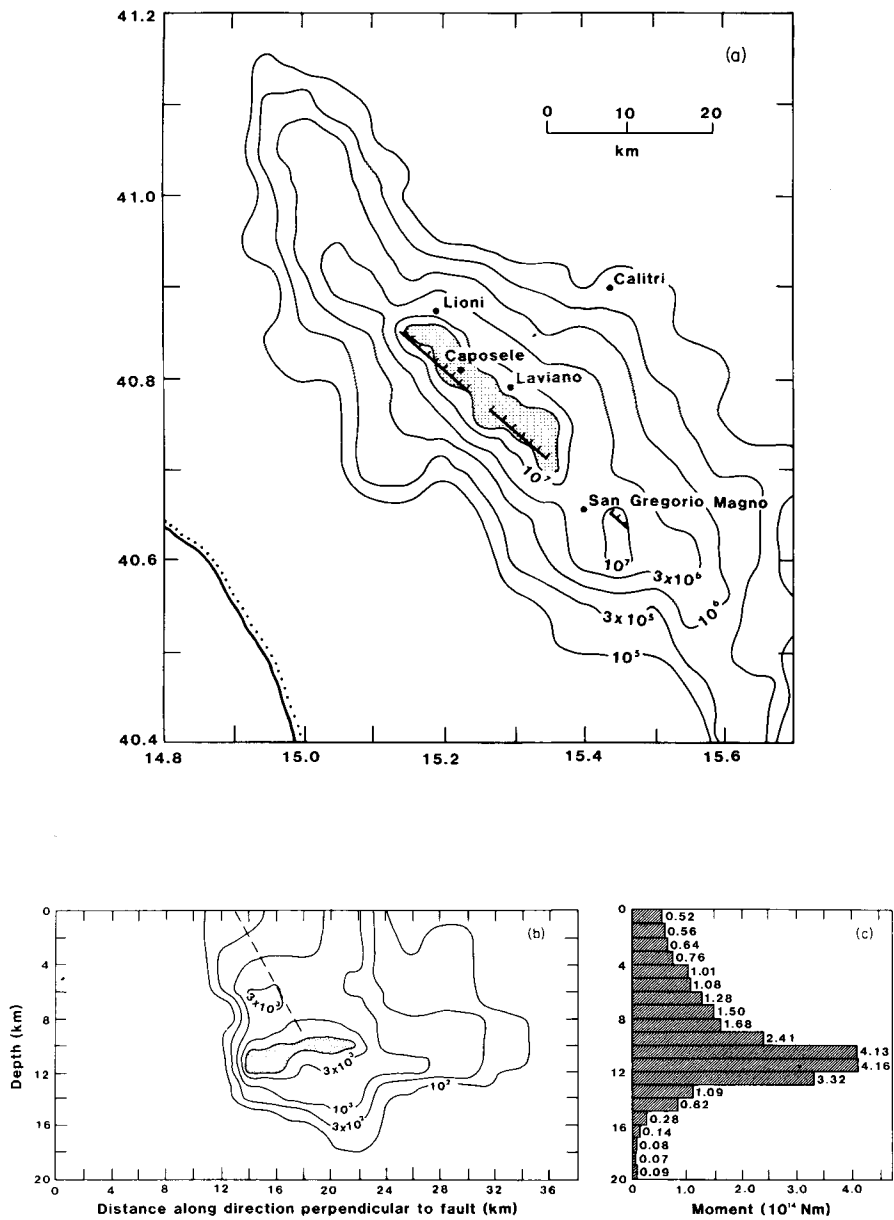


**Figure 23.** Cumulative seismic moment for aftershocks between 1980 December 5 and 15. (a) Plan view of the aftershock area showing contours of cumulative aftershock moment-density (in  $\text{Nm}^{-1}$ , or  $\text{Nm}$  per unit horizontal area). The figure also shows areas where faulting is inferred from other evidence to have occurred during the mainshock. Areas of maximum aftershock moment-density ( $> 2 \times 10^7 \text{ Nm}^{-1}$ ; shaded) lie along these segments of fault. (b) Vertical section striking at  $\text{N } 47^\circ \text{ E}$  across the Monte Marzano segment of faulting, showing contours of cumulative aftershock moment per unit volume (in  $\text{Nm}^{-2}$ ), and their relationship to a downward projection of the observed surface faulting. The zone of maximum ( $> 6 \times 10^3 \text{ Nm}^{-2}$ ) cumulative aftershock moment per unit volume, situated between 10 and 12 km focal depth, largely in the footwall, is shaded. The centre-line of this section extends between  $40.642^\circ \text{ N}$ ,  $15.188^\circ \text{ E}$  and  $40.893^\circ \text{ N}$ ,  $15.535^\circ \text{ E}$ . The section indicates moment that was released within 3 km of this centre-line, on either side. (c) Histogram of cumulative aftershock seismic moment in 1 km thick horizontal slices, from 0 to 20 km depth, for the section shown in Fig. 23(b).

and their relationship to a downward projection of the observed Monte Marzano segment of surface faulting. Most of the moment in aftershocks is released around 10–12 km depth, in a zone extending from a point in the footwall below the surface faulting, into the hanging wall. Further into the footwall, aftershock activity was negligible, though it extended for more than 10 km into the hanging wall. Stein & Barrientos (1985) reported a similar distribution, with aftershock activity most intense in the footwall close to the mainshock fault plane, for the Borah Peak, Idaho, earthquake of 1983 October 28. Fig. 23(c) shows the same information as Fig. 23(b), but displayed as a histogram. The small amount of seismic moment shown deeper than 12 km is mostly caused by shallower aftershocks that are poorly located, for which the moment is distributed over a large depth range because of the large standard errors in their focal depths. The seismic moment shown shallower than 10 km depth is partly caused by poorly located, deeper, events but mostly caused by well-located events that occurred in this depth range. Deschamps, Iannacone & Scarpa (1984) reported a similar depth-distribution for the frequency of occurrence of aftershocks following the Norcia normal-faulting earthquake, which occurred in the central Apennines on 1979 September 19. They did not calculate the distribution of seismic moment for their sequence of aftershocks, but found that very few aftershocks were located deeper than 12 km. Thus, both Deschamps *et al.* and this study suggest that the depth at which crustal deformation changes from being predominantly brittle to predominantly ductile is around 12 km in the Apennines.

Finally, we consider the interpretation of Deschamps & King (1984) for the overall pattern of the aftershocks. Deschamps & King noticed that many aftershock focal mechanisms have one very steep nodal plane striking NW, and one subhorizontal nodal plane. In all these mechanisms, the quadrant of the lower hemisphere of the focal sphere that lies to the NE receives compressional first motion. They interpret the subhorizontal nodal planes of these focal mechanisms as the fault planes, and suggest that these mechanisms are generated by brittle deformation adjacent to two subhorizontal ductile shear zones, one in the lower crust beneath the mainshock faulting, and the other between the mainshock faulting and the surface. In their model, these aftershocks accompany deformation on the inferred shear zones in which the upper plate moves to the NE, a sense of motion consistent with the geometry of normal faulting in the mainshock. However, aftershock focal mechanisms with the orientation described above imply motion in the *opposite* sense to this if the subhorizontal nodal plane is assumed to be the fault plane. Thus, the model suggested by Deschamps & King is not consistent with their observed aftershock focal mechanisms. We interpret the steep nodal plane of these aftershocks as the fault plane, and suggest that they occurred on normal faults that are subparallel (within 20–30°) to the steep normal faults that moved in the early ruptures of the mainshock.

To summarize, seismic moment from aftershocks is concentrated around the segments of fault that were either observed to have moved, or are inferred as having moved, during the mainshock. The strongest aftershock activity occurred close to the mainshock fault plane at the base of the footwall, but aftershock activity extended much further into the hanging wall, than into the footwall. Aftershock focal mechanisms very different from that of the mainshock are concentrated around transverse structural discontinuities between segments of mainshock faulting. However, these anomalous mechanisms are much less numerous than those that are similar to the mainshock.

## 11 Discussion

We have shown, by a variety of studies, that the mainshock of 1980 November 23 involved a complicated sequence of fault ruptures (Fig. 24). The total seismic moment released in the

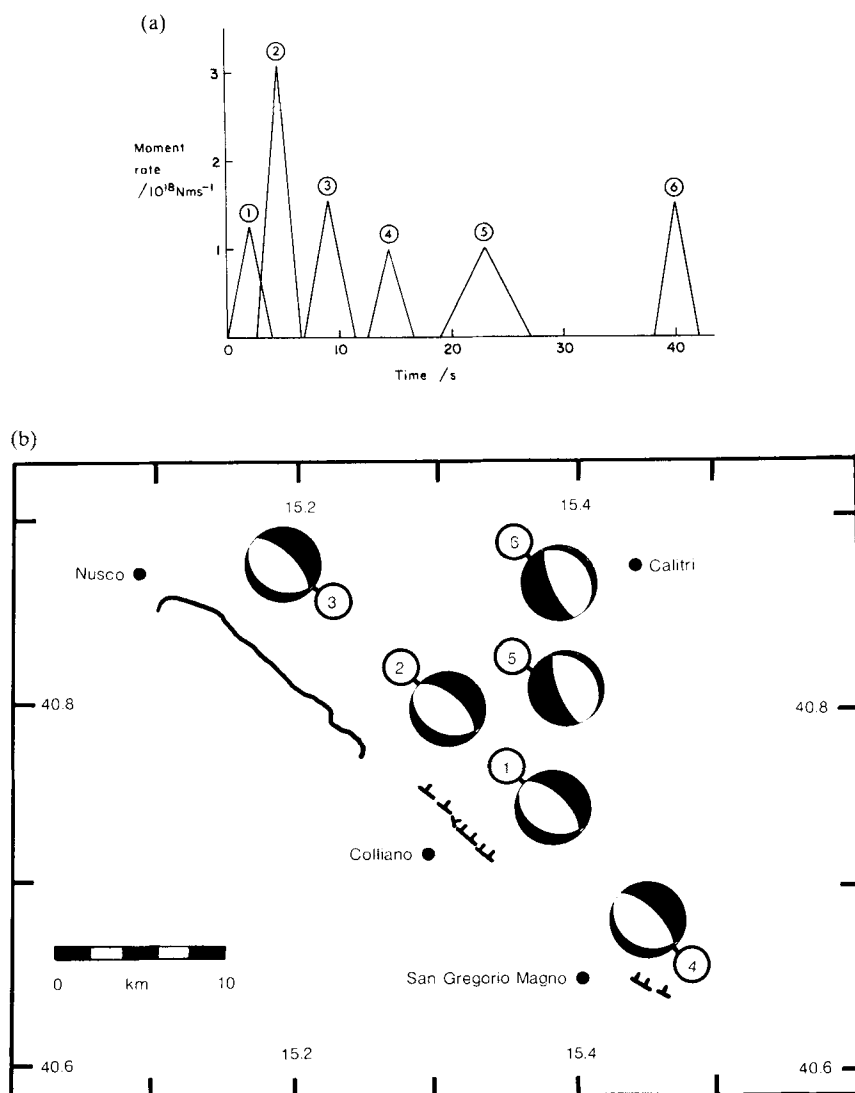


**Figure 24.** (a) Moment rate for the final, preferred, source model, incorporating six subevents. (b) Summary map of the final, preferred, source model, incorporating six subevents. The map shows the focal mechanism and the suggested position of faulting in each of these subevents.

six subevents of faulting that have been identified is estimated from waveform modelling as  $21.4 \times 10^{18} \text{ Nm}$ . Thus, our waveform modelling can account for most of the moment of  $26 \times 10^{18} \text{ Nm}$  predicted from moment tensor inversion studies in Section 7.

Our waveform modelling of the last two subevents, which occurred 19 and 38 s after the origin time, suggests that they had focal mechanisms with one nodal plane dipping at about  $20^\circ \text{ NE}$ , and the other at about  $70^\circ \text{ SW}$ . These subevents may either represent faulting in an antithetic sense to that in the early ruptures, or involve motion on low angle normal faults beneath the hanging wall of the faults that were active in the early ruptures. It is of interest to try to establish which of these two alternatives was the fault plane. Three lines of evidence suggest that the late ruptures occurred on low angle faults. First, the total moment

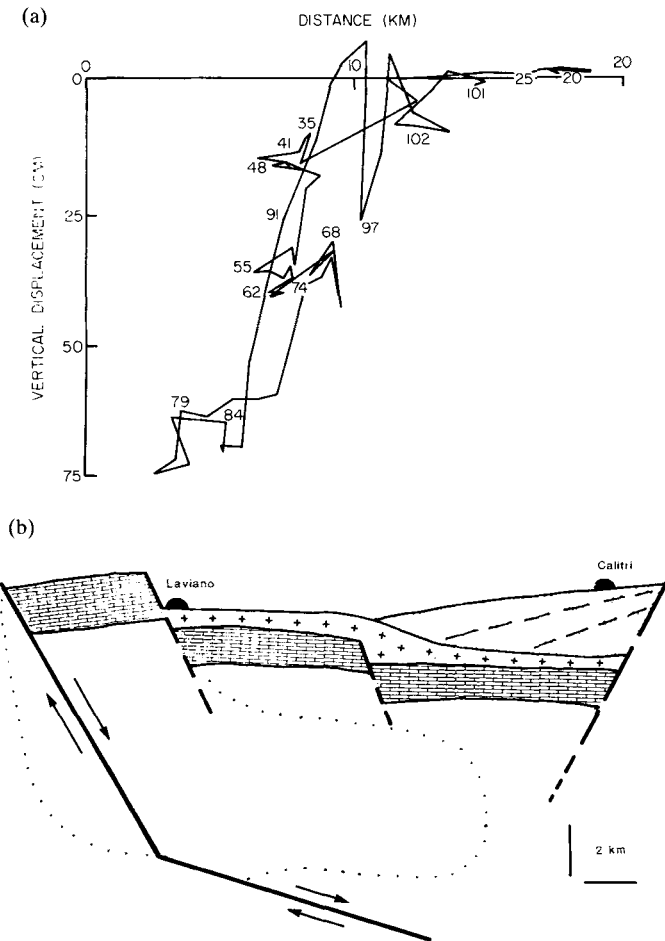


**Figure 25.** (Above and opposite.) (a) Elevation changes in the hanging wall observed through levelling by Arca *et al.* (1983), in a section striking at N 43° E. The projection of the Monte Marzano segment of surface faulting is 2 km SW of the origin. Note that ground elevation changes are only observed less than 15 km NE of the surface faulting. Fig. 4 of Arca *et al.* (1983). (b) Section orientated SW-NE across the area in which faulting occurred in the mainshock, indicating the suggested relationship between slip in both early and late mainshock ruptures, and deformation due to aftershocks. Information on the structural geology of the area is simplified from Ippolito *et al.* (1974) and from Ortolani & Torre (1981). It is based on borehole logs and on interpretation of shallow seismic reflection profiles shot for hydrocarbon exploration. Mesozoic limestone is indicated by brickwork shading, 'flysch' by crosses and Pliocene deposits of the Cairano basin by stipple. The area containing aftershocks is outlined by fine dots, and is based on Fig. 23(b). (c) Position of the levelling line (L) for which ground elevation changes have been modelled by Arca *et al.* (1983) and Crosson *et al.* (1986), in relation to the Monte Marzano (M) and Monti Picentini (P) segments of faulting, so the Sele Valley (V), and to the NE-striking fault (F) suggested by Crosson *et al.* (1986) as the source of the 40 s subevent. Benchmark numbers along the levelling line are from Arca *et al.* (1983).

from the late ruptures is estimated as  $7 \times 10^{18}$  Nm, and is large compared with the moment released on any one of the segments of fault that moved in the early ruptures. Each of these subevents would have been an earthquake of about  $M_S = 6.3$  if it had occurred on its own, sufficiently large for surface faulting to be expected if it had occurred on a steep antithetic fault, as was observed following the Gulf of Corinth, Greece, earthquake of 1981 March 4

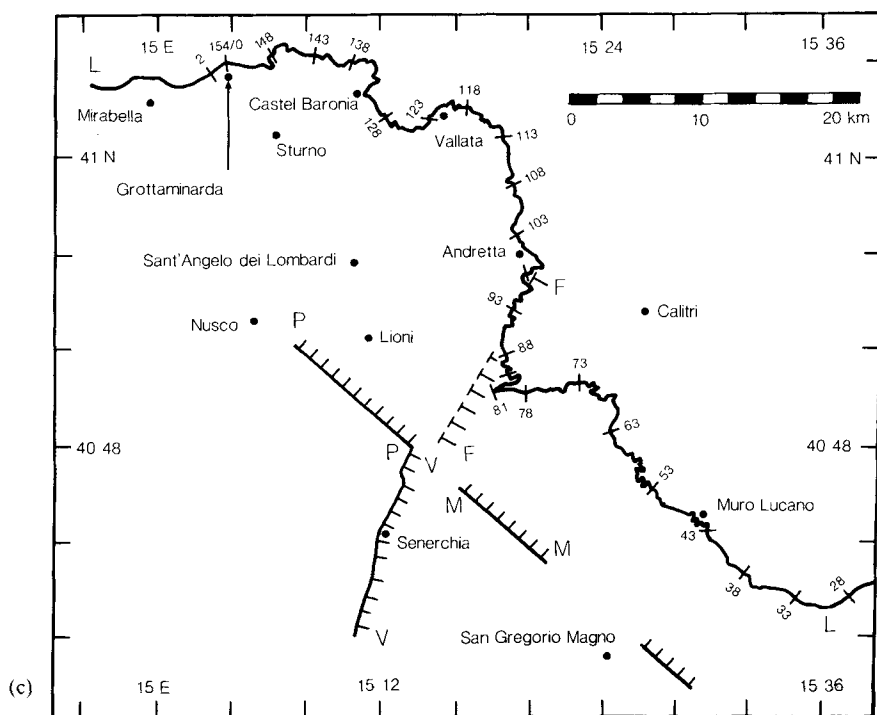


Figure 25—continued

(Jackson *et al.* 1982a). No antithetic surface faulting was found, even though the area where it might be expected, the northern edge of the Cairano basin (Fig. 26), is much more accessible, flatter, more open and more densely populated than the area in which the surface faulting from the first subevent was found (Fig. 1). However, the rocks in this area, mostly Miocene 'flysch' and Pliocene basin sediments, may be insufficiently brittle to support surface faulting. Secondly, measurements of elevation changes following the mainshock (Arca *et al.* 1983) indicate that the overall pattern was for subsidence to decrease smoothly away from the surface faulting from the early ruptures (Fig. 25a). The effect of the earthquake was thus to tilt the Cairano basin area towards the SW. Upper Pliocene sediments in this basin dip at between  $10^\circ$  and  $30^\circ$  towards the SW (e.g. Ortolani & Torre 1981). Presumably this dip has arisen from repeated movement in earthquakes similar to the 1980 event, indicating that the system of faults active in 1980 may have controlled the formation of this basin since Pliocene time. If the late ruptures had involved antithetic faulting, because their moments are comparable to the moments on any segment of fault that moved in the early ruptures, slip on each antithetic fault would be expected to be comparable to that on each of the faults that broke in the early ruptures. The block that is the hanging wall of both sets of fault would then have subsided uniformly, rather than tilting towards the southwest. Thirdly, aftershock moment-density (Fig. 23a and b) decreases smoothly and gradually NE of the faults that moved in the early ruptures. Had a major antithetic fault been active also, an abrupt NE edge to the aftershock zone would be expected, like the SW edge across the faults that moved in the early ruptures (Fig. 23a and b). Also, aftershocks with normal-faulting focal mechanisms similar to the mechanism of the late ruptures would be expected, close to the NE edge of the aftershock zone. However, neither Deschamps & King (1984) nor Westaway (1985) found any aftershock focal mechanism with this orientation.

Our interpretation of the late ruptures as involving low-angle faulting (Fig. 25b), is similar to that made by Eyidogan & Jackson (1985) for late ruptures in the Gediz (1970 March 28) and Alasehir (1969 March 28) normal-faulting earthquakes in western Turkey. The explanation suggested by Eyidogan & Jackson is that after steep normal faulting in the early ruptures breaks through the brittle upper crust, the usually ductile lower crust experienced a much higher strain rate than usual, and for a few seconds behaved in a brittle manner, breaking on a low angle normal fault. It is interesting to note that the low angle ruptures inferred by Eyidogan & Jackson had long-duration time-functions, similar to that for the 20 s subevent in this Italian earthquake. An active low angle fault would have the maximum of its *S*-wave radiation pattern directed upwards. Localities in this region, in the hanging wall of the early ruptures, would consequently experience very strong horizontal ground motion. Thus, the inferred motion on these low angle faults may explain the severe destruction that occurred at localities in the hanging wall (e.g. Alexander 1981). Consequently, it is of considerable engineering importance to establish how widespread low angle ruptures of this type are in normal-faulting earthquakes.

In contrast, Crosson *et al.* (1986) have suggested that the 40 s subevent involved motion on a near-vertical normal fault striking approximately NE, downthrown to the SE, extending NE from the northern end of the Sele Valley; a viewpoint which has stimulated lively discussion (Westaway 1987b; Crosson *et al.* 1987). The main evidence presented by Crosson *et al.* (1986) in support of their suggestion is elastic modelling of ground elevation changes observed by levelling. Apart from this elastic modelling, four other lines of evidence, which we have presented, are relevant to a discussion of the orientation of the faulting in the 40 s subevent. First, no surface faulting has been observed striking NE anywhere in the epicentral area. As already mentioned, Gars (1983) showed that the normal fault along the W side of the Sele Valley (Fig. 3), which has approximately the same orientation as the NE-striking fault of Crosson *et al.* showed no movement at the surface in 1980. Also, there is no evidence that any major NE-striking fault exists further NE, near the levelling line, at the position suggested by Crosson *et al.* Many landslides occurred in this region (Alexander 1981; Cantalamessa *et al.* 1981), but they do not lie on a NE-trending zone that might indicate a NE-striking buried seismogenic normal fault. Also, the presence of landslide activity along the levelling line may mean that it is not measuring tectonic elevation changes at all localities (Westaway 1987b). Secondly, there is the evidence from our waveform modelling (Figs 20 and 21). We prefer the match of the observed waveforms obtained using our model to that using the model of Crosson *et al.* but acknowledge that the overall improvement with our model is not dramatic, and that a source for the 40 s subevent with the orientation suggested by Crosson *et al.* matches some observed waveforms better. Thirdly, there is the evidence from the 'anomalous' aftershocks, discussed in Section 10, some of which have NE-striking nodal planes. Some of these have focal mechanisms similar to that required for motion on the NE-striking fault of Crosson *et al.* but a larger number have focal mechanisms with the opposite polarity in all quadrants. In any case, the total moment from these 'anomalous' aftershocks is very small compared with that necessary to generate the pattern of slip required by Crosson *et al.* on their NE-striking fault. We do not consider that the existence of small aftershocks with NE-striking nodal planes influences the argument about the existence of a major NE-striking fault either way. Finally, the modelling of Crosson *et al.* ignores elevation changes due to faulting NW of the Sele Valley, which our waveform modelling suggests accounts for more than half of the total moment released on steep NW-striking faults during the mainshock. The levelling line extends from SE to NW, passing at some points within 10 km of the surface faulting along the Monte Marzano segment. NE of the Sele Valley, the levelling line runs north-eastward for about



15 km (Fig. 25c), before resuming its NW trend more than 20 km NE of the Monti Picentini fault segment. The line thus has a Z shape overall. In the region of the NE offset in the line, the NW portion was apparently uplifted relative to the SE portion. Crosson *et al.* interpreted this pattern in terms of a NE-striking normal fault, downthrown to the SE, situated close to the offset in the line. We suggest that the observed pattern of elevation changes could also be a consequence of the line changing its distance from the almost continuous normal faulting, with a NW strike, along the Monte Marzano and Monti Picentini segments. The NW portion of the levelling lines is probably too far NE of the Monti Picentini segment to be sensitive to elevation changes due to the normal faulting there. Although Crosson *et al.* achieved an impressive match to the observed elevation changes, they did so with a model that ignores a large part of the overall faulting; indicating that their model is non-unique. The low-angle fault planes that we believe moved in the 20 s and 40 s subevents extend beneath the levelling line. Because any slip on these planes would be predominantly horizontal, elevation changes due to this slip would be relatively small, and, if our interpretation that such slip represents failure of the uppermost lower crust at high strain rates is correct, the accompanying elevation changes are unlikely to be modelled correctly using an elastic rheology. After considering the available evidence, we prefer our source model to that of Crosson *et al.*

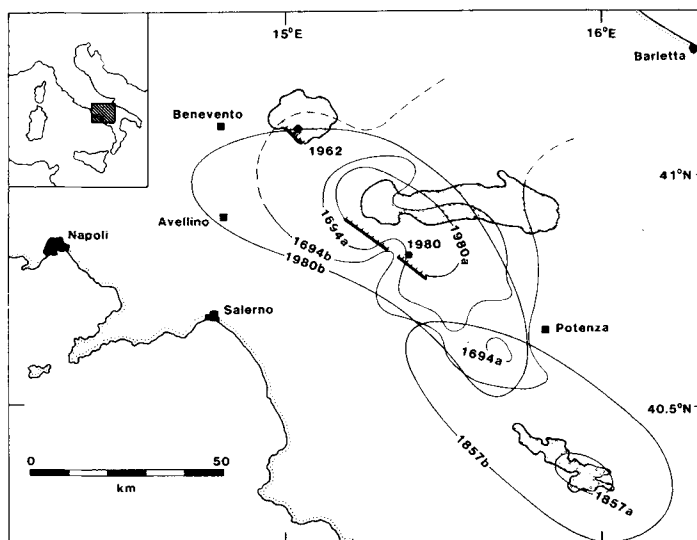


**Figure 26.** Epicentral areas of the 1694, 1857, 1962 and 1980 earthquakes in the southern Apennines, showing their relationship to Plio-quaternary sedimentary basins in the region, indicated by stipple. The Ariano basin, in the epicentral area of the 1962 earthquakes, is in the NW corner of the figure. The Cairano basin, in the epicentral area of the 1980 and 1694 earthquakes, is in the middle of the figure, and the Sant'Arcangelo basin, in the epicentral area of the 1857 earthquake, is in the SE corner. Instrumentally determined locations, where available, are marked by filled dots, and localities where faulting has been observed, or inferred to have taken place, are indicated with tick marks on the down-thrown side. Information for the 1694 earthquake is from Serva (1981). The isoseismals 1694 (a) and (b) have been assigned intensities X and IX. Information for the 1857 earthquake is from Mallet (1862). Isoseismals 1857 (a) and (b) enclose, respectively, all villages at which more than 10 per cent of the population was killed, and all localities at which anyone was killed. These correspond approximately to the intensity X and IX isoseismals of Magri & Molin (1979). Information for the 1962 earthquake is from Westaway (1987a). It has been located relative to the 1980 event. The isoseismals for the 1980 event, from Berardi *et al.* (1981), are assigned intensities of IX (1980a) and VIII (1980b). Other information for the 1980 earthquake is from this study.

We consider that the correct interpretation of the region at the northern end of the Sele Valley is that it behaves as a 'segment boundary' in the sense used by Schwartz & Coppersmith (1984) and others who have documented active normal faults elsewhere. We note further that the initial fault rupture nucleated close to the northern end of the Sele Valley, and that our short-period strong ground motion study suggests that the Monte Marzano segment of fault ruptured first, followed by the Monti Picentini segment on the opposite side of the Sele Valley. These two fault ruptures appear to have occurred in opposite directions away from this segment boundary.

We suggested above that the pattern of elevation changes observed following the 1980 earthquake was consistent with the pattern of deformation that has occurred in the Cairano basin since Pliocene time, and that the same system of faults may have been active throughout this timespan. In the southern Apennines, other earthquakes appear to be associated in a similar way with other intra-Apennine sedimentary basins of Pliocene and younger age. The earthquake of 1694 September 8 (Serva 1981) appears to have been of comparable size to the 1980 event and to have occurred in approximately the same place (Fig. 26). Further NW, the earthquakes of 1962 August 21 (Westaway 1987a) have been shown to be associated with normal faults that dip NE beneath the Ariano basin. To the SE, the distribution of damage (Mallet 1862, Magri & Molin 1979) for the event of 1857 December 16 suggests that it occurred beneath the Sant'Arcangelo basin. These two other intra-Apennine sedimentary basins are of similar age and comparable size to the Cairano basin, associated with the 1980 earthquake. These observations suggest that intra-Apennine sedimentary basins should be regarded as areas of high seismic hazard relative to surrounding areas. Like individual short strands of surface faulting around Monte Marzano (Fig. 1), the three large systems of normal fault in Fig. 26 step to the right, implying a small component of left-lateral strike-slip along the whole deforming zone in the southern Apennines.

There are no grounds for suggesting that the geometry of active normal faults in the Apennines is any different from that expected in other areas of active continental extension.

### Acknowledgments

We thank the station operators at many WWSSN stations, and the staff at the data centres at the British Geological Survey, Edinburgh, and at Lamont–Doherty Geological Observatory, New York, for providing copies of seismograms. We would also like to thank an anonymous reviewer whose detailed and constructive criticism substantially improved sections of this article.

The digitized records of ground acceleration used were generously provided by the staff of ENEA, Rome. We would particularly like to thank Marcello Peronaci and Dario Rinaldis for their assistance.

The centroid-moment tensor inversion study was carried out at Harvard University, with help from Gören Ekström and John Woodhouse.

RW acknowledges financial support through a research scholarship from Shell International Ltd, who also provided financial support for fieldwork and for other travel in relation to these studies. Other aspects of this work were supported by the Natural Environment Research Council. Part of this work was carried out while RW was supported by a Research Fellowship at the University of Reading.

This is publication number 841 of the Department of Earth Sciences, University of Cambridge.

## References

- Aki, K. & Richards, P. G., 1980. *Quantitative Seismology, Theory and Methods*, 2 vols, Freeman, San Francisco.
- Alexander, D. E., 1981. Preliminary assessment of landslides resulting from the earthquake of 23rd November 1980 in Southern Italy, *Disasters*, **5**, 376–383.
- Alexander, D. E., 1982. *The earthquake of 23rd November 1980 in Campania and Basilicata, Southern Italy*, International Disaster Institute, London.
- Anderson, H. J., 1985. Seismotectonics of the western Mediterranean, *PhD thesis*, University of Cambridge.
- Anderson, H. J. & Jackson, J. A., 1987. Active tectonics of the Adriatic region, *Geophys. J. R. astr. Soc.*, in press.
- Arca, S., Bonasia, V., Gaulon, R., Pingue, F., Ruegg, J. C. & Scarpa, R., 1983. Ground movements and faulting mechanism associated to the November 23, 1980 Southern Italy earthquake, *Boll. geod. sci. affini*, **XLII**, 137–147.
- Bakun, W. H., 1984. Magnitudes and moments of duration, *Bull. seism. Soc. Am.*, **74**, 2335–2356.
- Berardi, R., Berenzi, A. & Capozza, F., 1981. *Campania–Lucania earthquake on 23 November 1980: Accelerometric recordings of the main quake and relating processing. Contributo alla caratterizzazione della sismicità del territorio Italiano*, 1–103. Contribution to the annual convention of the Italian National Research Project on Italian Seismicity, Udine, 12–14 May 1981.
- Berberian, M., Jackson, J. A., Ghorashi, M. & Kadjar, M. H., 1984. Field and teleseismic observations of the 1981 Golbaf–Sirch earthquakes in SE Iran, *Geophys. J. R. astr. Soc.*, **77**, 809–838.
- Bollettinari, G. & Panizza, M., 1981. Una ‘faglia di superficie’ presso San Gregorio Magno in occasione del sisma del 23-XI-1980 in Irpinia, *Rend. Soc. geol. It.*, **4**, 135–136 (in Italian).
- Boschi, E., Mulargia, F., Mantovani, E., Bonafede, M., Dziewonski, A. M. & Woodhouse, J. H., 1981. The Irpinia earthquake of November 23, 1980 (abstr.), *EOS, Trans. Am. Geophys. Un.*, **62**, 330.
- Brüster, W. & Müller, G., 1983. Moment and duration of shallow earthquakes from Love-wave modelling for regional distances, *Phys. Earth planet. Int.*, **32**, 312–324.
- Campbell, K. W., 1985. Strong motion attenuation relations: a ten-year perspective, *Earthquake Spectra*, **1**, 759–804.
- Cantalamesa, G., Dramis, F., Pambianchi, G., Romano, A., Santoni, A. M. & Tonnetti, G., 1981. Fenomeni franosi connessi con attività sismica nell’area compresa tra S. Giorgio La Molara e Bisaccia, *Rend. Soc. geol. It.*, **4**, 467–469 (in Italian).
- Carmignani, L., Cello, G., Cerrina Ferroni, A., Funicello, R., Kälin, O., Meccheri, M., Patacca, E., Pertusati, P., Plesi, G., Salvini, F., Scandone, P., Tortorici, L. & Turco, E., 1981. Analisi del campo di fratturazione superficiale indotto dal terremoto Campano-Lucano del 23/11/80, *Rend. Soc. geol. It.*, **4**, 451–465 (in Italian).
- Cinque, A., Lambiase, S. & Sgroso, I., 1981. Su due faglie nell’alta valle del Sele legate al terremoto del 23.11.1981, *Rend. Soc. geol. It.*, **4**, 127–129 (in Italian).
- Crosson, R. S., Martini, M., Scarpa, R. & Key, S. C., 1986. The Southern Italy earthquake of 23rd November 1980: An unusual pattern of faulting, *Bull. seism. Soc. Am.*, **76**, 381–394.
- Crosson, R. S., Martini, M., Scarpa, R. & Key, S. C., 1987. Reply to “R. Westaway’s comment on ‘The Southern Italy earthquake of 23rd November 1980: an unusual pattern of faulting’ by R. S. Crosson, M. Martini, R. Scarpa and S. C. Key”, *Bull. seism. Soc. Am.*, in press.
- Deschamps, A., Iannaccone, G. & Scarpa, R., 1984. The Umbrian earthquake (Italy) of 19 September 1979, *Annales Geophys.*, **2**, 29–36.
- Deschamps, A. & King, G. C. P., 1983. The Campania–Lucania (southern Italy) earthquake of 23 November 1980, *Earth planet. Sci. Lett.*, **62**, 296–304.
- Deschamps, A. & King, G. C. P., 1984. Aftershocks of the Campania–Lucania (Italy) earthquake of 23 November 1980, *Bull. seism. Soc. Am.*, **74**, 2483–2517.
- Doser, D. I., 1985. The 1983 Borah Peak, Idaho and 1959 Hebgen Lake, Montana earthquakes: models for normal fault earthquakes in the intermountain seismic belt, in *Proc. of Workshop XXVIII on the Borah Peak, Idaho, Earthquake*, pp. 368–384, *U.S. geol. Surv. Open File Rep.*, 85–290.
- Dziewonski, A. M., Chou, T.-A. & Woodhouse, J. H., 1981. Determination of earthquake source parameters from waveform data for studies of global and regional seismicity, *J. geophys. Res.*, **86**, 2825–2852.
- Dziewonski, A. M., Franzen, J. E. & Woodhouse, J. H., 1985. Centroid-moment tensor solutions for July–September, 1984, *Phys. Earth planet. Int.*, **38**, 203–213.

- Eyidogan, H. & Jackson, J. A., 1985. A seismological study of normal faulting in the Demirci, Alasehir and Gediz earthquakes of 1969–1970 in western Turkey: implications for the nature and geometry of deformation in the continental crust, *Geophys. J. R. astr. Soc.*, **81**, 569–607.
- Fels, A., Pugliese, A. & Muzzi, F., 1981. *Campano–Lucano earthquake, November 1980, Italy: Strong motion data related to local site conditions. Contributo alla caratterizzazione della sismicità del territorio Italiano*, 105–124. Contribution to the annual convention of the Italian National Research Project on Italian Seismicity, Udine, 12–14 May 1981.
- Futterman, W. I., 1962. Dispersive body waves, *J. geophys. Res.*, **67**, 5279–5291.
- Gars, G., 1983. Etudes seismotectoniques en Méditerranée centrale et orientale: I. La neotectonique de l'Appennin meridional et le seisme (23 Nov 80) de l'Irpinia (Italie). II. Les failles activées par les seismes (Fev.–Mars 81) de Corinthe (Grèce), *Thesis*, Université de Paris Sud, Centre d'Orsay (in French).
- Gasparini, C., Iannaccone, G., Scandone, P. & Scarpa, R., 1982. Seismotectonics of the Calabrian arc, *Tectonophysics*, **84**, 267–286.
- Gasparini, C., Iannaccone, G. & Scarpa, R., 1985. Fault plane solutions and seismicity of the Italian peninsula, *Tectonophysics*, **117**, 59–78.
- Ghisetti, F., Scarpa, R. & Vezzani, L., 1982. Seismic activity, deep structures and deformation processes in the Calabrian arc, southern Italy, *Earth Evolution Sci.*, **3**, 248–260.
- Ghisetti, F. & Vezzani, L., 1982. Different styles of deformation in the Calabrian arc (Southern Italy): implications for a seismotectonic zoning, *Tectonophysics*, **85**, 149–165.
- Görler, K. & Giese, P., 1978. Aspects of the Evolution of the Calabrian arc, in *Alps, Apennines, Hellenides: Geodynamic Investigations along Geotraverses by an international group of geoscientists*, *Inter-Union Commission of Geodynamics Scientific Rep.* 38., pp. 374–388, eds Closs, H., Roeder, D. & Schmidt, K., E. Schweizerbartische Verlagsbuchhandlung, Stuttgart, West Germany.
- Hagiwara, T., 1958. A note on the theory of the electromagnetic seismograph, *Earthquake Res. Inst. Bull. Tokyo University*, **36**, 139–164.
- Helmberger, D. V., 1983. Theory and application of synthetic seismograms, in *Earthquakes: Observation, Theory and Interpretation*, LXXXV Corso, pp. 174–222, eds Kanamori, H. & Boschi, E., Soc. Italiana di Fisica, Bologna.
- Herrin, E., 1968. 1968 seismological tables for *P* phases, *Bull. seism. Soc. Am.*, **58**, 1193–1241.
- Ippolito, F., d'Argenio, B., Pescatore, T. & Scandone, P., 1975. Structural–stratigraphic units and the tectonic framework of the Southern Apennines, in *Geology of Italy*, pp. 317–328, ed. Squyres, C. H., The Earth Sciences Society of the Libyan Arab Republic, Tripoli, Libya.
- Ippolito, F., Ortolani, F. & di Nocera, S., 1974. Alcune Considerazioni sulla struttura profonda dell'Appennino Irpino: reinterpretazione di ricerche di idrocarburi, *Boll. Soc. geol. It.*, **93**, 861–881 (in Italian).
- Jackson, J. A., 1987. Active normal faulting and continental extension, in *Continental Extensional Tectonics*, pp. 3–17, eds Coward, M. P., Dewey, J. F. & Hancock, P. L., Spec. Publ. geol. Soc. Lond., Blackwell Scientific Publications, Oxford.
- Jackson, J. A., Gagnepain, J., Houseman, G., King, G. C. P., Papadimitriou, P., Soufleris, C. & Virieux, J., 1982a. Seismicity, normal faulting and the geomorphological development of the Gulf of Corinth (Greece): the Corinth earthquakes of February and March 1981, *Earth planet. Sci. Lett.*, **57**, 377–397.
- Jackson, J. A., King, G. & Vita-Finzi, C., 1982b. The neotectonics of the Aegean: an alternative view, *Earth planet. Sci. Lett.*, **61**, 303–318.
- Jackson, J. A. & McKenzie, D. P., 1983. The geometrical evolution of normal fault systems, *J. struct. Geol.*, **5**, 471–487.
- Jeffreys, H. & Bullen, K. E., 1967. *Seismological Tables*, British Association for the Advancement of Science, London.
- Johnston, D. E. & Langston, C. A., 1984. The effect of assumed source structure on earthquake source parameters: the eastern Hispaniola earthquake of 14 September 1981, *Bull. seism. Soc. Am.*, **74**, 2115–2134.
- Joyner, W. B. & Boore, D. M., 1981. Peak horizontal acceleration and velocity from strong-motion records including records from the Imperial Valley, California, earthquake, *Bull. seism. Soc. Am.*, **71**, 2011–2038.
- Julian, B. R., 1983. Evidence for dyke intrusion earthquake mechanisms near Long Valley caldera, California, *Nature*, **303**, 323–325.
- Kanamori, H. & Given, J. W., 1982. Use of long-period surface waves for rapid determination of earth-

- quake source parameters, 2. Preliminary determination of source mechanisms of large earthquakes ( $M_s > 6.5$ ) in 1980, *Phys. Earth planet. Int.*, **30**, 260–268.
- Kanasewich, E. R., 1981. *Time Series Analysis in Geophysics*, 3rd edn, pp. 274–277, University of Alberta Press, Edmonton, Canada.
- Key, S. C. & Crosson, R. S., 1984. Ground deformation modelling of the southern Italy earthquake of November 23, 1980 (abstr.), *Eos, Trans. Am. Geophys. Un.*, **65**, 1015.
- Knopoff, L. & Randall, M. J., 1970. The compensated linear-vector dipole: a possible mechanism for deep earthquakes, *J. geophys. Res.*, **75**, 4957–4963.
- Langston, C. & Helmberger, D., 1975. A procedure for modelling shallow dislocation sources, *Geophys. J. R. astr. Soc.*, **42**, 117–130.
- Lee, W. H. K. & Lahr, J. E., 1975. HYPO71: a computer program for determining hypocentre, magnitude and first motion pattern of local earthquakes, *U.S. Geol. Surv. Open File Rept.*, 75–311.
- McKenzie, D. P., 1972. Active tectonics of the Mediterranean region, *Geophys. J. R. astr. Soc.*, **30**, 109–185.
- Madariaga, R., 1983. High frequency radiation from dynamic fault models, *Annls. Geophys.*, **1**, 17–23.
- Magri, G. & Molin, D., 1979. *Attività macrosismica in Basilicata, Campania e Puglia dal 1847 al 1861*. Comitato Nazionale Energia Nucleare rep. no. RT/AMB(79)5 (in Italian).
- Mallet, R., 1862. *The Great Neapolitan Earthquake of 1857*, 2 vol, Chapman and Hall, London.
- Mantovani, E. & Boschi, E., 1983. Tectonics and seismicity in the Italian region, in *Earthquakes: Observation, Theory and Interpretation*, LXXXV Corso, pp. 519–529, eds Kanamori, H. & Boschi, E., Soc. Italiana di Fisica, Bologna.
- Martini, M. & Scarpa, R., 1983. Earthquakes in Italy in the last century, in *Earthquakes, Observation, Theory and Interpretation*, LXXXV Corso, pp. 479–492, eds Kanamori, H. & Boschi, E., Soc. Italiana di Fisica, Bologna.
- Nabelek, J. L., 1984. Determination of earthquake source parameters from inversion of body waves, *PhD thesis*, Massachusetts Institute of Technology.
- Niazi, M., 1982. Source dynamics of the 1979 Imperial Valley earthquake from near-source observations of ground acceleration and velocity, *Bull. seism. Soc. Am.*, **72**, 1969–2002.
- Ogniben, L. & Vezzani, L., 1975. Nappe structure of Sicily, Calabria and Lucania, Italy, in *Geology of Italy*, pp. 83–104, ed. Squyres, C. H., The Earth Sciences Society of the Libyan Arab Republic, Tripoli, Libya.
- Ortolani, F., 1975. Assetto strutturale dei Monti Picentini, della valle del Sele e del gruppo di Monte-Marzano-Monte Ognà (Appennino meridionale): implicazioni idrogeologiche, *Boll. Soc. geol. ital.*, **94**, 209–230 (in Italian).
- Ortolani, F., 1981. Principali effetti geologici di superficie del terremoto del 23.11.1980, *Rend. Soc. Geol. It.*, **4**, 71 (in Italian).
- Ortolani, F. & Torre, M., 1981. Guida all'Escursione nell'area interessata dal terremoto del 23 Novembre 1980, *Rend. Soc. Geol. It.*, **4**, 173–214 (in Italian).
- del Pezzo, E., Iannaccone, G., Martini, M. & Scarpa, R., 1983. The 23 November 1980 Southern Italy earthquake, *Bull. seism. Soc. Am.*, **73**, 187–200.
- Reutter, K. J., Giese, P. & Closs, H., 1980. Lithospheric split in the descending plate: observations from the northern Apennines, *Tectonophysics*, **64**, T1–T9.
- Ritsema, A. R., 1971. Notes on plate tectonics and arc movements in the Mediterranean region, *Communs. Obs. r. Belg. Geophys. Ser.*, **101**, 22.
- da Roit, R., Fontanive, A., Fontanive, L., Spat, G. & Pezze, M., 1983. *Comportamento dei terreni non coesivi sarni in alcune zone colpite dai terremoti del Friuli del 1976 e Campano Lucano del 1980*, Proceedings of the Fifteenth Italian National Convention on Geotechnical Engineering, Spoleto, 4–6 May 1983, pp. 105–114 (in Italian).
- Schwartz, D. P. & Coppersmith, K. J., 1984. Fault behaviour and characteristic earthquakes: examples from the Wasatch and San Andreas fault zones, *J. geophys. Res.*, **89**, 5681–5698.
- Serva, L., 1981. Il terremoto del 1694 in Irpinia e Basilicata, in *Contributo alla caratterizzazione della sismicità del territorio Italiano*, pp. 183–208. Contribution to the Annual Convention of the Italian National Research Project on Italian Seismicity, Udine, 12–14 May 1981 (in Italian).
- Smith, R. B. & Bruhn, R. L., 1984. Intraplate extensional tectonics of the eastern Basin-Range: inferences on structural style from seismic reflection data, regional tectonics and thermal-mechanical models of brittle-ductile deformation, *J. geophys. Res.*, **89**, 5733–5762.
- Soufleris, C. & Stewart, G. S., 1981. A source study of the Thessaloniki (north Greece) earthquake sequence, *Geophys. J. R. astr. Soc.*, **67**, 343–358.

- Stein, R. S. & Barrientos, S. E., 1985. Planar high-angle faulting in the Basin and Range: geodetic analysis of the 1983 Borah Peak, Idaho, earthquake, *J. geophys. Res.*, **90**, 11 355–11 366.
- Westaway, R. W. C., 1985. Active tectonics of Campania, southern Italy, *PhD thesis*, University of Cambridge.
- Westaway, R. W. C., 1987a. The Campania, southern Italy, earthquakes of 1962 August 21, *Geophys. J. R. astr. Soc.*, **88**, 1–24.
- Westaway, R. W. C., 1987b. Comment on ‘The Southern Italy earthquake of 23rd November 1980: An unusual pattern of faulting’ by R. S. Crosson, M. Martini, R. Scarpa & S. C. Key, *Bull. seism. Soc. Am.* (in press).
- Westaway, R. W. C. & Jackson, J. A., 1984. Surface faulting in the southern Italian Campania–Basilicata earthquake of 23 November 1980, *Nature*, **312**, 436–438.
- Whitcomb, J. H., Allen, C. R., Garmany, J. D. & Hileman, J. A., 1973. San Fernando earthquake sequence, 1971: focal mechanisms and tectonics, *Rev. Geophys. Space Phys.*, **11**, 693–730.
- Yielding, G., Jackson, J., King, G., Sinvhal, H., Vita-Finzi, C. & Wood, R., 1981. Relations between surface deformation, fault geometry, seismicity and rupture characteristics during the El Asnam (Algeria) earthquake of 10 October 1980, *Earth planet. Sci. Lett.*, **56**, 287–304.